Dissertation

Investigation of $\bar{K}$-Nucleus Interaction through Exclusive Measurements of the $^{12}\mathrm{C}(K^-, p)$ Reaction

($^{12}\mathrm{C}(K^-, p)$ 反応のエクスクルーシブ測定を通した
反 **K** 中間子**-**原子核間の相互作用研究)

Fumiya Oura

Department of Physics,
Graduate School of Science,
Tohoku University

February, 2026

Abstract

The interaction between the antikaon ($\overline{K}$) and the atomic nucleus, particularly the imaginary part of the optical potential (W_0), remains a subject of significant debate in hadron and nuclear physics. While the real part of the potential has been constrained to be relatively shallow ($V_0 \sim -80$ MeV) by recent kaonic atom X-ray measurements and inclusive reaction data, the imaginary part—governing absorption in the nuclear medium—has relied heavily on X-ray data, which are inherently sensitive only to the nuclear surface. Consequently, large uncertainties remain regarding the depth of the imaginary potential and the contribution of multi-nucleon absorption processes (e.g., $K^- NN \to YN$) in the nuclear interior.

In this study, we present a novel approach to determine the imaginary part of the potential by measuring the escape process of the K^- in the $^{12}\mathrm{C}(K^-, p)$ reaction. The escape process corresponds to quasi-free elastic scattering (QFES) in which the scattered K^- emerges from the nucleus without being absorbed. This observable provides direct sensitivity to the absorption strength inside the nucleus.

The experiment (J-PARC E42) was performed at the J-PARC K1.8 beamline using a high-intensity 1.8 GeV/c K^- beam incident on a diamond (^{12}C) target. A key feature of the experimental setup was the Hyperon Time Projection Chamber (HypTPC), installed inside a superconducting solenoid magnet, which enabled the exclusive reconstruction and identification of scattered particles with large acceptance.

We successfully derived the escape cross section to be $\left(\frac{d\sigma}{d\Omega}\right)_{\mathrm{esc}} = 436 \pm 6$ (stat.) $\pm$ 26 (syst.)μb/sr. To placing a quantitative constraint on the optical potential, we performed a simultaneous χ^2 minimization fit to both the inclusive and escape binding energy spectra. This analysis yielded the optimal potential depths at the nuclear center as $V_0 = -72^{+3}_{-5}$ (stat.)$^{+0}_{-8}$ (syst.) MeV and $W_0 = -100^{+7}_{-1}$ (stat.)$^{+0}_{-16}$ (syst.) MeV. This result represents the first high-precision determination of both the real and imaginary parts of the potential, successfully resolving the long-standing "continuous ambiguity" inherent in kaonic atom data.

Our findings reveal a nature of the $\bar{K}$-nucleus interaction: a moderately attractive real part consistent with chiral unitary models ($V_0 \sim -40$ to -80 MeV) combined with

a deeply absorptive imaginary part ($W_0 \sim -100$ MeV) that matches phenomenological fits like the DD potential. The results of the large W_0 value suggests the dominance of multi-nucleon absorption mechanisms, such as $\bar{K}NN \to YN$, in high-density nuclear matter.

Acknowledgements

First and foremost, I would like to express my deepest and most sincere gratitude to Professor Hirokazu Tamura. He introduced me to the fascinating world of hadron and nuclear physics, providing the very foundation of my research career. Through his own pursuit of physics, he taught me the vital importance of maintaining a broad perspective and never losing sight of the essential nature of phenomena. I am profoundly grateful for his numerous insightful suggestions and guiding advice, which consistently got to the heart of the physics problems. His unwavering support and the intellectual environment he fostered have been indispensable in completing this dissertation.

I would like to extend my sincere thanks to Professor Yudai Ichikawa. I am deeply indebted to him for the enormous amount of time he dedicated to discussing the analysis and providing invaluable guidance. His logical approach to complex problems and his commitment to scientific rigor served as a model for my own work. Beyond the technical aspects of this study, he taught me the fundamental principles and the integrity required for a professional researcher.

My heartfelt thanks go to Professor Shuhei Hayakawa, who invited me to join the J-PARC E42 experiment. I am grateful for his practical guidance in the analysis and his hands-on support at the experimental site. Through his mentorship, I was able to acquire essential expertise in Data Acquisition systems and the technical skills necessary for experimental physics.

I am also deeply grateful to Professor Jung Keun Ahn. He proposed this experiment and enthusiastically welcomed my participation. His vast knowledge of physics and creative ideas provided constant inspiration throughout this work.

I am grateful to the members of the J-PARC K1.8 beamline group and collaborators, including Professor Toshiyuki Takahashi, Professor Mifuyu Ukai, Professor Hiroyuki Sako, Professor Kiyoshi Tanida, Dr. Takeshi O. Yamamoto, Professor Shin Hyung

Kim, Professor Toshiyuki Gogami, Professor Manami Fujita, Mr. Takeshi K. Harada, and Mr. Kengo Ebata, for their continuous support not only during this experiment but also in the experiments following E42. My sincere thanks also go to the collaborators from Korea University: Dr. Woo Seung Jung, Mr. Byung Min Kang, Mr. Sung Wook Choi, and Ms. Hae In Lee. I am deeply thankful for their insightful advice and fruitful discussions on the analysis, and also for their warm hospitality during my stays in Korea.

I also thank all members of the J-PARC E42 and TPC collaborations for their dedicated efforts.

I wish to express my appreciation to Professor Junko Yamagata-Sekihara and Professor Satoru Hirenzaki. Their theoretical support and profound discussions were indispensable for the interpretation of the experimental results.

I would like to thank the laboratory staff, Professor Koji Miwa, Professor Masashi Kaneta, Professor Takuya Nanamura, and Professor Takeshi Koike. I am who I am today thanks to their guidance and the research environment they maintained. I would also like to express my special thanks to the laboratory secretaries, Ms. Ayumi Takahashi and Ms. Yukie Sasaki, the technical staff member, Mr. Hiroo Umetsu, the GP-PU secretary, Ms. Hiroko Lane Miwa, and all other administrative staff. Without their dedicated professional support, neither this dissertation nor my research activities would have been possible.

My time spent with the laboratory members over the past six years has been truly irreplaceable. I would like to thank Dr. Yuichi Toyama, Dr. Kosuke Itabashi, Dr. Yuji Ishikawa, Ms. Honoka Kanauchi, Ms. Anya Rogers, Dr. Kazuki Okuyama, Dr. Tamao Sakao, Dr. Takeru Akiyama, Mr. Shunsuke Kajikawa, Mr. Kento Kamada, Dr. Ryoko Kino, Mr. Hayato Miyata, Mr. Kazuma Ohashi, Mr. Chesu Seong, Mr. Daigo Watanabe, Mr. Ryoh Imamoto, Mr. Rintaro Kurata, Mr. Ryuta J. Saito, Mr. Koki Amemiya, Ms. Akari Haratani, Mr. Kaito Shimazaki, Mr. Zen Takano, Mr. Shota Toyama, Mr. Yuning Hong, Mr. Ryogo Akao, Mr. Yusuke Nakayama, Ms. Ruri Sasaki, and Ms. Miyu Yoshida. The countless hours of discussion, conversation, travels, and meals we shared have made them my most precious colleagues. Their constant encouragement and our daily interactions provided me with immense motivation and were truly indispensable in carrying out my research activities.

Finally, I would like to extend my sincere appreciation to all the people I have encountered and interacted with outside of my research. Above all, I wish to express my deepest gratitude to my family for their unconditional love, patience, and constant encouragement throughout my entire life. Their unwavering support and understanding have been the foundation of my strength and motivation, and I could never have completed this journey without them.

Standing at this new departure, I am eager to continue the exploration of nature, carrying the scientific mindset and insights I have gained here into my future career.

Contents

List of Figures

List of Tables

Chapter 1

Introduction

This chapter establishes the scientific context for the research presented in this dissertation. It begins with the motivation for studying kaonic nuclei and provides a survey of the relevant theoretical concepts and prior experimental work. The purpose of this review is to frame the unresolved questions in the field, thereby providing the foundation for the new experimental approach detailed in the subsequent chapters.

1.1 Scientific Motivation

From the Structure of Matter to the Strong Interaction

The visible matter in our universe—ranging from elementary particles to macroscopic astrophysical objects—is governed by the strong interaction, one of the fundamental forces in nature. Quarks (q) and antiquarks ($\bar{q}$) interact through gluons (g), forming color-neutral hadrons: mesons ($q\bar{q}$) and baryons (qqq). These hadrons constitute atomic nuclei, and it is not an exaggeration to say that the variety of these nuclei gives rise to the rich variety of chemical elements and chemical phenomena in our universe. Among them, the proton p and neutron n (collectively referred to as nucleons, N), composed of up and down quarks (u, d), represent the simplest and most essential building blocks of "ordinary" matter. Even with only two types of nucleons, an enormous diversity of bound nuclear systems is realized, underscoring how subtle changes in the strong interaction shape the complexity of the material world.

Despite the fact that the underlying theory of the strong interaction, Quantum Chromodynamics (QCD), is well established, predicting the structure and dynamics

of hadronic systems at the energy scales relevant for nuclear physics remains difficult. This difficulty originates from the non-perturbative nature of QCD in the low-energy regime. Hadrons —more than two hundred of which are now catalogued—provide a fertile testing ground for exploring such non-perturbative phenomena. Incorporating the strange quark (s) introduces a qualitatively new degree of freedom in addition to u, d quarks and enriches the landscape of hadronic interactions.

Motivation of $\bar{K}N$ and $\bar{K}$-Nucleus Interactions

A particularly intriguing case arises in the interaction between the antikaon ($\bar{K}$), a meson consisting of an s quark and a light antiquark, and the nucleon. The $\bar{K}N$ interaction in the isospin $I = 0$ channel is exceptionally strong—roughly several to tens of times stronger than the typical nuclear force—and is among the most significantly attractive hadron–hadron interactions known. This strong attraction is responsible for the formation of the $\Lambda(1405)$, a resonance located below the $\bar{K}N$ threshold. However, the $\Lambda(1405)$ cannot be accommodated within a simple three-quark model: it emerges as a dynamically generated state arising from coupled-channel interactions. Its internal structure, line shapes, and pole positions all indicate that it is an exotic hadronic molecule rather than a conventional baryon.

Beyond ordinary nuclei composed solely of nucleons, the study of nuclei in which a hadron other than a nucleon is embedded has developed into a major frontier of hadronic physics. A variety of exotic bound systems—including pionic, ϕ-mesic, and η'-mesic nuclei, as well as hypernuclei containing Λ, Σ, or Ξ hyperons—have provided invaluable insights into the strong interaction and the behavior of hadrons in a dense nuclear environment. Such systems serve as sensitive probes of in-medium modifications of hadron properties, revealing how mass, decay widths, and interaction strengths evolve when embedded in nuclear matter. Within this broader context, the study of antikaon - nuclear bound systems is particularly compelling. Because the $\bar{K}N$ interaction is both strongly attractive and strongly absorptive, kaonic nuclei offer a uniquely rich testing ground in which the interplay between binding dynamics, multi-nucleon absorption, and coupled-channel effects can be explored in a controlled manner. Investigations of $\bar{K}$-nuclear systems thus complement and extend the insights obtained from other mesic and hyperonic nuclei, providing a unique perspective on non-perturbative QCD

dynamics in the strangeness sector.

The complexity seen in the $\bar{K}N$ interaction becomes even richer when an antikaon is embedded in a nuclear environment. Few-body systems such as the $\bar{K}NN$ cluster and more extended kaonic nuclei highlight how the presence of a strongly interacting $\bar{K}$ can drastically modify the nuclear many-body dynamics. In such systems, the attractive $\bar{K}N$ interaction competes with multi-nucleon absorption processes, giving rise to nontrivial spectral properties and significant imaginary components in the effective optical potential. These features make antikaon–nuclear systems an ideal laboratory for probing dense nuclear matter, as the $\bar{K}$ can access high-density regions unreachable by ordinary nuclear probes.

Furthermore, the kaon occupies a special place in the chiral SU(3) sector of QCD as one of the Nambu - Goldstone bosons associated with spontaneous chiral symmetry breaking. Its in-medium modification may therefore carry direct information about the partial restoration of chiral symmetry in dense matter. In the astrophysical context, the possibility of kaon condensation in the interior of neutron stars has long been discussed, linking the microscopic $\bar{K}N$ interaction to the macroscopic equation of state of dense stellar matter. Recent observations of heavy neutron stars make this connection even more compelling, suggesting that a precise understanding of the antikaon interaction is essential for constraining the behavior of matter at supranuclear densities.

In this way, the study of the $\bar{K}N$ and $\bar{K}$–nuclear interactions touches upon a wide range of scales—from hadronic structure and nuclear few-body dynamics to the physics of dense matter in the universe. The present thesis aims to advance this understanding by quantitatively constraining the strength and absorptive properties of the $\bar{K}N$ interaction inside nuclei, thereby providing new insights into the structure of kaonic nuclear systems.

A central tool for describing the interaction between an antikaon and a nucleus is the $\bar{K}$–nucleus optical potential. Despite extensive efforts over several decades, its magnitude and density dependence remain poorly constrained. The real part of the potential has long been debated in terms of “deep” versus “shallow” solutions, with different experimental and theoretical approaches supporting competing interpretations. The imaginary part, which reflects one-nucleon and multi-nucleon absorption processes of the $\bar{K}$ in the nuclear medium, is equally important: it encodes information about

the in-medium dynamics at high density and is intrinsically linked to the real part through dispersion relations. However, current empirical constraints on the absorptive strength rely almost exclusively on analyses of kaonic-atom X-ray data, leaving large uncertainties in the region relevant to nuclear-density interactions.

Motivation of This Study

In this context, the measurement of the kaon escape process in the J-PARC E42 experiment provides a direct probe of the imaginary part of the $\bar{K}$–nucleus optical potential. By accessing absorption mechanisms that cannot be constrained by kaonic-atom X-ray data alone, the escape process offers new sensitivity to the in-medium $\bar{K}N$ dynamics across nuclear densities. This dissertation focuses on exploiting this observable—measured for the first time in E42—to quantitatively determine the absorptive strength of the $\bar{K}$-nuclear interaction. By establishing a robust constraint on the imaginary component of the potential, the present work aims to provide a decisive benchmark for theoretical models and to advance the broader effort to understand the role of antikaons in dense nuclear matter.

1.2 $\bar{K}N$ Interaction and $\Lambda(1405)$

1.2.1 $\bar{K}N$ Interaction at Low Energy

A quantitative understanding of the elementary antikaon-nucleon ($\bar{K}N$) interaction in vacuum is the foundation for describing more complex systems of kaonic matter, such as kaonic atoms and kaonic nuclei. Especially, the interaction is characterized by significant coupling between different meson-baryon channels (e.g., $\pi\Sigma$) and has two isospin components, $I = 0$ and $I = 1$. The $I = 0$ $\bar{K}N$ channel is of particular interest as it exhibits an attraction significantly stronger than the other hadron-hadron interactions. This exceptionally strong force is the primary driver behind the rich and complex phenomena observed in kaonic matter, making it a compelling and challenging field of study.

Information on the low-energy $\bar{K}N$ interaction has been obtained from studies of K^-p scattering. A detailed analysis by Martin evaluated the scattering lengths through a self-consistent M-matrix treatment, incorporating the strongly coupled meson–baryon

channels characteristic of the $\bar{K}N$ system [1]. The analysis included the elastic reaction $K^-p \to K^-p$, the charge-exchange process $K^-p \to \bar{K}^0n$, and several inelastic channels such as $K^-p \to \Lambda\pi^0$, $\Sigma^0\pi^0$, and $\Sigma^\pm\pi^\mp$ measured in [2–4]. Dispersion relations constrained by $K^\pm p$ and $K^\pm n$ scattering data (see Fig. 1.1) were employed to extract the threshold scattering lengths[1]

$$\begin{aligned} a^{I=0} &= -1.70 + i\,0.65 \text{ fm}, \\ a^{I=1} &= \quad 0.37 + i\,0.60 \text{ fm}, \end{aligned} \tag{1.1}$$

which represent the $\bar{K}N$ scattering lengths in the isospin $I = 0$ and $I = 1$ channels, respectively.

Additional constraints on the $\bar{K}N$ interaction come from X-ray spectroscopy of kaonic hydrogen, in particular from the K_α transition ($2p \to 1s$). The deviation of the measured $1s$ energy from the pure electromagnetic value ($\Delta E_{1s} = E_{1s}^{\text{measured}} - E_{1s}^{\text{e.m.}}$) and the strong-interaction width Γ_{1s} of the ground state provide direct information on the S-wave $\bar{K}N$ scattering at threshold. These observables can be confronted with the K^-p scattering amplitudes. The corresponding scattering length is related to ΔE_{1s} and Γ_{1s} via the Deser-type relation [5, 6]:

$$\Delta E_{1s} + i\,\frac{\Gamma_{1s}}{2} = 2\alpha^3\mu^2 a_{K^-p}, \tag{1.2}$$

$$a_{K^-p} = \frac{1}{2}\left(a^{I=0} + a^{I=1}\right), \tag{1.3}$$

where α is the fine-structure constant and μ denotes the reduced mass of the K^-p system.

Historically, the scattering length inferred from kaonic-hydrogen measurements had not agreed with the value extracted from Martin's analysis until the late 1990s. The disagreement was most evident in the sign of the real part of the amplitude, a long-standing issue often referred to as the "kaonic hydrogen puzzle."

The long-standing "kaonic hydrogen puzzle" was resolved by the KEK-PS E228 (KpX) experiment in 1997. By employing a gaseous hydrogen target to suppress Stark

[1] The scattering length a is defined as the low-energy limit of the scattering amplitude, $f(k \to 0) = a$. In this convention, a positive real part ($\text{Re}(a) > 0$) indicates an attractive interaction. A negative real part ($\text{Re}(a) < 0$) possibly corresponds to a repulsive one or bound state.

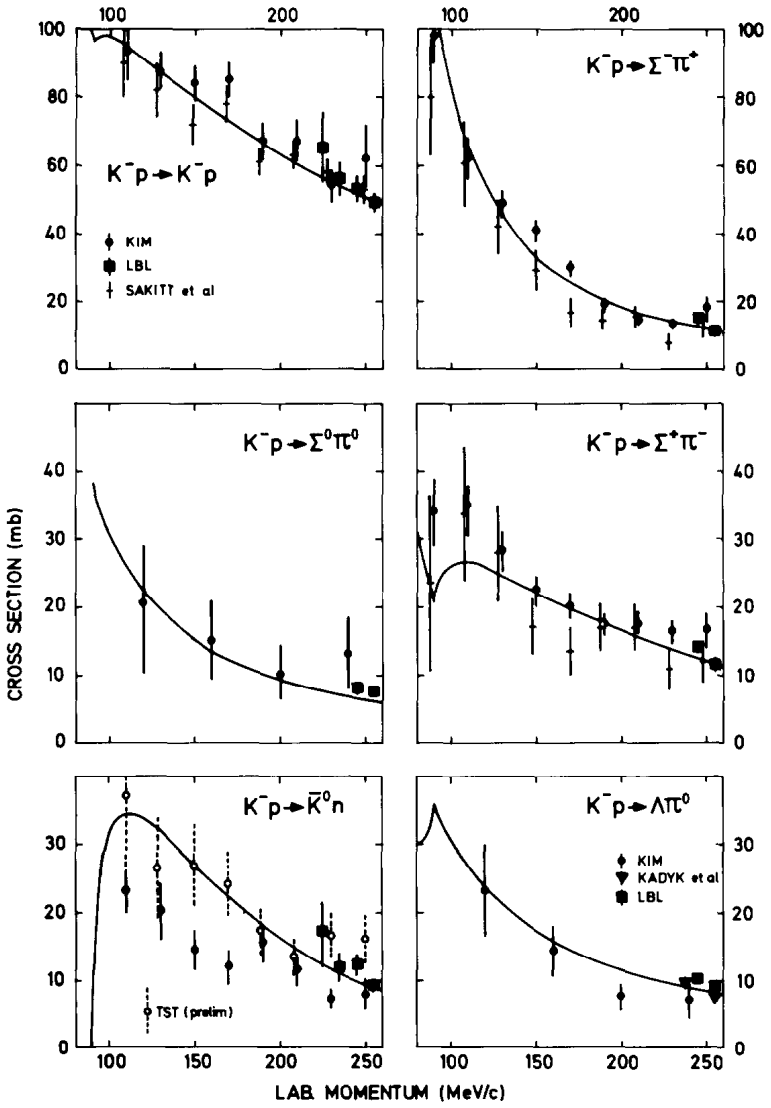

Figure 1.1: Schematic overview of the low-energy $\bar{K}N$ scattering channels incorporated in Martin' s M-matrix analysis. Elastic ($K^-p \to K^-p$), charge-exchange ($K^-p \to \bar{K}^0n$), and inelastic channels ($\Lambda\pi$, $\Sigma\pi$) are shown together with the dispersion-relation constraints from $K^\pm p$ and $K^\pm n$ data used to extract the threshold scattering lengths. This figure is taken from [1].

effect, the experiment succeeded in observing a distinct K_α X-ray peak [7]. Subsequently, the DEAR collaboration reported new kaonic-hydrogen measurements [8], whose extracted values were broadly consistent with those obtained in the E228 study.

More recently, the SIDDHARTA experiment at DANE has achieved a high-precision measurement of the kaonic-hydrogen X-ray spectrum using silicon drift detectors (SDDs). The SDDs provided an energy resolution of approximately 150 eV and a timing resolution of about 1 μs, enabling a significant improvement in the determinations of ΔE_{1s} and Γ_{1s} to be $\Delta E_{1s} = -283 \pm 36$ (stat.) $\pm$ 6 (syst.) eV and the width as $\Gamma_{1s} = 541 \pm 89$ (stat.) $\pm$ 22 (syst.) eV [9]. The negative sign of the energy shift provides direct and unambiguous evidence that the $K^- p$ interaction at threshold is strongly attractive. These experimental results are summarized in Fig. 1.2.

Figure 1.2 also includes recent theoretical predictions based on coupled-channel calculations employing chiral effective field theory (chiral unitary approach), with interaction kernels constructed up to next-to-leading order (NLO) [10–13]. These theoretical studies further address the extrapolation of the $\bar{K}N$ amplitude into the sub-threshold region.

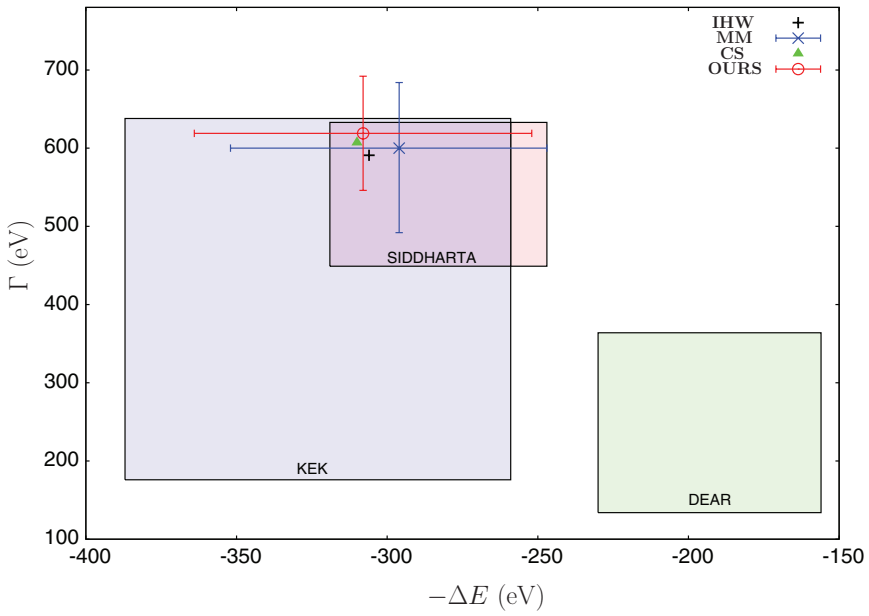

Figure 1.2: Comparison of the kaonic-hydrogen ΔE_{1s} and Γ_{1s} values reported by three experimental groups (adapted from Ref. [14]). The data with their uncertainties are shown as rectangles corresponding to the KEK-PS E228 [7], DEAR [8], and SIDDHARTA [9] measurements. Recent theoretical predictions are also displayed using a black plus symbol [10, 11], a blue cross [12], a green filled triangle [13], and a red open circle [14].

A representative example is shown in Fig. 1.3, which is taken from Ref. [15]. Theoretical models reproduce existing experimental observables—kaonic-hydrogen data, K^-p cross sections, and branching ratios—reasonably well, although the detailed fitting strategies differ among groups.

However, as illustrated in Fig. 1.3, notable deviations appear in the extrapolated amplitudes below threshold, reflecting differences in model assumptions and parameterizations [13, 15]. Consequently, the $\bar{K}N$ interaction in the subthreshold energy region remains insufficiently constrained, and new experimental input is required to reduce these uncertainties, because the SIDDHARTA result constrains only the above-threshold, physical region.

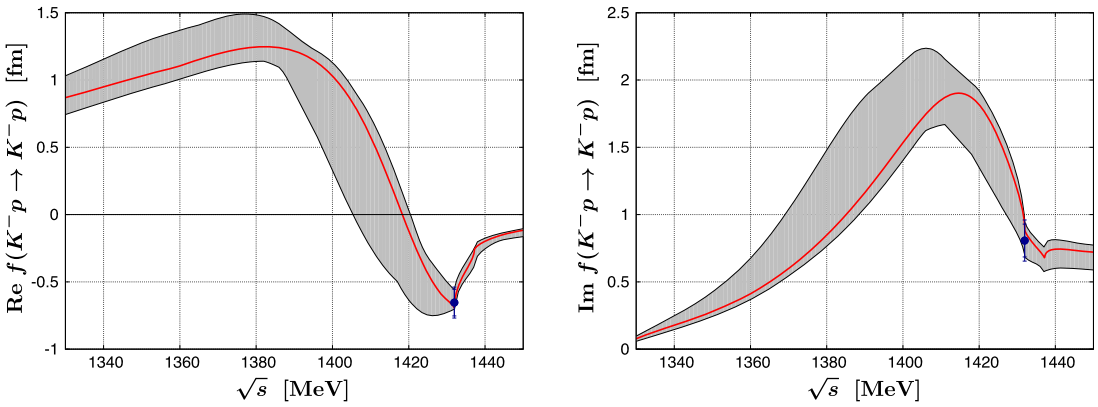

Figure 1.3: Real (left) and imaginary (right) parts of the $K^-p \to K^-p$ forward scattering amplitude extrapolated into the subthreshold region. The SIDDHARTA constraints are shown as points with statistical and systematic uncertainties. The shaded bands denote theoretical uncertainties. This figure is taken from [15].

The strong $\bar{K}N$ attraction in the $I = 0$ channel is believed to give rise to a quasi-bound state, which manifests as the $\Lambda(1405)$ resonance, appearing just below the $\bar{K}N$ mass threshold.

Recently, the ALICE Collaboration reported the K^-p correlation function measured via femtoscopy in pp collisions at the LHC, accessing the low relative momentum region

that is difficult to probe with conventional scattering experiments [16]. This measurement demonstrated the strong attractive interaction of the K^-p pair and observed a cusp structure at the $\bar{K}^0 n$ threshold, providing crucial constraints on the $\bar{K}N$ dynamics and coupled-channel effects.

1.2.2 $\Lambda(1405)$: $\bar{K}N$ Molecular Picture and Two-pole Nature

The $\Lambda(1405)$ resonance, with strangeness $S = -1$, isospin $I = 0$, and spin-parity $J^P = 1/2^-$, plays a central role in understanding the low-energy $\bar{K}N$ interaction. The pole position of the bound state is estimated using the $\bar{K}N$ scattering length for isospin $I = 0$, $a^{I=0} = -1.70 + i0.65$ fm, obtained from the analysis of scattering cross sections by A.D. Martin [1]. Here, assuming the relationship $k = 1/(ia)$ between the scattering length a and the wave number k, the value is converted to the complex energy plane using the non-relativistic relation $k^2 = 2\mu E$, where μ is the reduced mass. From this derivation, the pole position is calculated to be $E = 1418.4 - i12.1$ MeV, corresponding to a state with a central value of 1418.4 MeV and a half-width of 12.1 MeV. This is considered to correspond approximately to the higher pole of the $\Lambda(1405)$.

Experimentally, it appears as a broad resonance located significantly below the $\bar{K}N$ threshold ($\approx$ 1432 MeV/c^2) and is observed primarily through its $\pi\Sigma$ decay channel. When parameterized with a simple Breit–Wigner form, the resonance shows a nominal mass of approximately 1405 MeV/c^2 and a width of about 50 MeV [17]. However, its dynamical origin and internal structure have long been subjects of extensive discussion.

Early constituent-quark models, which describe the $\Lambda(1405)$ as an orbitally excited *uds* baryon, predict a mass significantly higher (around 1500 MeV) and fail to account for the experimental value around 1400 MeV. The lowest negative-parity excitation of the nucleon is the $N(1535)$, whose mass lies above that of the $\Lambda(1405)$. This implies that the $\Lambda(1405)$, which contains an s quark, is lighter than the $N(1535)$ composed only of u and d quarks—an ordering opposite to the naive expectation of constituent quark models. In such models, the $J^P = 1/2^-$ and $J^P = 3/2^-$ states are regarded as LS-partner states formed by coupling the same quark-spin configuration ($S = 1/2$) to different orbital angular momenta. For the nucleon, the mass splitting between the $N(1535)$ and $N(1520)$, about 15 MeV, is interpreted as the corresponding LS separation. The analogous excited Λ states, $\Lambda(1405)$ and $\Lambda(1520)$, are separated by more than 100 MeV,

a value far larger than expected from the quark-model viewpoint. These discrepancies suggest that the $\Lambda(1405)$ is not well accommodated within a simple three-quark picture and may instead possess a more complex structure beyond a conventional qqq configuration, but as a quasi-bound $\bar{K}N$ state strongly coupled to the open $\pi\Sigma$ channel.

Coupled-channel calculations based on chiral SU(3) dynamics provide a natural theoretical foundation for this molecular interpretation. A major conclusion in this framework is that the $\Lambda(1405)$ is not a single resonance but rather the superposition of *two distinct poles* on the complex energy plane. Jido *et al.* [18] and other related studies [19] revealed the following structure:

- **Higher-mass pole** ($\sim$ 1420 MeV) with a narrower width, coupling strongly to the $\bar{K}N$ channel and,
- **Lower-mass pole** ($\sim$ 1380 MeV) with a broader width, coupling predominantly to the $\pi\Sigma$ channel.

This two-pole structure has become a cornerstone of the modern theoretical description of the $\Lambda(1405)$. A more refined NLO chiral coupled-channel analysis by Ikeda, Hyodo, and Weise (IHW) [20] further quantified the pole positions with improved precision, confirming the robustness of this picture, where the higher-mass pole, which couples strongly to the $\bar{K}N$ channel, was found to have a mass of 1424^{+23}_{-23} MeV and a width of 26^{+14}_{-30} MeV and the lower-mass pole, coupling almost exclusively to the $\pi\Sigma$ channel, was determined to have a mass of 1381^{+18}_{-18} MeV with a width of 102^{+18}_{-28} MeV.

The two-pole nature of the $\Lambda(1405)$ has profound implications. Since different reaction mechanisms couple differently to the $\bar{K}N$ and $\pi\Sigma$ channels, the observed $\pi\Sigma$ invariant-mass spectrum—often referred to as the "lineshape"—varies significantly depending on the production process. This channel dependence, observed in kaon-induced reactions, photoproduction, and proton–proton collisions, provides strong suggestion supporting the two-pole scenario.

1.2.3 Experimental Research on $\Lambda(1405)$ Structure

If the $\Lambda(1405)$ indeed consists of two nearby poles with distinct coupling strengths to the $\bar{K}N$ and $\pi\Sigma$ channels, as predicted by chiral coupled-channel dynamics, then its observed $\pi\Sigma$ invariant-mass spectrum (the "lineshape") must depend sensitively on

how the resonance is produced. Different reaction mechanisms excite the $\bar{K}N$ and $\pi\Sigma$ channels with different weights; consequently, the contribution of each pole varies from reaction to reaction. A wide range of experimental studies over the past decades has established this reaction dependence, providing strong suggestion for the two-pole scenario and the molecular $\bar{K}N$ origin of the $\Lambda(1405)$.

J-PARC E31 experiment investigated the subthreshold $\bar{K}N$ interaction and the pole structure of the $\Lambda(1405)$ through measurements of the $d(K^-, n)\pi\Sigma$ reaction [21]. By employing a two-step mechanism in a deuteron target, the experiment accessed the S-wave $\bar{K}N$ amplitude below threshold, which is not reachable by ordinary K^-p scattering.

A 1 GeV/c K^- beam was directed onto a liquid deuterium target. Forward neutron emission ($\theta_n < 6^\circ$) produced a low-momentum $\bar{K}$ ($\sim$ 250 MeV/c), which subsequently interacted with the spectator nucleon in an S-wave dominated kinematic region. Charged particles, neutrons, and decay products from the $\pi\Sigma$ final states were reconstructed.

Invariant-mass spectra were obtained for the $\pi^+\Sigma^-$, $\pi^-\Sigma^+$, $\pi^0\Sigma^0$, and $\pi^-\Sigma^0$ channels. Their distinct line shapes reflect different mixtures of $I = 0$ and $I = 1$ amplitudes. The $\pi^0\Sigma^0$ mode provided a clean $I = 0$ component, consistent with the isospin relation verified using the combination $(\pi^+\Sigma^- + \pi^-\Sigma^+ - \pi^-\Sigma^0)/2$.

The spectra were analyzed using the two-step reaction formalism, with the S-wave $\bar{K}N$ amplitude modeled by an effective-range expansion. A simultaneous fit to the $\pi^0\Sigma^0$ spectrum yielded the scattering length $a_{I=0} = -1.22 + i0.79$ fm and the effective range $r_{e,I=0} = 0.53 - i0.66$ fm. The fitted amplitude revealed a resonance pole at

$$z_{\rm pole} = 1417.7^{+6.0+1.1}_{-7.4-1.0} - i\left(26.1^{+6.0+1.7}_{-7.9-2.0}\right)\ \text{MeV},$$

which lies much closer to the higher pole. The strong $\bar{K}N$ coupling, $|T_2^{I=0}(\bar{K}N \to \bar{K}N)|^2/|T_2^{I=0}(\bar{K}N \to \pi\Sigma)|^2 \approx 2.2$, supports the interpretation of the $\Lambda(1405)$ as a quasi-bound $\bar{K}N$ molecular state.

The E31 result provides the first direct determination of the subthreshold $I = 0$ $\bar{K}N$ S-wave amplitude. The extracted pole position agrees with the higher pole predicted by chiral SU(3) dynamics and offers an essential constraint on low-energy $\bar{K}N$ interactions relevant to kaonic nuclear systems.

The LEPS experiment measured the hyperon resonances $\Lambda(1405)$ and $\Sigma^0(1385)$ via the photoproduction on the proton using 1.5–2.4 GeV photons [22]. Data were taken in the forward kinematic region, $0.8 < \cos\theta_K^{\mathrm{CM}} < 1.0$, where K^+Y^* production is enhanced and clean missing-mass spectra can be obtained.

A K^+ was detected with the LEPS spectrometer, and the missing mass $MM(K^+)$ was reconstructed. To separate the overlapping $\Lambda(1405)$ and $\Sigma^0(1385)$ contributions, additional data with a time-projection chamber (TPC) were analyzed, allowing identification of their decay channels:$\Lambda(1405) \rightarrow \Sigma^{\pm}\pi^{\mp}, \Sigma^0(1385) \rightarrow \Lambda\pi^0$. By combining decay topology, branching ratios, and detector efficiencies, the production ratio $\Lambda(1405)/\Sigma^0(1385)$ was experimentally determined and used to decompose the missing-mass spectra.

The $\Lambda(1405)$ spectra in the $\Sigma^+\pi^-$ and $\Sigma^-\pi^+$ channels showed distinct line shapes, reflecting strong interference between the $I = 0$ and $I = 1$ components of the $\pi\Sigma$ amplitude. When the two modes were summed, the resulting line shape became consistent with theoretical expectations.

Differential cross sections were extracted for both $\Lambda(1405)$ and $\Sigma^0(1385)$. $\Lambda(1405)$ production is enhanced near threshold but decreases rapidly with increasing photon energy, while $\Sigma^0(1385)$ production remains relatively stable. The measured production ratios ($\Lambda(1405)/\Sigma^0(1385)$) are

$$0.54 \pm 0.17 \quad (1.5 < E_\gamma < 2.0 \text{ GeV}), \qquad 0.084 \pm 0.076 \quad (2.0 < E_\gamma < 2.4 \text{ GeV}).$$

These results provide the first separated photoproduction cross sections of $\Lambda(1405)$ and $\Sigma^0(1385)$. The mode-dependent line shapes confirm strong isospin interference in the $\Lambda(1405)$ decay, and the observed energy dependence suggests differences in the underlying reaction mechanisms and internal structure between the two hyperon resonances.

The CLAS experiment at Jefferson Lab performed high-statistics measurements of the $\Sigma\pi$ invariant-mass distributions in the $\Lambda(1405)$ region using tagged real photons in the reaction $\gamma p \rightarrow K^+\Sigma\pi$ for $1.95 < W < 2.85$ GeV [23]. This dataset provided, for the first time, simultaneous coverage of all three charge combinations ($\Sigma^+\pi^-$, $\Sigma^0\pi^0$, and $\Sigma^-\pi^+$), enabling a detailed comparison of their line shapes. A bremsstrahlung photon beam was incident on a liquid-hydrogen target, and charged

particles were reconstructed with drift chambers and time-of-flight detectors, while π^0 and neutrons were identified using missing-mass and kinematic-fit techniques.

Invariant-mass spectra of the $\Sigma\pi$ system were extracted in nine W bins and summed over kaon angles. Backgrounds from $\Sigma(1385)$, K^* production, and higher hyperon states were modeled and subtracted using Monte Carlo templates, leaving distributions associated with the structure traditionally referred to as the $\Lambda(1405)$. A simple relativistic Breit–Wigner function fails for all channels, and a Flatté-type parametrization was introduced to incorporate the strong $N\bar{K}$ threshold behavior near 1435 MeV. Empirical templates of the $\Lambda(1405)$ line shapes were iteratively constructed from acceptance-corrected residuals. A phenomenological isospin decomposition was then applied, assuming coherent interference between $I = 0$ and $I = 1$ amplitudes.

The three charge combinations display markedly different line shapes, with variations well beyond statistical and systematic uncertainties, demonstrating significant $I = 0$–$I = 1$ interference. The $\Sigma^+\pi^-$ channel peaks near 1420 MeV with a relatively narrow width, whereas $\Sigma^-\pi^+$ is shifted to lower mass and is considerably broader. The best global description requires one $I = 0$ component and two distinct $I = 1$ amplitudes, whose extracted centroids are

$$m_{I=0} \approx 1338 \text{ MeV}, \qquad m_{I=1}^{(\text{narrow})} \approx 1413 \text{ MeV}, \qquad m_{I=1}^{(\text{broad})} \approx 1394 \text{ MeV}.$$

The $I = 0$ amplitude peaks essentially at the $\Sigma\pi$ threshold, consistent with a picture in which coupled-channel dynamics dominate the observed $\Lambda(1405)$ line shape rather than a single isolated Breit–Wigner pole. The $I = 1$ contributions are also sizeable, reaching roughly half the magnitude of the $I = 0$ amplitude at higher W.

These findings show that the structure known as the $\Lambda(1405)$ cannot be treated as a single $I = 0$ resonance near 1405 MeV. Instead, the observed spectra arise from strong $\bar{K}N$–$\Sigma\pi$ coupled-channel effects together with significant $I = 1$, $J^P = 1/2^-$ amplitudes. The results support interpretations consistent with a two-pole nature of the $\Lambda(1405)$ and provide the most detailed experimental determination of $\Sigma\pi$ line shapes to date, offering essential constraints for theoretical studies of the $\Lambda(1405)$ and nearby hyperon dynamics.

The CLAS Collaboration also reported the result of the $\Lambda(1405)$ line shape analysis in the electroproduction using a 5.5 GeV electron beam [24]. The reaction

was $e^- p \to e^- K^+ \Lambda(1405)$, with the hyperon reconstructed through the decay chain $\Lambda(1405) \to \Sigma^+\pi^- \to p\pi^0\pi^-$. Final-state particles (e^-, K^+, p, and π^-) were detected directly, while the π^0 was identified via the missing-mass technique. The analysis was carried out over the virtual-photon momentum-transfer range $1.0 < Q^2 < 3.0$ (GeV/c)^2 and for hadronic momentum transfers $0.5 < -t < 4.5$ (GeV/c)^2.

The invariant-mass spectra of the $\Sigma^+\pi^-$ final state show a pronounced dependence on Q^2. At low Q^2 the line shape is weak, but for $Q^2 > 1.5$ (GeV/c)^2 two distinct structures emerge: a narrow peak near 1420 MeV and a broader enhancement around 1365–1380 MeV. These features cannot be reproduced by a single Breit–Wigner amplitude. Fits using the PDG parameters fail, and even a free single Breit–Wigner yields poor agreement. A model employing two incoherent Breit–Wigner amplitudes successfully describes the observed line shape, yielding resonance centroids

$$m_{\text{high}} = 1423 \pm 2 \text{ MeV}, \qquad m_{\text{low}} = 1368 \pm 4 \text{ MeV},$$

consistent with the two-pole structure predicted by chiral SU(3) unitary approaches, in which the higher-mass pole couples mainly to $\bar{K}N$ and the lower-mass pole couples predominantly to $\pi\Sigma$. The relative strength of the higher-mass component increases with Q^2, indicating that virtual photons preferentially excite the $\bar{K}N$-dominated pole.

In summary, taken together, the experimental results from hadronic, photoproduction, and electroproduction reactions provide a coherent and quantitatively consistent picture of the $\Lambda(1405)$ as a strongly coupled $\bar{K}N$ - $\pi\Sigma$ system whose observed spectral shape depends sensitively on the production mechanism and the isospin composition of the final state. The hadronic measurement by J-PARC E31 has established, for the first time, the subthreshold $I = 0$ $\bar{K}N$ S-wave amplitude and located the associated pole near 1420 MeV, demonstrating that the dominant $\bar{K}N$ component of the $\Lambda(1405)$ resides significantly above the nominal 1405 MeV value. Photoproduction data from LEPS and CLAS have revealed large charge-dependent variations in the $\Sigma\pi$ line shapes, far exceeding statistical and systematic uncertainties and requiring substantial interference between $I = 0$ and $I = 1$ amplitudes. These results show unambiguously that the observed mass spectra cannot be interpreted as those of a single, isolated resonance. The electroproduction study by CLAS further demonstrates a strong Q^2 dependence, in which virtual photons increasingly emphasize the higher-mass, $\bar{K}N$-dominated pole,

thereby exposing the reaction-dependent projection of the underlying coupled-channel structure.

The combined evidence now strongly supports the two-pole picture predicted by chiral SU(3) dynamics: a narrow, predominantly $\bar{K}N$ pole around 1420 MeV and a broader, mostly $\pi\Sigma$ pole near 1360 - 1380 MeV. In this framework, the apparent mass of the $\Lambda(1405)$ is not a fixed property but rather an emergent feature shaped by the interplay of channel couplings, interference between isospin amplitudes, and the specific dynamics of the production reaction. This modern understanding provides a solid foundation for contemporary studies of antikaon - nucleon interactions and for exploring few-body kaonic nuclear systems such as the K^-pp state.

1.3 $\bar{K}NN$ System

Interpreting the $\Lambda(1405)$ resonance as a $\bar{K}N$ bound state, the $\bar{K}NN$ system is proposed as a natural extension, driven by the same strong $\bar{K}N$ attraction. This section provides an overview of the theoretical predictions and the current status of experimental searches for the so-called "K^-pp" state, which is regarded as the simplest kaonic nucleus and a natural extension of the $\Lambda(1405)$ led by $\bar{K}N$ attraction with $I = 0$.

1.3.1 Experimental Search for the K^-pp State

The existence of the K^-pp bound state, the simplest kaonic nuclear system if it exists, has been the subject of a long-standing and complex experimental search, which for many years did not yield a consistent picture. Early experiments such as FINUDA (stopped K^- reactions) [25] and DISTO ($pp \to p\Lambda K^+$ reaction at 2.85 GeV) [26] reported structures suggesting the existence of a "deep" bound state, with binding energies reported as $B_K = 115^{+6}_{-5}(\text{stat.})^{+3}_{-4}(\text{syst.})$ MeV and $B_K = 103\pm3(\text{stat.})\pm5(\text{syst.})$ MeV, respectively. However, their interpretations were debated. The peak structure reported by the FINUDA collaboration was later reinterpreted as a kinematic artifact caused by final state interactions, specifically involving the two-step process of $K^-NN \to \Sigma N$ absorption followed by the $\Sigma N \to \Lambda p$ conversion. This mechanism naturally reproduces the observed spectrum without invoking a deeply bound K^-pp state. The validity of the DISTO result was questioned due to the analysis method, in which the signal was ex-

tracted by dividing the measured spectrum by a simple phase-space simulation, and that interpretation was debated also due to challenges in handling backgrounds, such as the contribution from N^* resonances later pointed out by the HADES experiment [27, 28]. The OBELIX experiment at CERN [29, 30] reported a low-mass enhancement in the Λp invariant mass spectrum from $\bar{p}\,^4$He annihilation. However, similar to the FINUDA result, this structure can be explained by kinematic effects and final state interactions, such as the $\Sigma N \to \Lambda p$ conversion, without invoking a deeply bound state. The LEPS experiment reported null observations in the inclusive measurement [31]. Similarly, in the π^+-induced reaction (J-PARC E27), no significant structure was observed in the inclusive spectrum. However, in the coincidence measurement, they reported findings consistent with the "deep" state ($B_K = 95.3^{+1.7}_{-1.8}(\text{stat.})^{+2.1}_{-4.6}(\text{syst.})$ MeV) [32].

This long-standing controversy was significantly addressed by the J-PARC E15 experiment [33–35]. It employed what was considered one of the most sensitive method for this search: the K^- induced reaction on a ^{3}He target. As a result, a statistically significant peak corresponding to a bound state was clearly observed. Its binding energy and decay width were determined with high precision to be

$$\begin{aligned} B_K &= 41.9 \pm 1.2(\text{stat.})^{+1.1}_{-0.8}(\text{syst.})\ \text{MeV}, \\ \Gamma &= 100.2 \pm 3.1(\text{stat.})^{+3.1}_{-1.9}(\text{syst.})\ \text{MeV}, \end{aligned} \tag{1.4}$$

respectively. The existence of this K^-pp bound state was thereby firmly established by E15.

The recent femtoscopic studies by the ALICE experiment in pp collisions have explored the $K^- - p - p$ correlation function [36]. While no contribution from a bound state was found, this result is not in direct contradiction with the E15 finding due to the fundamentally different production environment.

Future experiments such as E80/E89 at J-PARC are being prepared to search heavier kaonic system of K^-ppn ($\bar{K}NNN$) and determine the spin-parity of the state and search for its isospin partner, the $\bar{K}^0nn$ state, promising a more complete understanding of the $\bar{K}NN$ system.

1.3.2 Theoretical Research on the K^-pp State

Theoretical investigations of the K^-pp state have been extensively conducted employing various frameworks, which differ primarily in their treatment of the $\bar{K}N$ interaction and the few-body calculation techniques utilized in [37–46]. Broadly, the $\bar{K}N$ interaction models are categorized into two types: energy-dependent potentials based on chiral SU(3) dynamics [38–41, 44, 46], and, energy-independent phenomenological potentials [37, 42, 43, 45]. Regarding the calculation methods, variational approaches and Faddeev coupled-channel methods are commonly adopted.

A systematic comparison of these theoretical predictions reveals a characteristic dependence on the interaction model. Calculations based on chiral SU(3) dynamics (energy-dependent potentials) generally predict relatively a shallow binding energy and a broad decay width. For instance, Doté, Hyodo, and Weise [39, 40] performed a variational calculation and reported a binding energy of $B_{K^-pp} \sim 20$ MeV with a width of $\Gamma_{K^-pp} \sim 40$–70 MeV. The decay width is comparable to or larger than the binding energy, which implies that the experimental observation of such a state as a distinct peak would be difficult.

In contrast, calculations utilizing energy-independent potentials tend to yield deeper binding energies. For instance, the pioneering work by Akaishi and Yamazaki [37] employing such a potential predicted the existence of deeply bound kaonic nuclear states, including the K^-pp system, by constructing a phenomenological energy-independent $\bar{K}N$ potential based on the ansatz that the $\Lambda(1405)$ resonance is a $\bar{K}N$ bound state. Using a G-matrix approach and variational calculations, they demonstrated that the strong attraction in the $I = 0$ $\bar{K}N$ channel, necessary to reproduce the $\Lambda(1405)$ mass, leads to the formation of dense, deeply bound states. Specifically, for the K^-pp system (experimentally searched for as a K^-pp state), their model predicted a deeply bound state with a binding energy of $B_{K^-pp} \sim 48$ MeV and a relatively narrow width of 61 MeV, formed within a highly contracted nuclear core with a density significantly higher than normal nuclear density. Consistent results were obtained by Maeda *et al.* [47] using rigorous Faddeev-Yakubovsky calculations, which yielded $B_{K^-pp} \sim 51.5$ MeV. Similarly, Shevchenko *et al.* [42, 43] reported binding energies in the range of 50–70 MeV and $\sim$ 100 MeV of the decay width when employing phenomenological potentials. Although these models yield deeper bindings than chiral dynamics, they still fall

short of the significantly larger values ($B > 100$ MeV) reported by early experimental searches such as FINUDA [25], DISTO [26], and OBELIX [29, 30]. This significant discrepancy between the "deep" values reported in early experiments and the "shallow" to "moderate" range supported by theoretical consensus highlighted a fundamental contradiction in the understanding of the kaonic nuclear system, underscoring the necessity for definitive experimental verification.

In this context, Maeda, Akaishi, and Yamazaki [47] investigated the implications of such strong interactions using rigorous Faddeev-Yakubovsky calculations. They reported that if the $\bar{K}N$ interaction is enhanced to reproduce the DISTO result, it leads to interesting consequences in other systems; specifically, double kaonic nuclei like K^-K^-pp would undergo drastic shrinkage, forming extremely dense and deeply bound states.

1.4 $\bar{K}$-Nucleus System

In this section, we extend our discussion to $\bar{K}$-nucleon multi-body systems beyond the K^-pp state. A variety of experimental and theoretical approaches have been employed to explore the properties of antikaons nucleus interaction. Here, we overview three key areas of research: (1) experimental and theoretical studies of kaonic atoms, which probe the interaction almost at the nuclear surface; (2) experimental searches for bound states and study of reaction mechanisms using stopped kaon absorption; and (3) spectroscopic studies via in-flight kaon reactions. These studies collectively provide a broader context for understanding the $\bar{K}$-nucleus interaction.

1.4.1 X-ray Spectroscopy of Kaonic Atom

As discussed in Sec. 1.2.1, experimental and theoretical studies of kaonic atom X-rays are extremely useful for extracting the $\bar{K}$-nucleon ($\bar{K}N$) interaction from kaonic hydrogen data, and the same for determining the $\bar{K}$-nucleus interaction. In particular, the data on atomic level shifts and widths reflect the nature of the interaction in the low-density region, thereby imposing constraints on the potential depth, which serves as the basis for discussions on deeply bound states. Since the kaonic hydrogen system has already been discussed in the context of the elementary $\bar{K}N$ interaction, we begin

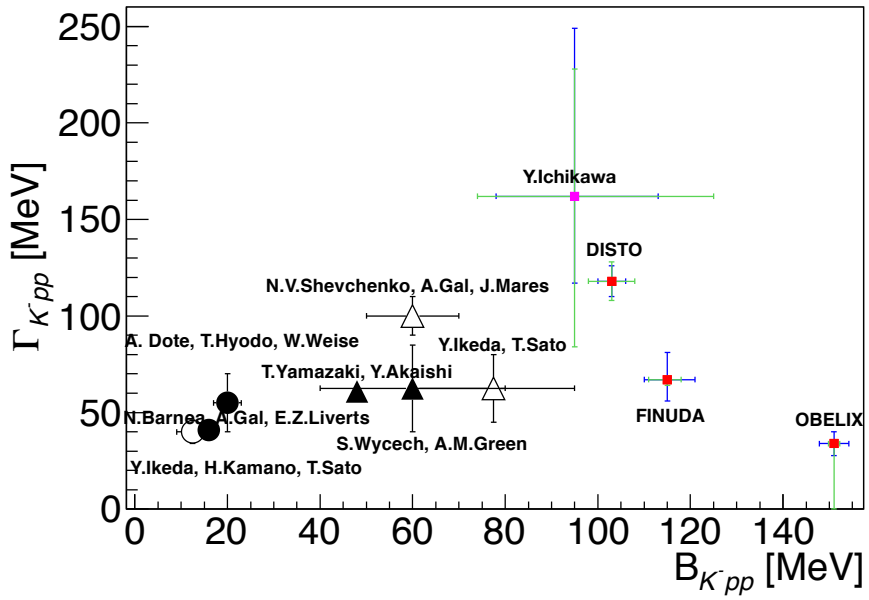

Figure 1.4: Binding energies and widths of the K^-pp system obtained from different theoretical predictions [38–46, 48] and experimental measurements are compared. Results derived from chiral SU(3)-based energy-dependent potentials are displayed as circles, while those calculated with energy-independent potentials are represented by triangles. Experimental determinations from J-PARC E15 [33–35], J-PARC E27 [32], FINUDA [25], DISTO [26], and OBELIX [29, 30] are shown as red or magenta squares. For the experimental points, blue and green bars denote statistical and systematic uncertainties, respectively. This figure is taken from [49].

this overview with kaonic deuterium, followed by kaonic atoms in heavier nuclei.

X-ray Spectroscopy of $\bar{K} - d$ Atom

Experimental measurements of kaonic deuterium are technically challenging due to the expected low X-ray yield and broad spectral width caused by strong nuclear absorption. Currently, two major international projects are pursuing the first precision measurement of the 1s state shift and width to resolve the isospin dependence of the $\bar{K}N$ interaction. The **SIDDHARTA-2 experiment** at the DAΦNE collider in Italy aims to perform high-precision spectroscopy using a gaseous target and large-area Silicon Drift Detectors (SDDs) with dedicated background suppression [50]. In parallel, the **J-PARC E57**

experiment utilizes the high-intensity kaon beam at the K1.8BR beamline [51]. Since J-PARC E57 operates under different beam conditions and background environments compared to SIDDHARTA-2, it provides a crucial independent measurement with different systematics. The combined results from these complementary experiments are expected to provide definitive values for the $\bar{K}N$ isospin-dependent scattering lengths through rigorous few-body calculations.

X-ray Spectroscopy of Heavier $\bar{K}$ Atoms

Kaonic atoms serve as a vital probe for investigating the $\bar{K}$-nucleus interaction in the low-energy regime. These systems are characterized as Coulomb-bound states of a K^- and a nucleus, which are significantly influenced by the strong interaction—effects that are observable via X-ray spectroscopy. Notably, high-precision measurements of kaonic helium isotopes (^{4}He and ^{3}He) were achieved by the KEK-PS E570 and SIDDHARTA collaborations [9, 52]. For kaonic atom systems heavier than deuterium (K^-d), rigorous few-body calculations have not yet been performed due to the complexity of the many-body problem. Instead, to derive the hadron-nucleus interaction from such experimental data, the standard $t\rho$ approximation is widely employed. This method utilizes the free-space zero-energy t matrix and the nuclear density ρ to perform global fits on extensive datasets using an optical potential $V_{\rm opt}$ within the Klein-Gordon equation:

$$[\Delta - 2\mu(B + V_{\rm opt} + V_c) + (V_c + B)^2]\Psi = 0, \tag{1.5}$$

where V_c represents the static Coulomb potential arising from the finite charge distribution of the nucleus, and μ denotes the reduced mass of the K^--nucleus system. The complex binding energy is defined as $B = B_{\bar{K}} + i\Gamma_{\bar{K}}/2$, where $B_{\bar{K}}$ and $\Gamma_{\bar{K}}$ correspond to the binding energy and width, respectively. The simple $t\rho$ optical potential is typically expressed as:

$$2\mu V_{\rm opt}(r) = -4\pi \left(1 + \frac{\mu}{m}\frac{A-1}{A}\right) b_0 \rho(r), \tag{1.6}$$

In this equation, m is the nucleon mass, $\rho(r)$ is the nucleon density distribution normalized to the mass number A, and b_0 acts as a fitting parameter equivalent to the $\bar{K}$-nucleon isoscalar scattering length in the impulse approximation. Analyses using

this basic $t\rho$ model typically yield "shallow" potentials, with real-part depths of approximately -80 MeV for medium to heavy nuclei, and Level-shifts (a) and widths (b) of the K^- atom with the best-fit density dependent optical potentials [53] as shown in Fig. 1.5. Similar shallow potentials are also suggested by motivated Chiral SU(3) approaches fitting low-energy K^-p reaction data [54]. Furthermore, imposing self-consistency in the construction of the optical potential tends to result in even shallower potentials of around -60 MeV [55, 56].

Significant refinements to the $t\rho$ model (Eq. 1.6) were introduced by implementing a density-dependent (DD) potential. This modification replaces the fixed parameter b_0 with a density-dependent term: $b_0 \rightarrow b_0 + B_0[\rho(r)/\rho_0]$. The parameters b_0, B_0, and $\alpha \geq 0$ are determined through fitting procedures. Global fits incorporating 65 data points regarding level shifts and widths for kaonic atoms ranging from ^{7}Li to ^{238}U demonstrated that these density-dependent optical potentials favor a "deep" potential solution, characterized by real-part depths between $-(150$–$200)$ MeV. This "deep" nature is consistent with results obtained from other methods, such as the multiplicative function approach and the model-independent Fourier-Bessel analysis [57, 58].

More recently, the $\bar{K}$-nuclear potential was investigated using Ikeda-Hyodo-Weise (IHW) NLO chiral K^-N subthreshold scattering amplitudes [10, 11]. In this study, a single-nucleon density-dependent potential $V^{(1)}_{K^-}(\rho)$ was generated based on the IHW amplitudes, supplemented by a phenomenological density-dependent interaction potential $V^{(2)}_{K^-}(\rho)$ to account for multi-nucleon dispersive and absorptive processes. Both $V^{(1)}_{K^-}(\rho)$ and $V^{(2)}_{K^-}(\rho)$ were coupled implicitly within a self-consistent cycle built into the kaonic atom fitting procedure. Ultimately, this IHW-based composite potential $(V^{(1)}_{K^-}(\rho) + V^{(2)}_{K^-}(\rho))$ produced a deeply attractive real potential, reaching a depth of -191 MeV at the center of a Ni [59].

1.4.2 Precision Measurements of X-ray from $\bar{K}$ Helium

The J-PARC E62 experiment was performed to investigate the strong-interaction effects in kaonic helium isotopes with unprecedented precision, aiming to resolve the long-standing ambiguity regarding the depth of the $\bar{K}$-nucleus potential. Conducted at the J-PARC K1.8BR beamline, the experiment employed a superconducting Transition-Edge Sensor (TES) microcalorimeter array to measure the $3d \rightarrow 2p$ X-ray transitions

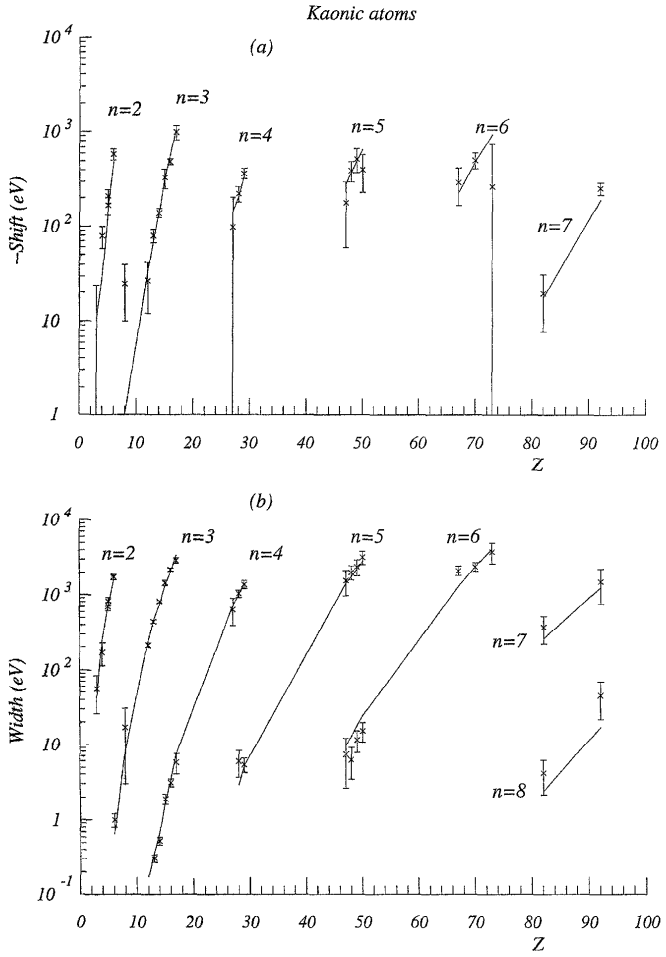

Figure 1.5: Level-shifts (a) and widths (b) of the K^- atom with the best-fit density dependent optical potentials taken from Ref. [53].

of kaonic ^{3}He and ^{4}He atoms [60]. A crucial technical achievement of this setup was the attainment of an energy resolution better than 6 eV (FWHM) at 6 keV, which represents a drastic improvement over the typical resolution of ~ 150 eV provided by silicon drift detectors in previous studies such as KEK-PS E570 and SIDDHARTA. Utilizing this superior resolution, the experiment successfully determined the strong-interaction shifts (ΔE_{2p}) and widths (Γ_{2p}) with a precision improved by approximately a factor of ten compared to past experiments. The measured values for kaonic ^{3}He were determined to be $\Delta E_{2p} = -0.2 \pm 0.4\,(\text{stat.}) \pm 0.3\,(\text{syst.})$ eV and $\Gamma_{2p} = 2.5 \pm 1.0\,(\text{stat.}) \pm 0.4\,(\text{syst.})$ eV. Similarly, the values for kaonic ^{4}He were measured as $\Delta E_{2p} = 0.2 \pm$

$0.3\,(\text{stat.}) \pm 0.2\,(\text{syst.})\,\text{eV}$ and $\Gamma_{2p} = 1.0 \pm 0.6\,(\text{stat.}) \pm 0.3\,(\text{syst.})\,\text{eV}$. These results have significant implications for theoretical models of the $\bar{K}$-nucleus interaction. Specifically, the data clearly exclude the large shifts ($|\Delta E| > 1\,\text{eV}$) and broad widths ($> 5\,\text{eV}$) predicted by certain coupled-channel calculations that assume deep potentials capable of accommodating p-wave bound states. Instead, the observed small shifts and widths are consistent with predictions based on standard optical potential models. Furthermore, this experiment provided the first direct determination of the finite width of a kaonic atomic state from the spectral line shape, marking a significant milestone in sub-eV precision spectroscopy of hadron-nuclear systems.

1.4.3 Implications of J-PARC E62 Data on $\bar{K}$-Nucleus Potential

Yamagata-Sekihara *et al.* [61] has investigated phenomenologically the $\bar{K}$-nucleus optical potential, using the ultra-high-precision K^{-3}He and K^{-4}He data from the J-PARC E62 experiment [60] as inputs.

In this study, the $\bar{K}$-nucleus potential $U(r)$ is defined using a simple phenomenological model, assuming that it is proportional to the nuclear density $\rho(r)$:

$$V_{\text{opt}}(r) = (V_0 + iW_0)\frac{\rho(r)}{\rho_0}, \tag{1.7}$$

where (V_0, W_0) are the parameters indicating the strength of the real (depth) and imaginary (absorption) parts of the potential at the normal nuclear density ρ_0.

First, the study identifies pairs of parameters (V_0, W_0) that can simultaneously reproduce the precision data for both K^{-3}He and K^{-4}He. Two different candidate solutions were found as shown in Fig. 1.6. One is the set IS-A, $(V_0, W_0) = (-90, -120)$ MeV (a relatively shallow real part and strong absorption). The other is IS-B, $(V_0, W_0) = (-280, -70)$ MeV (a very deep real part and weak absorption).

A critical point of this paper is that it verifies in its Appendix how well these two candidates (IS-A and IS-B) can reproduce the past X-ray measurement data from a wide range of heavier nuclei (from Li to U). The results showed that IS-B (deep real part) could not reproduce the data for heavier nuclei at all ($\chi^2/\text{DoF} = 16.4$). In contrast, IS-A (shallow real part) was shown to reproduce the data across a very wide range of nuclei

remarkably well (χ^2/DoF = 1.5). From this result, it is concluded that the $\bar{K}$-nucleus potential parameter set most favored by this study is $(V_0, W_0) = (-90, -120)$ MeV.

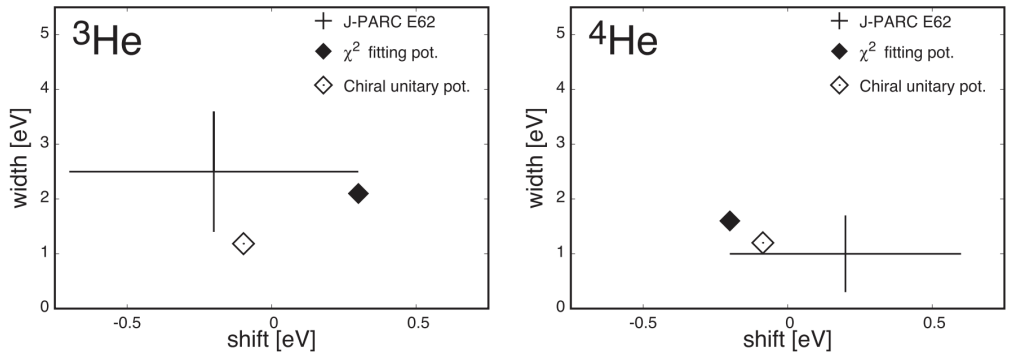

Figure 1.6: A comparison between theoretical calculations and recent experimental data for the kaonic atom 2p states in ^{3}He (left) and ^{4}He (right) from Ref. [61]. The plots show the energy shifts (derived from the 3d $\rightarrow$ 2p transition) versus the level widths. The experimental results from J-PARC E62 are indicated by the crosshairs. Theoretical predictions are shown for two models: the χ^2 fitting potential using all the data available including heavy atoms (solid diamond) and the chiral unitary potential (open diamond).

Furthermore, the analysis strongly suggests the possibility that the potential has a strong isospin dependence (a difference in the in-medium behavior of K^-p and K^-n), based on the slight differences between the K^{-3}He and K^{-4}He data. The paper also proposes that while IS-A and IS-B are difficult to distinguish in the $2p$ orbital, they produce a clear difference on the order of several keV in the $1s$ orbital.

1.4.4 Origin of Repulsive Energy Shift in Kaonic Atoms

A comprehensive investigation of kaonic-atom X-ray data has revealed that all measured systems exhibit a repulsive energy shift—an upward displacement of the atomic levels compared with the pure electromagnetic values. This phenomenon of the repulsive shifts is puzzling at first sight, because the fundamental $\bar{K}N$ interaction is known to be strongly attractive, the $\Lambda(1405)$ as a quasi-bound state, as already discussed in the previous section. This behavior is now understood to be a consequence of the existence of the $\bar{K}N$ bound state as the $\Lambda(1405)$ resonance lying below the $\bar{K}N$ threshold.

Iizawa, Jido *et al.* [62] explored two possible mechanisms that could reconcile the attractive $\bar{K}N$ interaction with the observed repulsive atomic shifts.

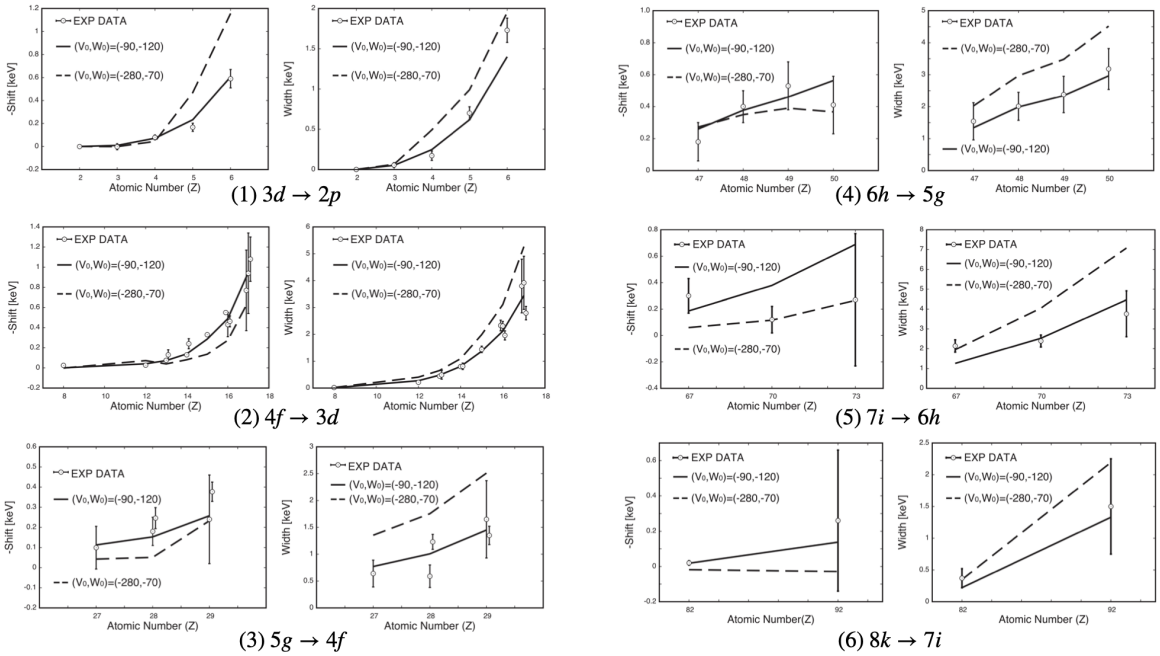

Figure 1.7: Systematic comparison of the energy shifts (left panel in each pair) and level widths (right panel in each pair) for various kaonic atom states, plotted against the atomic number Z. The experimental data (EXP DATA, circles with error bars) are shown for the transitions indicated: (1) $3d \rightarrow 2p$, (2) $4f \rightarrow 3d$, (3) $5g \rightarrow 4f$, (4) $6h \rightarrow 5g$, (5) $7i \rightarrow 6h$, and (6) $8k \rightarrow 7i$. The theoretical calculations are shown for two sets of optical potential parameters, which are known to reproduce the ^{3}He and ^{4}He X-ray data well: (V_0, W_0) = (-90, -120) MeV (dashed lines) and (V_0, W_0) = (-280, -70) MeV (solid lines). These figures are taken from [61]

The first hypothesis involves *the rearrangement of the energy spectrum caused by a strongly attractive optical potential* (Zel'dovich effect). As the attractive depth increases, the original atomic $1s$ state is pulled down significantly, eventually becoming confined within the nuclear radius as a "nuclear state." Consequently, the original atomic $2s$ state descends to occupy the position of the lowest-lying atomic orbital. Since the energy of this state is higher than that of the unperturbed Coulombic $1s$ level, it manifests as an apparent repulsive shift relative to the pure Coulomb case.

The second hypothesis concerns *the effect of a large imaginary optical potential*. In this scenario, the imaginary part of the optical potential, usually associated with nuclear absorption (loss of flux) at first order in perturbation theory, can act as a repulsive contribution at second order:

$$E_n^{(2)} = \sum_{m \neq n} \frac{\langle \phi_n \mid i \operatorname{Im} V_{\text{opt}} \mid \phi_m \rangle^2}{E_n - E_m}.$$

This mechanism naturally leads to an upward energy shift of the atomic states even when the underlying interaction is attractive.

Iizawa and Jido find that while the first mechanism—level repulsion—can account for only a limited set of systems, the second mechanism involving the imaginary potential provides a comprehensive and consistent explanation of the full kaonic-atom data set. Thus, their analysis underscores once again the essential importance of determining the imaginary part of the antikaon optical potential with precision.

1.4.5 Kaonic Nucleus

Several experiments on stopped K^- reactions have been conducted using liquid helium targets and bubble chambers [63]. These studies revealed that Σ hyperon emission dominates over Λ emission in the final state. Additionally, for nuclei heavier than ^{12}C, the non-mesonic decay fraction (involving multi-nucleon absorption) was found to be approximately 20% as shown in Table 1.1.

Recent discussions regarding the distinction between "deep" and "shallow" $\bar{K}$-nucleus potentials have also utilized comparisons of calculated $1s_\Lambda$ hypernuclear formation rates in stopped K^- reactions against measured values from the FINUDA Collaboration [25]. While this comparison tends to support the "deep" potential hypothesis, the conclu-

Table 1.1: Branching ratios R (in %) for hyperon production using stopped K^-[64]. The ratio R_n/R_p is the ratio of captures on neutrons to captures on protons. The ratio R_m is the branching ratio for capture on multinucleon clusters in the nucleus with no emitted pions, reaching about 20% in nuclei beyond ^{12}C.

Ratio	H	D	He	C	Ne
$R(\Lambda\pi^0)$	4.9	5.0	6.2	4.4	3.4
$R(\Sigma^+\pi^-)$	14.9	30.0	37.3	37.7	37.7
$R(\Sigma^-\pi^+)$	34.9	22.0	10.9	16.8	20.4
$R(\Sigma^0\pi^0)$	21.4	23.0	21.2	25.7	27.6
$R(\Lambda\pi^-)$	9.7	10.0	12.6	8.7	6.7
$R(\Sigma^0\pi^-)$	7.1	5.0	5.9	3.3	2.1
$R(\Sigma^-\pi^0)$	7.1	5.0	5.9	3.3	2.1
R_n/R_p	0.31	0.25	0.32	0.18	0.12
R_m		0.01	0.16	0.19	0.23

sive determination of whether the interaction is "deep" or "shallow" remains an open question in the current landscape.

In contrast, in-flight K^- absorption reactions, where the incident kaon carries finite momentum, have not yet been systematically investigated. Kinematically, the momentum transfer in these reactions is significantly larger compared to pion-induced reactions, suggesting that multi-nucleon absorption processes are more likely to occur. However, the reaction mechanism is expected to be complicated due to the involvement of numerous open channels. Experimentally, it remains undetermined whether the non-mesonic decay fraction for in-flight kaons stays around the 20% observed in stopped reactions or increases further. In terms of elementary processes, single-nucleon absorption is dominated by s-wave interactions, with $K^-p \to \pi^-\Sigma^0$ being the primary channel, while two-nucleon absorption is represented by processes such as $K^-d \to \Lambda p$.

The KEK-PS E548 experiment measured energy spectra for both the $^{12}\mathrm{C}(K^-, n)$ and $^{12}\mathrm{C}(K^-, p)$ reactions [65]. Using the Green's function method, potential depths were estimated at $-190\,\mathrm{MeV}$ for the (K^-, n) reaction and $-160\,\mathrm{MeV}$ for the (K^-, p) reaction. However, the validity of this experimental setup has been challenged; a specific critique highlighted that the experimental requirement for detecting at least one charged particle in the decay counter, trigger bias, could introduce significant distortion to the spectrum shape. Consequently, a distortion-free, high-resolution inclusive spectrum was required to settle the discussion on the potential depth.

The next chapter reviews the J-PARC E05 in-flight experiment, which marked a significant advance by determining the real part of the optical potential for kaonic nuclei. However, the imaginary part of this potential remained unconstrained by the experiment. To address this crucial gap, a new experiment was conducted, introducing a novel observable to precisely measure this imaginary component. The methodology and results of this new approach form the central focus of this dissertation.

Chapter 2

Motivation and Objectives

As established in the previous chapter, the determination of the imaginary part of the kaon-nucleus optical potential is an unresolved issue in hadronic physics. While the preceding J-PARC E05 experiment successfully constrained the real part of the potential, the imaginary component remained elusive. The primary objective of the research presented in this dissertation is, therefore, to provide the first experimental determination of this imaginary part. This chapter outlines the novel experimental strategy developed to achieve this goal, detailing the unique observable introduced for this measurement.

2.0.1 Insights from $^{12}\mathrm{C}(K^-, p)$ inclusive measurement

As mentioned in Chap. 1, the J-PARC E05 experiment provides the immediate context for this research. In that experiment, a trigger-bias-free spectrum was successfully obtained from the $^{12}\mathrm{C}(K^-,\, p)$ inclusive measurement at the J-PARC K1.8 beam line [66]. The obtained spectrum was compared with theoretical calculations based on the Green function method to evaluate the $\bar{K}$–nucleus optical potential. The measured spectrum, shown in Fig. 2.1 (a), is understood as a superposition of various reaction channels. The specific reaction channels contributing to the forward high-momentum proton events are summarized in Table 2.1, classified by the proton source (direct reaction or hyperon decay). Furthermore, the possible quasi-free inelastic processes on individual nucleons (p or n) within the $^{12}\mathrm{C}$ nucleus are detailed in Table 2.2. The comparison yielded the potential parameters $(V_0, W_0) = (-80,\, -40)\,\mathrm{MeV}$, which reproduce the experimental data most consistently, as shown in Fig. 2.1 (a). The real part corresponds to the "shallow

potential" predicted by the chiral unitary models, indicating a moderately attractive $\bar{K}$–nucleon interaction in nuclear matter. On the other hand, the χ^2 distribution shows that the sensitivity to the imaginary part is rather low, and therefore the absorptive strength cannot yet be determined with sufficient accuracy, as shown in Fig. 2.1 (b).

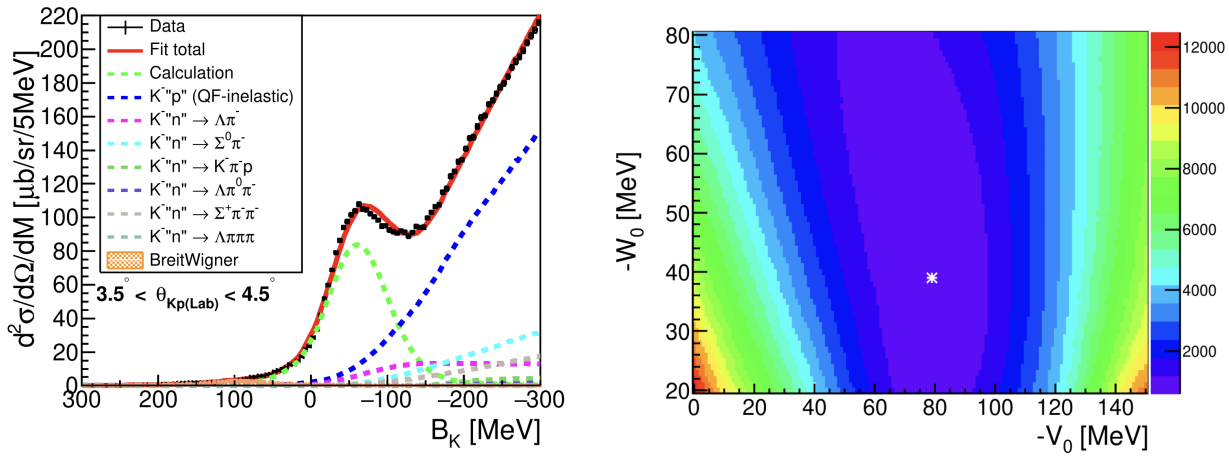

(a) (b)

Figure 2.1: (a) Measured spectrum with the fitted curve (red line), which is the sum of the calculated spectra from possible reactions (dotted lines) for the optical potential with the parameter set of $(V_0, W_0) = (-80, -40)$ MeV. (b) Two dimensional χ^2 plots as functions of the V_0 and W_0 parameters. The white asterisk shows the parameter set giving the minimum χ^2. Taken from Ref. [66].

Furthermore, a statistically significant excess of events was observed around the deeply bound region of $B_K \sim 100$ MeV as shown in Fig. 2.2. This event excess cannot be reproduced well by any parameter sets of optical potential. By assuming a Breit-Wigner function with $(-B_k, \Gamma) = (-90, 100)$ MeV added to the spectrum fitting for the potential parameter sets, the measured spectrum is found to be reproduced well. In this region, the dominant one-nucleon mesonic process $K^- N \to \pi Y$ is kinematically closed, and non-mesonic channels such as $K^- NN \to YN$ are expected to become dominant. One interpretation of the observed excess is a deeply bound Y^*–nucleus system ($Y^* = \Lambda(1405)$ or $\Sigma(1385)$). However, no firm conclusion can be drawn from the present data alone, and further experimental studies with coincident detection are necessary to clarify its origin.

These two outstanding issues—the poorly constrained absorptive potential and the unknown origin of the deeply bound event excess—are the primary motivations for the recently performed J-PARC E42 experiment, the central subject of this dissertation.

Table 2.1: List of K^-p reaction channels identified in the forward high-momentum proton analysis. The reactions are classified into Elastic and Quasi-Free Inelastic (QF-Inelastic) types. Protons originate either directly from the reaction or from the decay of hyperons.

Event Type	**Reaction Channel**	**Multiplicity**	**Proton Source**
Elastic	$K^-p \to K^-p$	2	Direct
QF-Inelastic	$K^-p \to \Lambda\pi^0$	2	Decay ($\Lambda \to p\pi^-$)
	$K^-p \to \Sigma^+\pi^-$	2	Decay ($\Sigma^+ \to p\pi^0$)
	$K^-p \to \bar{K}\pi p$	3	Direct
	$K^-p \to \Lambda\pi^+\pi^-$	3	Decay ($\Lambda \to p\pi^-$)
	$K^-p \to \Sigma\pi\pi$	3	Decay ($\Sigma \to p\pi$)
	$K^-p \to \bar{K}\pi\pi p$	4	Direct
	$K^-p \to Y\pi\pi\pi$	4	Decay ($Y \to p\ldots$)

Table 2.2: List of possible quasi-free inelastic reactions on a single nucleon in the $^{12}\mathrm{C}(K^-, p)$ reaction. "p" and "n" denote a proton and a neutron with Fermi motion in the nucleus, respectively.

Target Nucleon	**Reaction Channel**	**Proton Source**
Proton ("p")	K^-"p" (QF-Inelastic)	Direct / Decay
Neutron ("n")	K^-"n" $\to \Lambda\pi^-$	Decay ($\Lambda \to p\pi^-$)
	K^-"n" $\to \Sigma^0\pi^-$	Decay ($\Sigma^0 \to \Lambda\gamma \to p\pi^-\gamma$)
	K^-"n" $\to K^-\pi^-p$	Direct
	K^-"n" $\to \Lambda\pi^0\pi^-$	Decay ($\Lambda \to p\pi^-$)
	K^-"n" $\to \Sigma^+\pi^-\pi^-$	Decay ($\Sigma^+ \to p\pi^0$)
	K^-"n" $\to \Lambda\pi\pi\pi$	Decay ($\Lambda \to p\pi^-$)

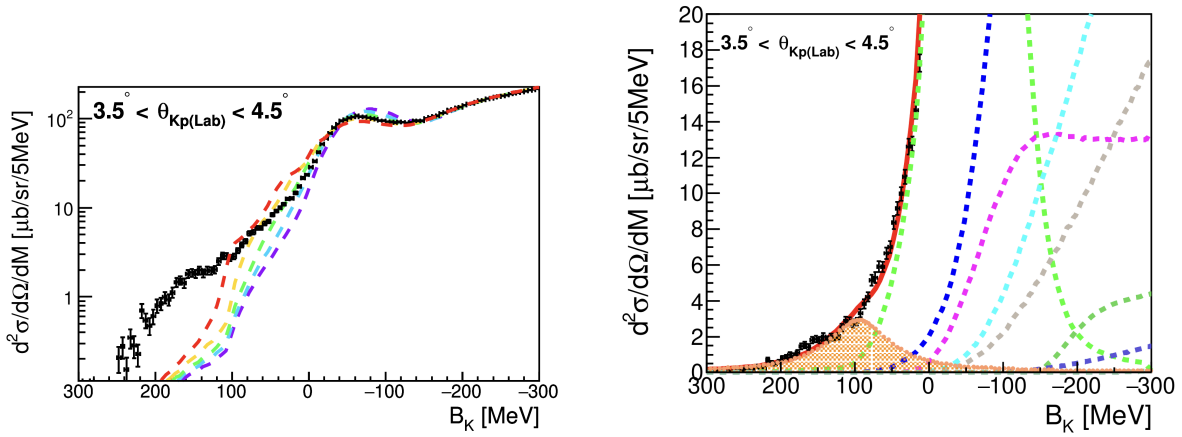

(a) (b)

Figure 2.2: (a) Measured spectrum with the fitted curve (red line), which is the sum of the calculated spectra from possible reactions (dotted lines) for the optical potential with the parameter set of $(V_0, W_0) = (-80, -40)$ MeV. (b) Measured spectrum with the fitted curve (red line), which is the sum of the calculated spectra from possible reactions (dotted lines) for the optical potential with the parameter set of $(V_0, W_0) = (-80, -40)$ MeV, and, Breit-Wigner function with $(-B_K, \Gamma) = (-90, 100)$ MeV. This figure shows a magnified view of the vertical axis in Fig. 2.1 (a). Taken from Ref. [66].

2.1 Imaginary Part of Optical Potential

2.1.1 Current Status and Remaining Open Questions

The depths of the $\bar{K}$-nucleus optical potential remain a subject of active discussion, generally categorized into "deep" and "shallow" solutions. Table 2.3 summarizes the typical values of the real and imaginary parts at the nuclear saturation density (ρ_0).

Theoretical approaches based on chiral SU(3) dynamics, such as the standard $t\rho$ approximation, typically predict a shallow potential. In these models, the real part depth is moderate (~ -40 to -80 MeV), and the imaginary part is also relatively shallow (~ -40 to -60 MeV), reflecting the microscopic $\bar{K}N$ interaction and the $\Lambda(1405)$ structure [67, 68]. The fundamental energy scale of this interaction is illustrated in Fig. 2.3, which shows the energy levels of the K^-p system and its coupled channels relative to the threshold. As listed in Table 2.4, the $\Lambda(1405)$ resonance explicitly couples to the $\Sigma\pi$ channels, located approximately 100 MeV below the $\overline{K}N$ threshold. This proximity of the resonance to the threshold is a key feature of the chiral dynamics.

In contrast, phenomenological analyses involving global fits to kaonic atom X-ray

Table 2.3: Typical depths of the $\bar{K}$-nucleus optical potential at nuclear saturation density (ρ_0). The values distinguish between the "shallow" potentials derived from chiral microscopic models (Theo.) [67, 68] and the "deep" potentials obtained from phenomenological global fits (Phen.) [53, 59] to kaonic atom data.

Potential Type	Approach	Real Part ($\mathrm{Re}\,V$)	Imaginary Part ($\mathrm{Im}\,V$)
Shallow	Theo. / Chiral SU(3)	~ -40 to $-80\,\mathrm{MeV}$	~ -40 to $-60\,\mathrm{MeV}$
Deep	Phen. / DD-fit	~ -150 to $-200\,\mathrm{MeV}$	~ -90 to $-110\,\mathrm{MeV}$

Table 2.4: Threshold energies and isospin states for K^-p scattering channels of $K^-p \to Y\pi$. The threshold energy ΔM is defined relative to the K^-p mass threshold.

Type	**Process**	**ΔM (MeV)**	**Isospin (I)**
Elastic	$K^-p \to K^-p$	–	0, 1
Charge Exchange	$K^-p \to \bar{K}^0n$	+5.3	0, 1
Inelastic ($\Sigma\pi$)	$K^-p \to \Sigma^+\pi^-$	−104.2	0, 1
	$K^-p \to \Sigma^-\pi^+$	−96.2	0, 1
	$K^-p \to \Sigma^0\pi^0$	−100.2	0
Inelastic ($\Lambda\pi$)	$K^-p \to \Lambda\pi^0$	−178.6	1

data favor a deep potential. These density-dependent (DD) models require a strongly attractive real part (~ -150 to $-200\,\mathrm{MeV}$) combined with a highly absorptive imaginary component ($\sim -100\,\mathrm{MeV}$) to reproduce the observed level shifts and widths simultaneously. The deep imaginary part is often attributed to multi-nucleon absorption processes occurring in the dense nuclear medium [53, 59].

The determination of the imaginary part of the optical potential, W_0, is of great importance for a comprehensive understanding of the $\overline{K}$-nucleus interaction. While earlier studies often focused on the depth of the real part (V_0) to search for deeply bound kaonic nuclear states, it has become increasingly clear that the imaginary part plays a decisive role in the in-medium dynamics. The significance of understanding the imaginary potential is threefold.

First, the imaginary part encodes the microscopic absorption mechanisms of the antikaon in the nuclear medium. Global analyses of kaonic atom data have established that the absorption width is exceptionally large, ranging from 50 to 100 MeV [53, 59]. This large width suggests significant contributions from multi-nucleon processes, such as $\overline{K}NN \to YN$. This conclusion is further supported by the recent systematic

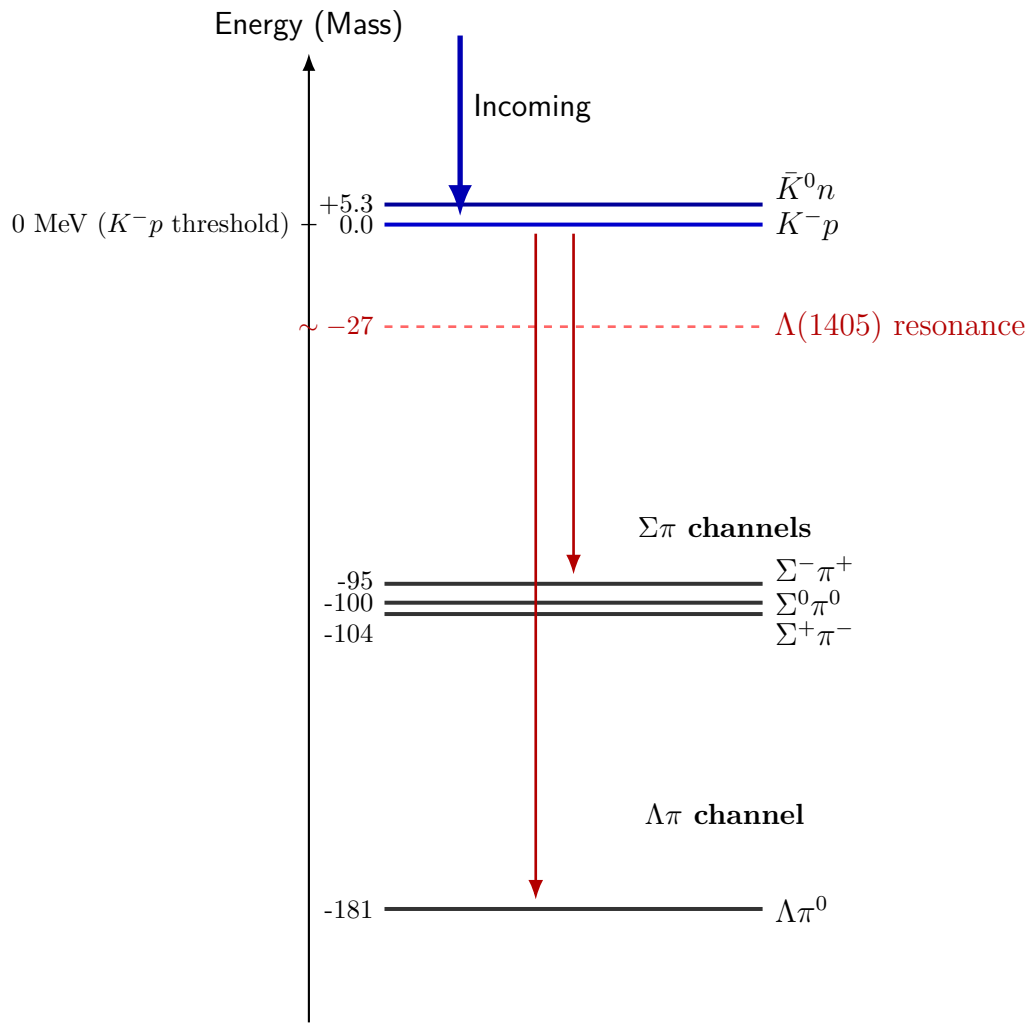

Figure 2.3: Energy level diagram of the K^-p system and coupled channels relative to the K^-p threshold.

analysis of kaonic atoms by Yamagata-Sekihara et al. [61] as described in Sec. 1.4.3 in detail. Their comprehensive calculation, which covers a wide range of nuclear targets, strongly indicates that a potential with a large imaginary part is required to consistently reproduce the global data. These findings reinforce the view that strong multi-nucleon absorption is a dominant feature of the interaction.

Furthermore, the real and imaginary parts of the optical potential are not independent parameters but are intrinsically coupled. This interdependence manifests in both phenomenological and theoretical aspects.

Phenomenologically, global analyses of kaonic atoms have revealed a "continuous ambiguity" in the potential parameters. Because the atomic data primarily constrain the potential at the nuclear surface, a wide range of potential depths (real parts) can reproduce the experimental results equally well, provided that the absorption strength

(imaginary part) is adjusted accordingly [53, 59]. This implies that the depth of the real potential—whether deep or shallow—cannot be uniquely determined without a strict independent constraint on the imaginary part.

Theoretically, this coupling is even more fundamental. In microscopic approaches based on chiral dynamics, the real and imaginary parts of the in-medium self-energy are connected through dispersion relations [69, 70]. The energy dependence of the absorption (imaginary part) directly dictates the attractive strength (real part) near the threshold. Consequently, the determination of the imaginary part is physically a prerequisite for establishing the correct structure of the real potential.

Second, the magnitude of the imaginary part fundamentally alters the spectral nature of the antikaon in dense matter. Theoretical calculations based on chiral unitary dynamics predict that the strong absorption leads to a substantial broadening of the spectral function [56]. If the imaginary potential is sufficiently large, the quasiparticle peak of the antikaon may effectively dissolve. Thus, determining the absorptive strength is essential to conclude whether the antikaon retains a distinct particle identity or merges into the nuclear continuum.

Third, the imaginary part is key to resolving the long-standing puzzle of the repulsive energy shift in kaonic atoms. Although the elementary $\overline{K}N$ interaction is strongly attractive, experimental observations consistently show repulsive shifts in atomic levels. Recent theoretical studies suggest that this behavior is not merely due to level repulsion but is a consequence of the large imaginary potential acting as a repulsive contribution in the second-order perturbation [62]. This implies that the "repulsive" nature of the shift is, in fact, a manifestation of strong nuclear absorption.

Therefore, an accurate constraint on the imaginary part is not only necessary for disentangling the real part of the potential but is also central to understanding the many-body interaction and medium effects and the existence of kaonic nuclear states.

2.1.2 Probing the Imaginary Potential in the Nuclear Interior

The preceding sections have reviewed the present understanding of the $\bar{K}$–nucleus optical potential from both microscopic theory and experimental studies. Kaonic-atom measurements have established that the imaginary part of the potential must be sizable, reflecting strong multi-nucleon absorption in the nuclear medium. Microscopic chiral-

model calculations further support this picture, predicting that the antikaon develops a large in-medium width and a strongly distorted spectral function.

Recent phenomenological analyses of light kaonic atoms (J-PARC E62) have shown that the real part of the potential is likely to be relatively shallow, while the imaginary part remains less tightly constrained. At the same time, the in-flight $^{12}\mathrm{C}(K^-, p)$ measurement (J-PARC E05), discussed in Sec. 2.0.1, has provided complementary information for a medium-mass nucleus. Although E05 yielded a consistent estimate for the real part of the potential, its sensitivity to the imaginary part was limited, and the absorptive strength could not be determined with satisfactory accuracy.

Taken together, these studies indicate that the magnitude and density dependence of the imaginary part—as well as its possible energy dependence below threshold—are still not well understood. Moreover, kaonic atoms probe the $\bar{K}$ primarily at extremely low energies and at the nuclear surface. To fully reveal the in-medium dynamics of the antikaon, including absorption processes deep inside the nucleus, it is essential to explore systems in which the K^- penetrates the nuclear interior with nonzero momentum.

In this respect, kaonic nuclear reactions offer information that is not accessible from kaonic atoms alone. They provide sensitivity to the sub-threshold energy region of the $\bar{K}N$ interaction, as well as to the density dependence of absorption mechanisms through multi-nucleon channels. Thus, measurements using K^- reactions on nuclear targets can supply crucial complementary constraints on the optical potential.

2.1.3 Approach to Imaginary Potential in J-PARC E42

Motivated by these open questions, the J-PARC E42 experiment aims to determine the imaginary part of the $\bar{K}$–nucleus potential with significantly improved precision by measuring the K^- escape process in exclusive kinematics. The conceptual design, experimental setup, and analysis framework of the E42 experiment will be described in the following chapter.

2.2 Objectives of the Present Study

The discussions in this chapter have clarified the current status of the $\bar{K}$–nucleus optical potential; while the real part has been increasingly constrained by the recent

kaonic-atom measurements and by the in-flight study of the J-PARC E05 experiment, the imaginary part, $\mathrm{Im}\, V_{\mathrm{opt}}$, remains undetermined and yet the most decisive quantity in the study of the $\bar{K}$-nucleus interaction. It governs the in-medium absorption of antikaons and reflects the underlying sub-threshold processes, including quasi-free scattering and multinucleon absorption such as $K^- NN \to YN$. A precise determination of $\mathrm{Im}\, V_{\mathrm{opt}}$ is therefore indispensable for establishing a quantitative and unified description of antikaon propagation in nuclear matter.

However, as reviewed in Chapter 1, inclusive spectra such as those obtained by E05 provide only limited sensitivity to the absorptive strength. To overcome this limitation, a new observable with direct and robust sensitivity to the imaginary potential is required. In the J-PARC E42 experiment, we introduced such an observable: the escape process of the antikaon which is the quasi-free elastic scattering (QFES) in which the scattered K^- emerges from the nucleus without being absorbed, which is expected to be sensitive to the absorption strength, i.e., the imaginary part of the optical potential. A larger $|W_0|$ naturally leads to a smaller survival probability, and vice versa. In this sense, the escape process offers a straightforward and experimentally clean probe of the imaginary part. In the E42 experiment, Hyperon Time Projection Chamber (HypTPC) installed for various exclusive measurements enables access to the escape K^-.

The primary objective of this thesis is to perform a comprehensive analysis of the E42 data to obtain the *first experimental determination of the antikaon escape probability* from a nucleus. Through this measurement, the work aims to establish a new constraint on the imaginary part of the $\bar{K}$–nucleus optical potential, thereby addressing one of the most critical issues in the physics of antikaon-nucleus interactions.

2.3 Thesis Outline

This thesis is organized as follows:

- **Chapter 1** provides the scientific background for this study. It reviews the physics of $\bar{K}N$ and $\bar{K}A$ interactions and discusses the theoretical importance and experimental challenges related to the kaon-nucleus optical potential.

- **Chapter 2** (this chapter) clarifies the specific objectives of this thesis. It reviews the preceding J-PARC E05 experiment to highlight unresolved questions and then

presents an overview of the new J-PARC E42 experiment, where that question is to be addressed.

- **Chapter 3** describes the experimental setup of the J-PARC E42 experiment.
- **Chapter 4** details the data analysis methods, specifically the event selection and the procedure for deriving the inclusive spectrum.
- **Chapter 5** details the procedure for extracting the escape cross section, a novel observable introduced in this work.
- **Chapter 6** presents the theoretical formalism used to interpret the results and discusses their implications for the $\bar{K}$-nucleus optical potential, focusing on the analysis of the escape probability.
- **Chapter 7** summarizes the findings of this thesis and discusses future prospects.

Chapter 3

Experiment

3.1 Experimental Overview

The J-PARC E42 experiment, conducted from May to June 2021, was designed to search for H-dibaryon via the (K^-, K^+) reaction on a carbon target. The experiment was carried out at the Hadron Experimental Facility of J-PARC (Japan Proton Accelerator Research Complex), utilizing the high-intensity separated K^- beam delivered from the K1.8 beamline. The typical beam intensity was 5.5×10^5 particles per spill with a central momentum of 1.8 GeV/c. Each extraction period lasted 5.2 s (= 1 spill), and the beam cycle time was 2.1 s. In parallel with this double-strangeness program, the same experimental setup also enabled the measurement of the (K^-, p) reaction, which serves as a probe for kaonic nuclear systems. The investigation of such systems constitutes the primary objective of the present dissertation.

The $^{12}\mathrm{C}(K^-, p)$ reaction was induced on a diamond target located at the entrance of the Hyperon Spectrometer. Scintillation counters and Cherenkov detectors placed along the K1.8 beamline and downstream of the KURAMA spectrometer were used to generate triggers.

The momentum of the incident K^- beam was determined using the K1.8 beamline spectrometer, while the momentum of the scattered p particles was reconstructed with the KURAMA spectrometer. Both spectrometers were equipped with timing counters and tracking chambers to measure particle trajectories and momenta with high precision.

The Superconducting Hyperon Spectrometer (SHS) was positioned between the two

spectrometers to detect charged decay products originating from hyperons produced in the target. The SHS system consisted of a large-acceptance dipole magnet, a Time Projection Chamber (TPC), and a downstream time-of-flight detector. All detector signals were digitized and recorded using a unified Data Acquisition (DAQ) system. An overview of the entire experimental setup is shown in Fig. 3.1. The detailed configurations and operational principles of each subsystem are described in the following sections.

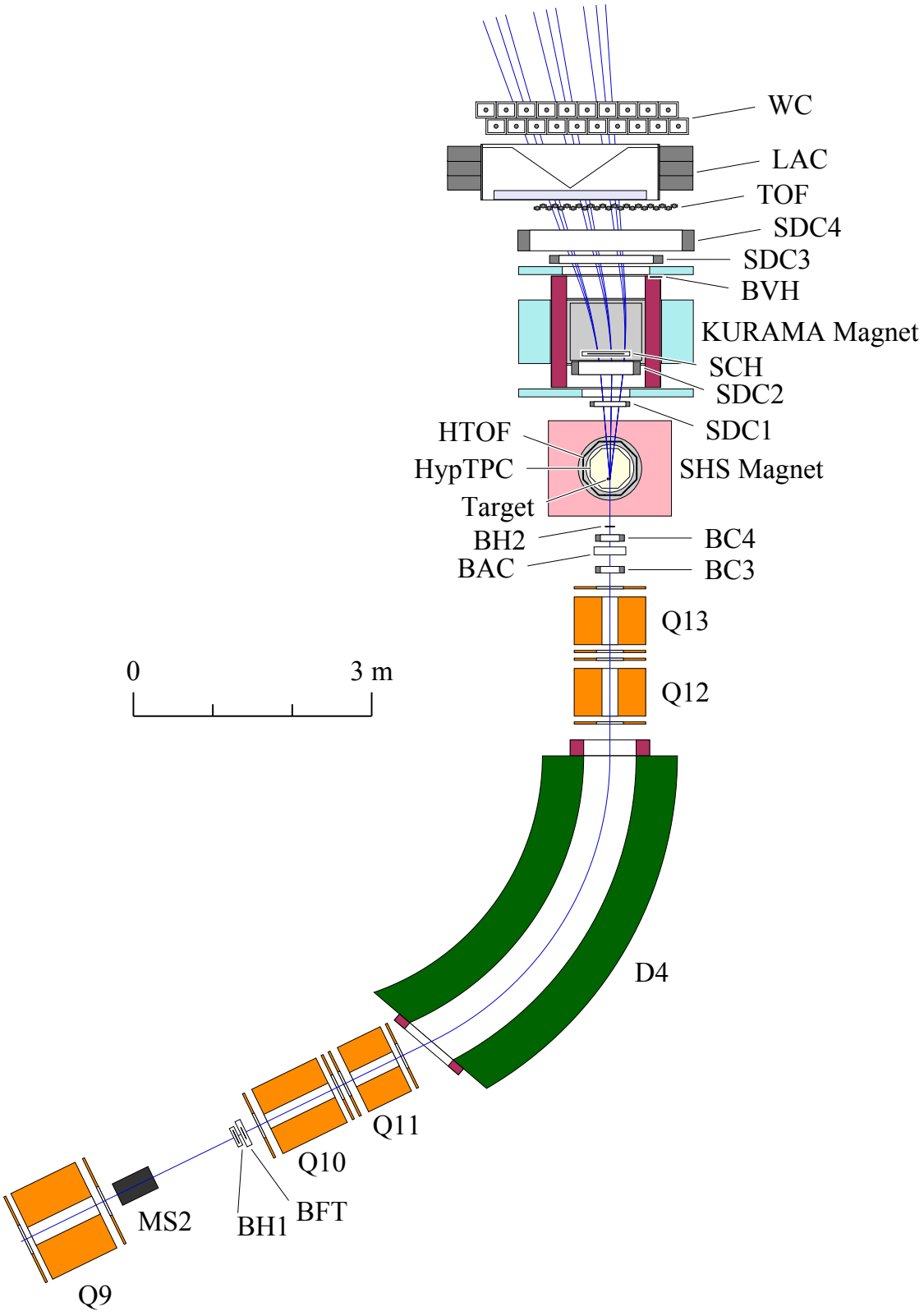

Figure 3.1: An overview of the E42 experimental configuration. The incoming K^- beam is measured by the K1.8 beamline spectrometer, while the KURAMA and SHS spectrometers identify the outgoing K^+ particles and hyperon decay products, respectively.

3.2 J-PARC K1.8 Beamline

J-PARC is a suite of proton accelerators and experimental facilities that enables cutting-edge research across a broad spectrum of disciplines, including elementary-particle and nuclear physics, materials science, life sciences, and nuclear transmutation. Protons are accelerated sequentially to 400 MeV by a linear accelerator (linac), to 3 GeV by the Rapid-Cycling Synchrotron (RCS), and ultimately to 30 GeV by the Main-Ring (MR) synchrotron.

At the Hadron Experimental Facility, both the primary protons extracted from the Main-Ring synchrotron (MR) and the secondary particles produced when those protons impinge on a gold target (T1) are utilized. The primary beam is delivered in a slow-spill mode lasting roughly 2 sec, so that secondary particles are generated continuously at T1 and a high-intensity beam is supplied to the experimental areas. The primary and secondary beams are subsequently transported to beam lines such as K1.8, K1.8BR, KL, and the high-p line. To date, a wide variety of experiments—ranging from elementary-particle to hadron and nuclear physics—have been performed at the facility.

We conducted the E42 experiment in the K1.8 area, where a high-momentum, high-intensity kaon beam is available. The K1.8 beam line is equipped with two electrostatic separators, ESS1 and ESS2, which discriminate particles by velocity using a strong electric field crossed with a magnetic field. These devices provide a high-purity K^- beam with a momentum of 1.8 GeV/c, where the Ξ-hyperon production cross section reaches its maximum. This helps us produce kaonic nuclei and their deeply bound states.

The K1.8 beam line spectrometer is composed of three main sections: a front-end section, a mass-separation section, and a momentum-analysis section. A schematic layout of the beam line is illustrated in Fig. 3.2. This beam line was designed to deliver a high-intensity separated K^- beam with a central momentum of 1.8 GeV/c to the experimental target.

Front-end Section

The front-end section extends from D1 to IFV in Fig. 3.2. It consists of two dipole magnets (D1 and D2) and two quadrupole magnets (Q1 and Q2). The beam extraction

angle is set to 6°, which corresponds to the optimal condition for maximizing the kaon production cross section. Some beamline components in this region are housed inside a large vacuum tank maintained at approximately 1 Pa. The transported beam is vertically focused at the intermediate focus (IF) point. Horizontal and vertical beam profiles are defined by a horizontal slit (IFH) and a vertical slit (IFV), respectively. These slits are used to eliminate so-called cloud pions produced by K^0 decays and by secondary scattering from upstream materials.

Mass-Separation Section

The mass-separation section consists of two stages. The first stage extends from Q3 to MS1, and the second stage from Q7 to MS2, as shown in Fig. 3.2. This section includes one dipole magnet (D3), seven quadrupole magnets (Q3–Q9), four sextupole magnets (S1–S4), and three octupole magnets (O1–O3). Two electrostatic separators (ESS1 and ESS2), each equipped with four correction magnets (CM1–CM4), are installed to separate kaons from pions based on their mass differences. This double-stage electrostatic system plays a crucial role in achieving high-purity K^- beam delivery.

Each electrostatic separator generates a vertical electric field between parallel electrodes with a 10 cm gap and a plate length of 6 m. The field strength reaches up to 75 kV/cm when filled with He/Ne insulating gas at a pressure of about 10^{-2} Pa. In the experiment, both ESS1 and ESS2 were operated at an electric field of 50 kV/cm. Correction magnets (CM1–CM4) are located at the entrance and exit of each separator to compensate for the beam orbit distortions. After passing through the separators, the beam is vertically focused at the mass slits (MS1 and MS2). For pion-beam tuning, the correction magnet settings were adjusted so that only pions within the desired momentum bite could pass through the slits. A horizontal momentum slit (MOM) downstream of the system defines the overall momentum acceptance of the secondary beam.

Momentum-Analysis Section

The momentum-analysis section, also referred to as the K1.8 beam-line spectrometer, employs a $QQDQQQ$ magnetic configuration (Q10–Q13 and D4). In this region, the beam is focused onto the experimental target, and the momentum of each particle is determined from its trajectory.

During the present experiment, the central beam momentum was set to 1.8 GeV/c for the (K^-, p) reaction, with a typical momentum bite of about 3.4% (FWHM), as illustrated in Fig. 3.2. The horizontal and vertical beam sizes at the target position were approximately 16 mm and 11 mm (FWHM), respectively. A diamond target was employed, with dimensions of 50 mm (horizontal) × 30 mm (vertical). The beam incident angles at the target were 0.05 rad (horizontal) and 0.004 rad (vertical), respectively.

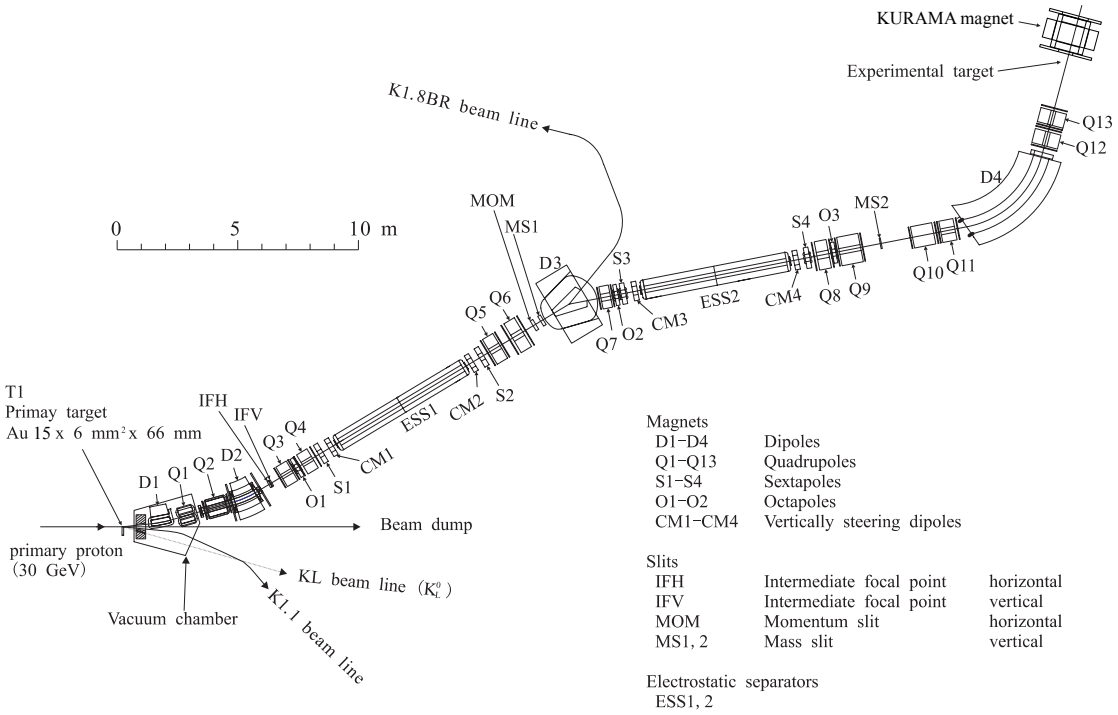

Figure 3.2: A diagram of the K1.8 beamline, designed to provide a high-purity K^- beam to the experimental area. The system uses a combination of magnetic and electrostatic elements to transport the secondary beam generated at the T1 target.

3.3 K1.8 Beamline Spectrometer

The downstream part of the K1.8 beam line functions as a beam spectrometer that determines the momentum and trajectory of each particle transported to the experimental area. A schematic layout of the K1.8 beam-line spectrometer is shown in Fig. 3.1. The spectrometer comprises two plastic scintillation hodoscopes (BH1 and BH2) for timing measurements, a Cherenkov counter (BAC) for particle identification, and three tracking detectors (BFT, BC3, and BC4) located upstream and downstream of the $QQDQQ$

magnet system.

The beam momentum is reconstructed from the horizontal position at the entrance and the trajectories measured at the exit, using a third-order transfer matrix formalism. The designed momentum resolution of the spectrometer is $\Delta p/p = 3.3 \times 10^{-4}$ (FWHM), with a corresponding position resolution of 200 μm (rms). The magnetic field of the dipole magnet (D4) was continuously monitored during operation using a high-precision Hall probe (Digital Teslameter 151, DTM-151) with an accuracy of 1.7×10^{-6}. The observed field fluctuation, $\Delta B/B$, was maintained below 10^{-4} throughout the experiment. The main design specifications of the K1.8 beam-line spectrometer are summarized in Table 3.1.

Table 3.1: Design specifications of K1.8 beam-line spectrometer.

Parameter	**Value**
Momentum resolution	3.3×10^{-4} (FWHM)
Maximum momentum	2.0 GeV/c
Maximum magnetic field	1.67 T
Bending angle	64°
Central orbital radius of D4	4 m
Pole gap of D4	19 cm
Flight path (BH1 $\rightarrow$ BH2)	10.33 m

3.3.1 Counters and Fiber Tracker

A series of timing and tracking detectors were installed along the K1.8 beam line to identify beam particles and measure their trajectories. This system consists of two plastic scintillation hodoscopes (BH1 and BH2), a beam aerogel Cherenkov counter (BAC), and a beam fiber tracker (BFT). They form the essential components of the beam monitoring and particle identification system.

BH1 and BH2 Plastic Scintillation Hodoscopes

The BH1 and BH2 counters form the beam time-of-flight (BTOF) system, which measures the flight time of particles between the two detectors for particle identification. The flight path length between BH1 and BH2 is approximately 10.4 m. At a beam momentum of 1.8 GeV/c, the corresponding time-of-flight difference between kaons and pions is about 1.1-1.3 ns.

BH1 Detector. The BH1 hodoscope, located upstream of the K1.8 spectrometer, is composed of eleven slats of 5 mm-thick BC-420 plastic scintillators. The slats are horizontally segmented to maintain a uniform beam rate, with three central slats 8 mm wide and outer slats gradually increasing up to 20 mm in width. The total active area is 170 mm (H) × 66 mm (V). Each scintillator bar is read out from both ends using 23.5 mm-diameter photomultiplier tubes (H6524MOD) coupled through acrylic light guides. Three-stage booster amplifiers (H1650MOD) are employed to enhance signal quality. To eliminate inactive gaps, adjacent slats are overlapped by 1 mm. The segmentation and dimensions of the BH1 detector are shown in Fig. 3.3.

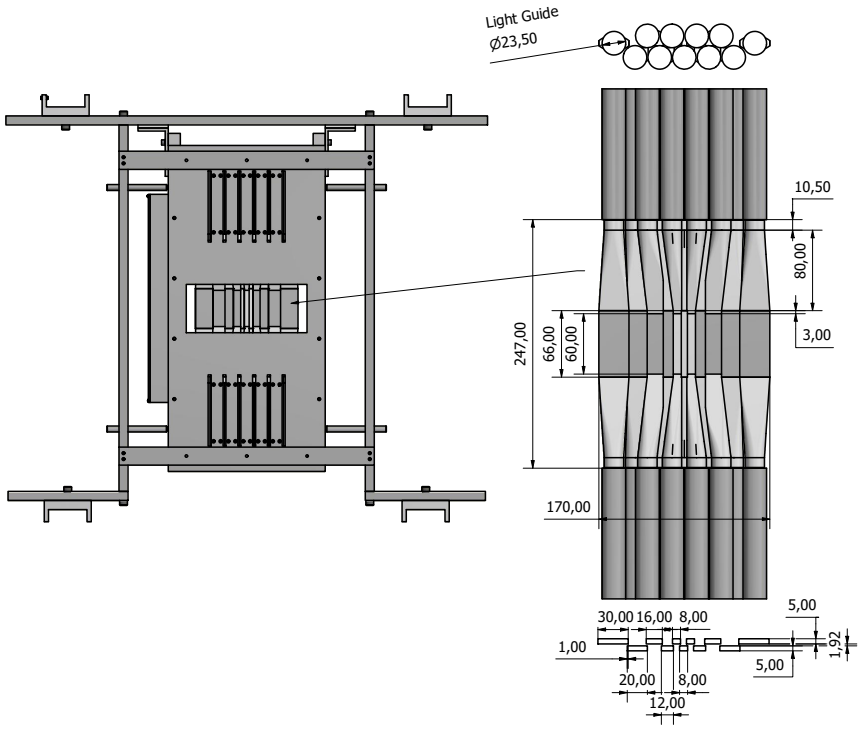

Figure 3.3: A diagram of the BH1 detector, showing its eleven horizontally-arranged scintillator bars of varying widths. This segmentation serves to equalize the beam rate per bar. The total effective area measures 170 mm (H) × 66 mm (V).

BH2 Detector. The BH2 counter is positioned between BC4 and the SHS spectrometer, serving as the common start-time reference for all E42 subsystems. It consists of eight segments of EJ-232 plastic scintillators, each 5 mm thick and 80 mm long, oriented perpendicular to the beam axis. The six central segments are 14 mm wide, while the two outer segments are 17 mm wide, providing a total effective area of 118 mm × 80 mm. Each segment is read out by three multi-pixel photon coun-

ters (MPPCs; S13360-3050PE) with an active area of 3×3 mm^2. To reduce optical crosstalk, the MPPC signals from each segment are individually amplified and summed on a dedicated readout board. The entire detector is enclosed with a light-tight dark sheet to ensure proper optical shielding. Position scanning calibration was performed to determine the beam-passing region accurately, as shown in Fig 3.4. The intrinsic time resolution of BH2 is 50 - 60 ps.

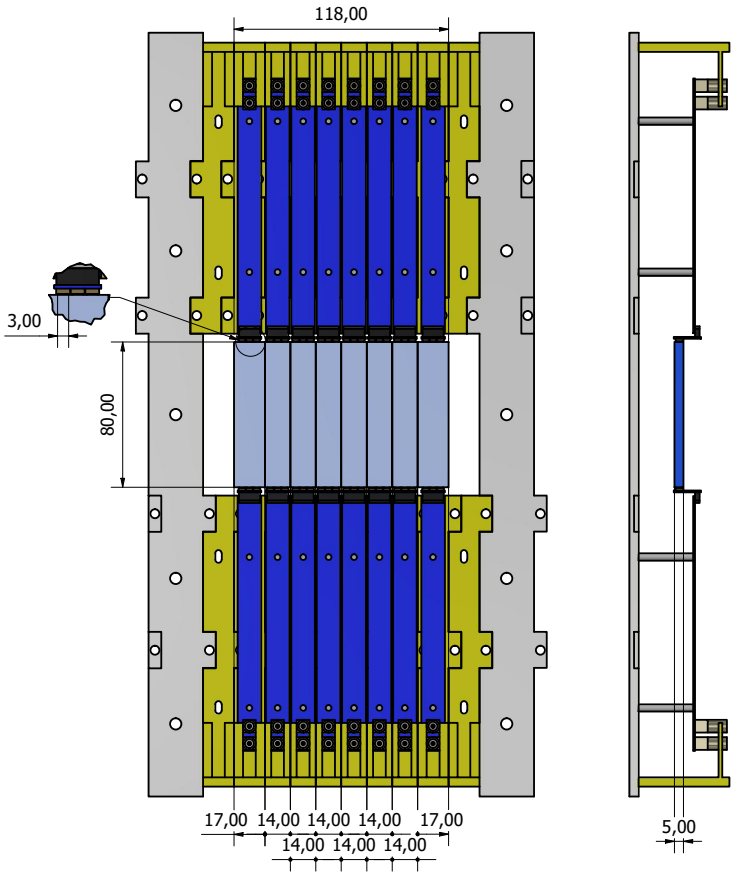

Figure 3.4: A diagram of the BH2 detector and its eight vertically arranged scintillator segments. The detector provides a total effective area of 118 mm $\times$ 80 mm, composed of six central 14-mm-wide bars and two 17-mm-wide outer bars.

BAC Aerogel Cherenkov Counter

The beam aerogel Cherenkov counter (BAC) is installed between the tracking chambers BC3 and BC4 to discriminate pions in the incident beam. It covers an active area of 342 mm $\times$ 80 mm, centered along the beam axis. The detector contains a 66 mm-thick silica aerogel radiator with a refractive index of $n = 1.03$, enclosed in a diffuse light box wrapped with Teflon sheets to enhance light reflection. The Cherenkov threshold

momenta for the aerogel are approximately 0.57 GeV/c for π^- and 2.0 GeV/c for K^-. Cherenkov photons are collected by five 2-inch fine-mesh photomultiplier tubes (PMTs; H6614-70UV) mounted beneath the radiator. Each PMT is equipped with a 19-stage grid-dynode structure and UV-transmitting glass, operated at high voltages between +2.3 kV and +2.4 kV. Analog signals from the five PMTs are summed using an analog mixer and sent to a discriminator to generate trigger decisions. The BAC operating threshold corresponds to a refractive index of $n = 1.03$.

BFT Beam Fiber Tracker

The beam fiber tracker (BFT) is positioned downstream of BH1 and measures the horizontal position and timing of the incident beam. It consists of 320 round scintillating fibers (Kuraray SCSF-78MJ) with a diameter of 1 mm, arranged in a two-layer XX' configuration. Each fiber is read out at one end by a multi-pixel photon counter (MPPC; Hamamatsu S10362-11-100P). The detector's active area is 160 mm (H) × 80 mm (V). The two fiber layers are staggered by a half-pitch to enhance spatial resolution. The BFT's timing and position resolutions are estimated to be 0.68 ns and 190 μm (σ), respectively, as summarized in Table 3.2. Photographs and schematic drawings of the detector are presented in Fig. 3.5.

Table 3.2: Specifications of the BFT in the K1.8 beamline spectrometer.

	Scintillation Fiber (Sensitive area) (W×H) [mm^2]	Readout Detector
BFT	Kuraray SCSF-78M, ϕ1 mm (160×80)	1×1 mm^2 MPPC (S10362-11-100P)

3.3.2 Drift Chambers

Two multi-wire drift chambers (MWDCs), designated as BC3 and BC4, were installed downstream of the K1.8 beam-line spectrometer to determine the position and trajectory of beam particles. Both chambers share an identical design and are mounted facing each other near the spectrometer exit. Each chamber comprises six detection layers arranged in the configuration $xx'uu'vv'$, where the u and v planes are tilted by ±15° relative to the vertical axis. The anode wire spacing is 3 mm, providing a high

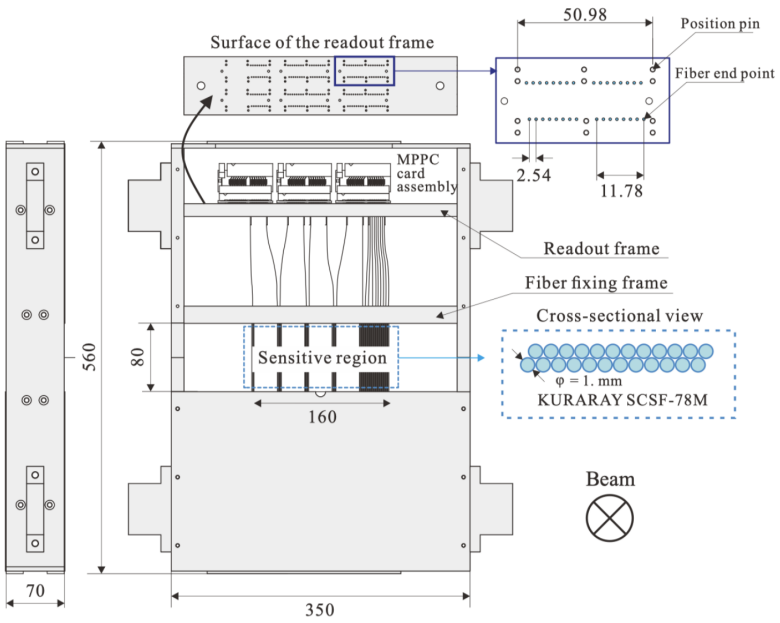

Figure 3.5: A schematic of the Beam Fiber Tracker (BFT). It is a hodoscope constructed from 320 round scintillating fibers (Kuraray SCSF-78MJ), each with a 1 mm diameter.

spatial resolution suitable for precise tracking. A schematic view of the internal wire structure is shown in Fig. 3.6.

Mechanical and Electrical Structure

Each pair of detection layers (e.g., xx', uu', vv') forms a doublet plane, with one layer offset by 1.5 mm (half a cell) relative to the other to eliminate left - right ambiguity in drift-time measurements for straight tracks. The sense wires are made of gold-plated tungsten with a diameter of 12.5 μm, while potential wires are fabricated from gold-plated beryllium copper (Au - BeCu) with a diameter of 75 μm. The cathode planes consist of 12 μm-thick aramid films coated with a 20 μm graphite layer and are stretched over rigid frames to ensure planarity. The spacing between the anode and cathode planes is 2 mm. Typical wire tensions are 20 g for anode wires and 80 g for potential wires, ensuring stable operation against electrostatic forces.

Gas System and Operation Conditions

The chambers are filled with a gas mixture of 76% argon, 20% iso-C_4H_{10}, and 4% methylal. Methylal is included as an additive to suppress polymerization by scavenging

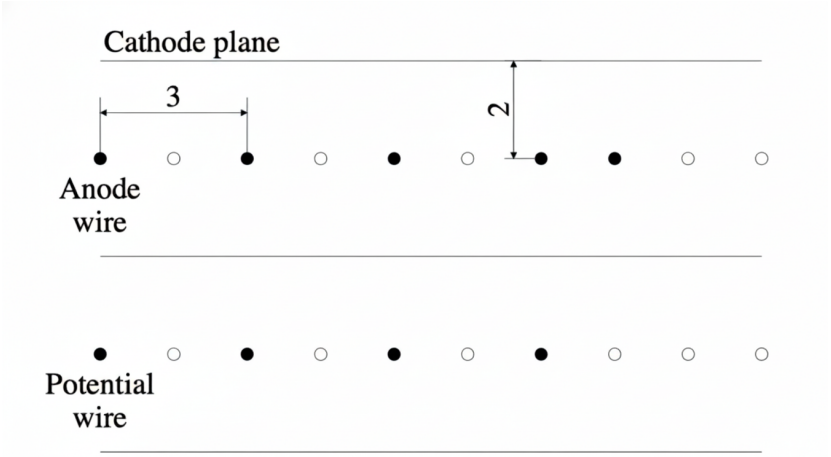

Figure 3.6: Schematic drawing of the BC3 and BC4 wire structure. The drift chambers consist of alternating anode and potential wires with a 4.5 mm spacing, and cathode planes positioned 3 mm away from the anode wires. The circles and cathode planes are enlarged by 1.5 times in this diagram

CH_2 radicals, thereby preventing the accumulation of polymer residues on the anode wires. This process mitigates wire damage due to beam-induced sputtering. The chamber pressure is maintained slightly above atmospheric pressure to avoid contamination from external air. Signals from the anode wires are processed by Amplifier - Shaper - Discriminator (ASD) chips mounted on dedicated readout cards. During normal operation, high voltages of approximately -1.20 kV and -1.22 kV are applied to the sense and potential wires, respectively.

Detector Specifications

The principal specifications of BC3 and BC4 are summarized in Table 3.3. Both detectors have an active area of 192 mm × 100 mm, with an anode spacing of 3 mm. The orientation of wire layers and tilt angles are optimized to provide high precision in both horizontal and vertical tracking components, supporting momentum reconstruction of the incident beam.

Table 3.3: Specifications of the BC3 and BC4 drift chambers.

Chamber	**Sensitive Area (W×H)** [$\mathbf{mm^2}$]	**Wire Spacing** [**mm**]	**Orientation**	**Tilt Angle** [°]
BC3	192 × 100	3	$xx'vv'uu'$	0, −15, +15
BC4	192 × 100	3	$uu'vv'xx'$	+15, −15, 0

3.4 KURAMA Spectrometer

The scattered protons from the (K^-, p) reaction were analyzed using the downstream KURAMA spectrometer. For the momentum analysis of outgoing protons, a large-acceptance dipole magnet, KURAMA, was employed together with a set of tracking and particle-identification detectors.

The KURAMA magnet is a normal-conducting H-type dipole magnet with a pole gap of 800 mm and dimensions of approximately 100 cm in width and 80 cm in length. It provides a magnetic field strength of about 0.7 T when operated at a current of 2400 A and a DC voltage of 170 V. The magnet power supply uses an input AC voltage of 380 V and an AC current of 800 A. A nuclear magnetic resonance (NMR) field meter (EFM-3000AX, ECHO Electronics Co., Ltd.) continuously monitors the magnetic field intensity at a reference position located 385 mm below the magnet center during excitation. The monitored field value is used to normalize the calculated magnetic field map for proton-tracking analysis.

The vertical magnetic field component $(-B_y)$ along the beam axis (z) determines the curvature of charged-particle trajectories through the spectrometer. The distribution of $-B_y$, together with the z-positions of adjacent detector components, is illustrated in Fig. 3.7.

The tracking system comprises four drift chambers (SDC1–4) placed downstream of the magnet to reconstruct the trajectories of scattered protons. Additional detectors were installed for triggering and particle identification: a scattered-charge hodoscope (SCH), a beam-veto hodoscope (BVH), a forward time-of-flight counter (TOF), a large aerogel Cherenkov detector (LAC), and a water Cherenkov detector (WC).

The SCH, BVH, and TOF detectors provide hit-pattern information from their scintillator segments, which is used in the matrix trigger logic. The TOF detector also provides time-of-flight measurements between BH2 and TOF, contributing to proton identification. The two Cherenkov counters, LAC and WC, are used to suppress background events by vetoing pions and kaons, respectively. The specifications of these detectors are summarized in Tables 3.7 and 3.5.

The designed momentum resolution of the KURAMA spectrometer is $\Delta p/p = 2.8 \times 10^{-2}$ (FWHM), and its geometrical acceptance is approximately 280 msr.

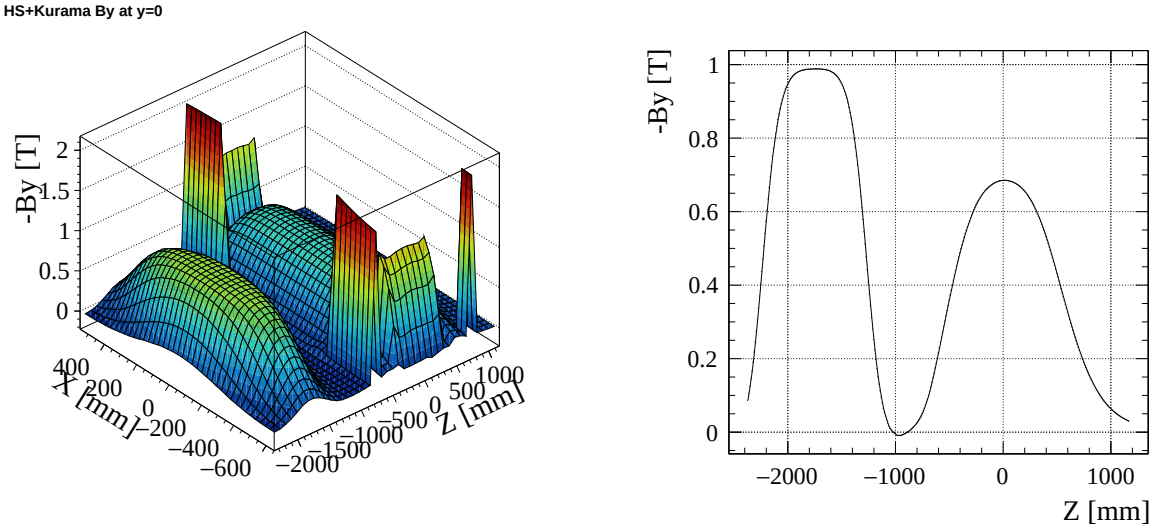

(a) (b)

Figure 3.7: Distribution of the magnetic field in the KURAMA spectrometer. (a) The three-dimensional profile of the B_y component, with the locations of the SHS and KURAMA magnets and the KURAMA end-guard indicated. (b) The on-axis distribution of the B_y component as a function of z (at $x = y = 0$).

Table 3.4: Specifications of the trigger and PID detectors in the KURAMA spectrometer.

	Scintillator/Radiator (Sensitive Area) (W×H×T) [mm^3]	Readout Detector
SCH	EJ-212 scintillator (673×450×2)	1×1 mm^2 MPPC (S10362-11-100P)
BVH	EJ-232 scintillator (184×100×5)	3×3 mm^2 MPPC (S13060-3050PE)
TOF	EJ-210 scintillator (1805×1800×30)	2″ PMT (H1949-51)
LAC	Silica aerogel, $n = 1.05$ (2080×1200×113)	5″ PMT (R1584-01, Burle 8854)
WC	Pure water, $n = 1.33$ (2698.5×1880×207)	2″ PMT (H11284-100UV)

Table 3.5: Specifications of the tracking drift chambers in the KURAMA spectrometer.

Drift Chamber	Sensitive Area (W×H) [mm^2]	Wire Spacing [mm]	Orientation	Tilt Angle [°]
SDC1	384×264	6	$uu'xx'vv'$	15, 0, −15
SDC2	700×400	10	$xx'yy'$	0, 90
SDC3	1152×1152	9	$xx'yy'$	0, 90
SDC4	1920×1280	20	$yy'xx'$	90, 0

3.4.1 Drift Chambers

Upstream Part

The drift chambers SDC1 and SDC2 were installed upstream of the KURAMA magnet to measure the incident trajectories of scattered protons. SDC1 has an effective area of 384 mm × 264 mm and consists of six wire planes with orientations uu', xx', and vv', tilted at 15°, 0°, and −15°, respectively. The anode-wire spacing is 6 mm, and the chamber is positioned at the upstream end of the KURAMA magnet.

SDC2 has an effective area of 700 mm × 400 mm and consists of four planes arranged in the $xx'yy'$ configuration, tilted at 0° and 90°. The wire spacing is 10 mm, and the chamber is installed at the entrance window of the KURAMA magnet. Both SDC1 and SDC2 operate with a gas mixture of Ar (76%), iso-C_4H_{10} (20%), and methylal (4%).

The internal wire configurations of SDC1 and SDC2 are illustrated in Fig. 3.8. Each chamber contains a periodic pattern of anode, potential, and shield wires. The wire spacing is 6 mm for SDC1 and 10 mm for SDC2.

Downstream Part

SDC3 and SDC4 are located downstream of the KURAMA magnet, where the trajectories of protons are measured after magnetic deflection. SDC3 has an effective area of 1152 mm × 1152 mm and consists of four planes in the $xx'yy'$ configuration with tilt angles of 0° and 90°. The anode-wire spacing is 9 mm.

SDC4 is the largest drift chamber in the spectrometer, with an effective area of 1920 mm × 1280 mm. It is composed of four planes arranged in the $yy'xx'$ configuration, tilted at 90° and 0°, respectively. The anode-wire spacing for SDC4 is 20 mm.

A gas mixture of Ar (50%) and C_2H_6 (50%) is used for both SDC3 and SDC4. The schematic wire configurations of these chambers are shown in Fig. 3.9. Each chamber includes two pairs of wire planes with anode, potential, and shield wires arranged in a repeated pattern. The wire pitch is 9 mm for SDC3 and 20 mm for SDC4.

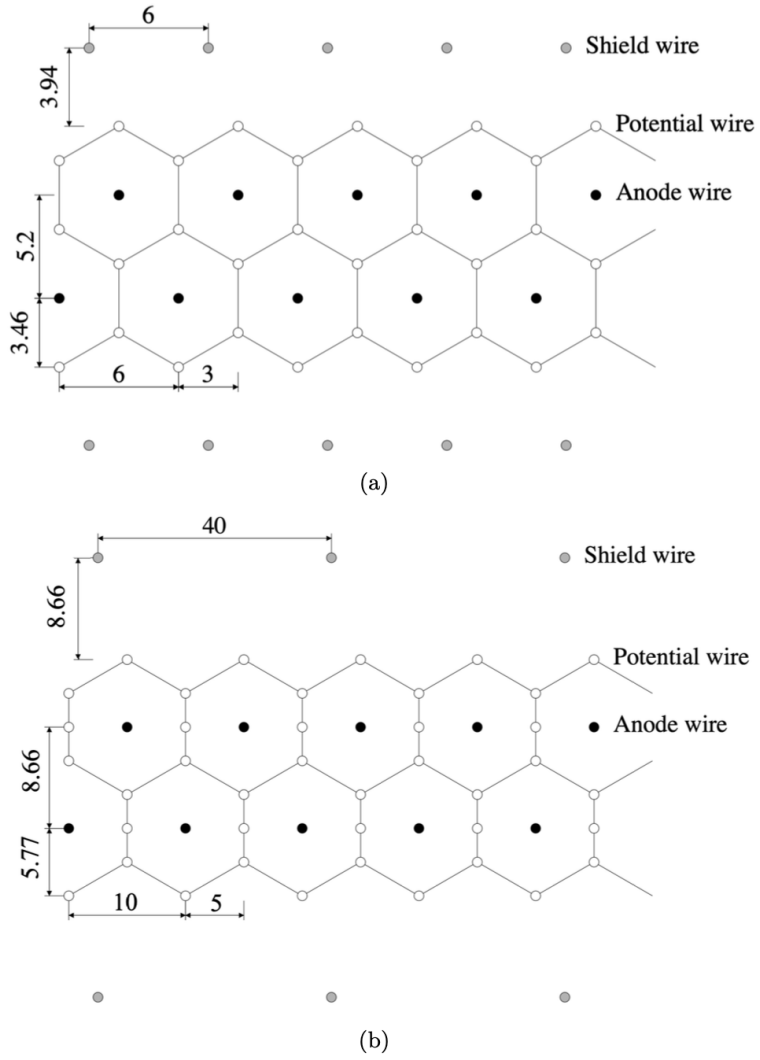

Figure 3.8: Schematic wire configurations of (a) SDC1 and (b) SDC2. Both chambers are composed of alternating anode, potential, and shield wires. The wire pitch is 6 mm in SDC1 and 10 mm in SDC2.

Table 3.6: Specifications of drift chambers in KURAMA spectrometer.

Drift Chamber	**Sensitive Area** (W×H) [mm^2]	**Wire Spacing** [mm]	**Orientation**	**Tilt Angle** [°]
SDC1	384×264	6	$uu'xx'vv'$	15, 0, −15
SDC2	700×400	10	$xx'yy'$	0, 90
SDC3	1152×1152	9	$xx'yy'$	0, 90
SDC4	1920×1280	20	$yy'xx'$	90, 0

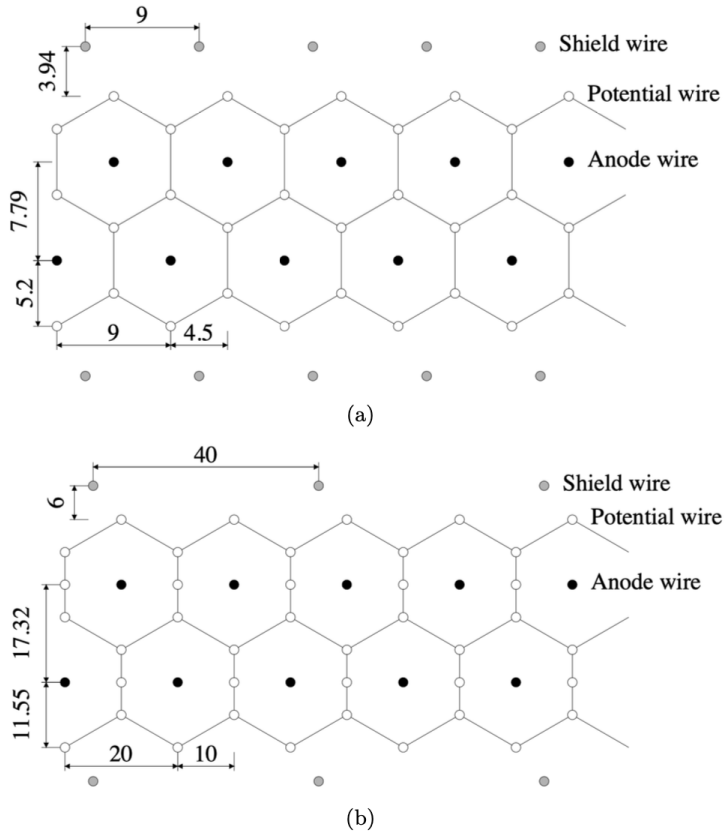

Figure 3.9: Schematic drawings of the wire configurations in SDC3 and SDC4. Each chamber consists of two pair planes with alternating anode, potential, and shield wires. The wire pitch is 9 mm in SDC3 and 20 mm in SDC4.

Table 3.7: Specifications of detectors for trigger and PID in KURAMA spectrometer.

	Scintillator/Radiator (Sensitive Area) (W×H×T) [mm^3]	**Readout Detector**
SCH	EJ-212 scintillator (673×450×2)	1×1 mm^2 MPPC (S10362-11-100P)
BVH	EJ-232 scintillator (184×100×5)	3×3 mm^2 MPPC (S13060-3050PE)
TOF	EJ-210 scintillator (1805×1800×30)	2″ PMT (H1949-51)
LAC	Silica aerogel, $n = 1.05$ (2080×1200×113)	5″ PMT (R1584-01, Burle 8854)
WC	Pure water, $n = 1.33$ (2698.5×1880×207)	2″ PMT (H11284-100UV)

3.4.2 Counters

SCH (Scattered Charge Hodoscope)

The scattered charge hodoscope (SCH) is positioned immediately upstream of the KURAMA spectrometer magnet. Its primary function is to record the hit pattern of charged particles scattered from the target region and to contribute to the online trigger selection in coordination with the TOF system. The SCH thus plays a key role in identifying (K^-, K^+) and (K^-, p) reaction events during data acquisition.

The detector consists of 64 plastic scintillator bars (EJ-212), each with dimensions of $2 \times 11.5 \times 450$ mm^3, covering an effective area of 673×450 mm^2. To prevent inefficiency at the segment boundaries, adjacent scintillator bars overlap by 1 mm. Scintillation light from each bar is collected by wavelength-shifting fibers and read out by 1×1 mm^2 multi-pixel photon counters (MPPCs; Hamamatsu S10362-11-100P) located at one end of each scintillator. A schematic drawing of the SCH layout is presented in Fig. 3.10.

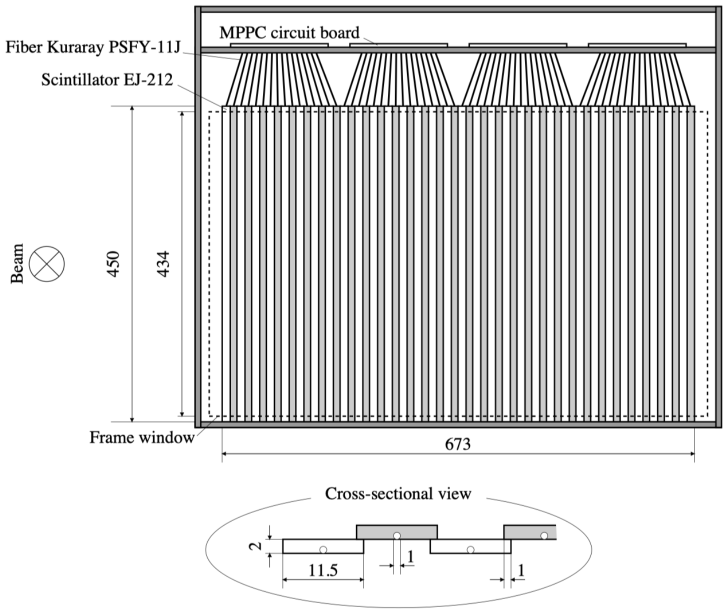

Figure 3.10: Schematic of the SCH. Top: Overall layout, composed of 64 plastic scintillator slats. Bottom: Detailed view, showing the 1 mm overlap between adjacent slats and the WLS fiber readout. The hodoscope provides a 2D matrix trigger by correlating hits with TOF counters, covering an effective area of 673×450 mm^2.).

BVH (Beam Veto Hodoscope)

The beam veto hodoscope (BVH) is installed just downstream of the KURAMA magnet and is designed to veto non-interacting beam particles that continue along the beam axis. It consists of 14 vertically segmented plastic scintillators (EJ-232), each with dimensions of $13 \times 5 \times 100$ mm^3. Although the initial design included 15 segments, only 14 were installed, providing a total effective width of approximately 182 mm. The BVH thus covers the entire acceptance of the outgoing charged particle region.

Each scintillator segment is equipped with three 3×3 mm^2 MPPCs (Hamamatsu S13060-3050PE), attached at both ends for dual readout. The signals from these MPPCs are combined into groups of two to five channels and integrated into the matrix trigger logic, which also incorporates timing information from the TOF, SCH, and BH2 detectors. Through this configuration, the BVH functions as part of the three-dimensional matrix trigger system for the (K^-, K^+) reaction. A schematic diagram of the BVH detector is shown in Fig. 3.11.

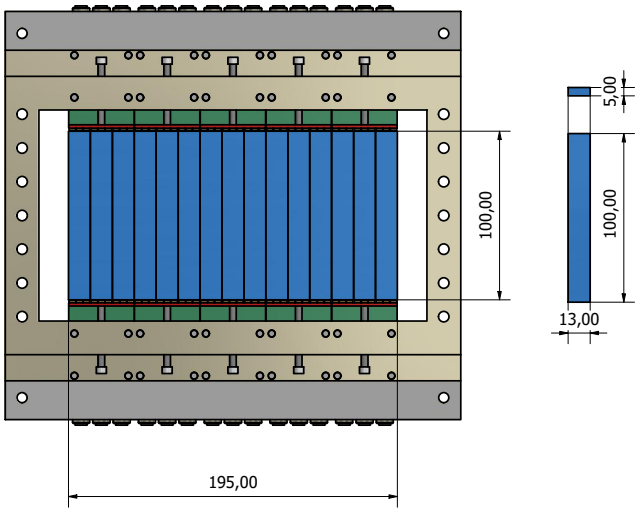

Figure 3.11: Schematic layout of the beam veto hodoscope (BVH). Each of the 14 installed segments is read out by three 3×3 mm^2 MPPCs, with nine MPPCs handled per readout board. Although 15 segments were originally designed, the leftmost one was omitted, resulting in an effective area of approximately 182×100 mm^2.

Time-of-Flight (TOF) Detector

The TOF (Time-of-Flight) wall was installed at the most downstream position of the KURAMA spectrometer to measure the flight time of protons between BH2 and the TOF wall. A schematic view of the TOF detector is shown in Fig. 3.12.

The detector consists of 24 plastic scintillator bars (EJ-200, Eljen Technology), each with a thickness of 30 mm. Each scintillator bar has dimensions of 80 mm in width and 1800 mm in height. Scintillation light was collected at both ends of each bar using acrylic light guides and detected by photomultiplier tubes (Hamamatsu H1949).

The TOF counter measures the time-of-flight of protons between BH2 and the TOF wall and provides precise timing information for particle identification. In addition to its timing role, the segment-wise hit positions are utilized as coarse position references for matching reconstructed tracks from SDC3 and SDC4. The intrinsic timing resolution of the TOF system is estimated to be 60–100 ps, and the attenuation length of the scintillator material is approximately 210 cm.

Large Aerogel Cherenkov (LAC) Counter

The large aerogel Cherenkov counter (LAC) was installed downstream of the TOF detector to reject scattered π^+ particles in the online trigger. The counter employs silica aerogel radiators with a refractive index of 1.05, optimized to generate Cherenkov photons from particles traveling with velocities exceeding $0.95c$. For pions, the Cherenkov threshold momentum corresponds to approximately 0.4 GeV/c.

The LAC has a sensitive area of 2080 mm $\times$ 1200 mm $\times$ 113 mm, and its inner walls are lined with aluminized Mylar sheets to improve light reflection and collection efficiency. Cherenkov light emitted in the aerogel is detected by 30 photomultiplier tubes (PMTs), consisting of 20 Hamamatsu R1584-01 tubes and 10 Burle 8854 tubes, mounted on the front face of the light-collection box. A schematic view of the detector layout is shown in Fig. 3.13.

The horizontal position of the LAC was offset by +45 cm along the x-axis to enhance the acceptance for positively charged protons emitted at forward angles.

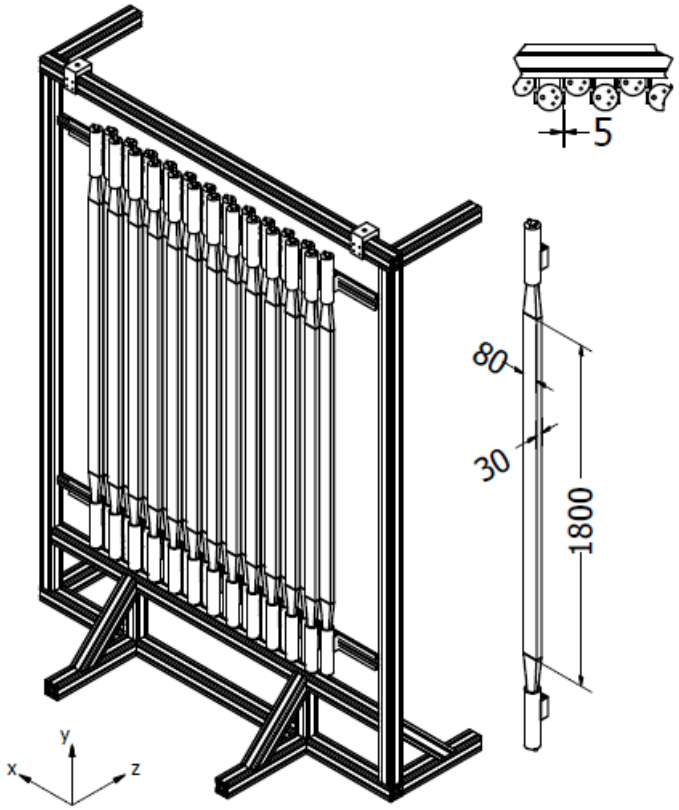

Figure 3.12: Schematic diagram of the forward time-of-flight (TOF) detector. To provide full angular coverage, the scintillator slats are positioned with a 5 mm overlap. Photomultiplier tubes located at both ends of each slat are used for signal readout. (from Ref. [71]).

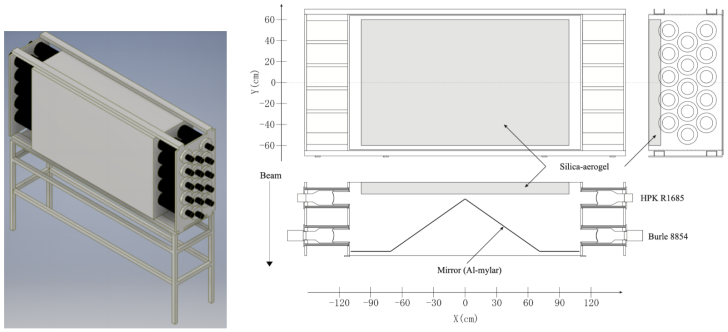

Figure 3.13: Schematic views of the LAC detector: (a) 3D rendering and (b) 2D layout. It consists of silica aerogel radiators ($n = 1.05$) and 30 PMTs (20 Hamamatsu, 10 Burle) enclosed in a light collection box. The system is designed to reject pions (threshold ≈ 0.4 GeV/c) and is shifted by +45 cm in x to optimize acceptance.

Water Cherenkov (WC) Counter

The water Cherenkov counter (WC) was positioned at the most downstream section of the E42 experimental setup, downstream of the LAC detector. Its x center was laterally displaced by +30 cm to increase the geometrical acceptance for scattered protons. The WC is designed to veto low-momentum protons by detecting Cherenkov photons generated in water.

The detector consists of 20 modules arranged in two layers to reduce detection inefficiency. Each module is a 20 mm thick acrylic vessel filled with deionized water, having dimensions of 257 mm $\times$ 207 mm $\times$ 1880 mm^3. The inner surfaces are lined with Tyvek reflector sheets to enhance photon collection efficiency, and both ends are sealed with 5 mm thick UV-transparent acrylic windows.

Cherenkov light produced in the water is detected by 2-inch photomultiplier tubes (PMTs; Hamamatsu H11284-100UV), which are optically coupled to the acrylic windows using optical grease (RX-688). The PMTs feature quartz windows and super bialkali photocathodes, achieving a peak quantum efficiency of 35% at a wavelength of 350 nm. The analog sum of the two PMT signals from each module is used in the online trigger logic to suppress position dependence along the y axis.

A schematic drawing of the WC detector layout is shown in Fig. 3.14.

3.5 Superconducting Hyperon Spectrometer

The Superconducting Hyperon Spectrometer (SHS) is a detector system designed to measure charged particles produced in the (K^-, p) reaction on a nuclear target. In addition to direct detection of primary particles such as p, $\pi^\pm$, and K^-, the SHS enables the reconstruction of secondary neutral particles, including Λ and $\overline{K^0}$, through their charged decay products.

The SHS consists of three main components: a superconducting dipole magnet, a central cylindrical time projection chamber called the Hyperon Time Projection Chamber (HypTPC), and a surrounding time-of-flight hodoscope array referred to as the Hyperon Time-of-Flight (HTOF) system. The HypTPC reconstructs the three-dimensional trajectories of charged particles and measures their specific energy loss (dE/dx) in the gas volume, while the HTOF provides precise time-of-flight (TOF)

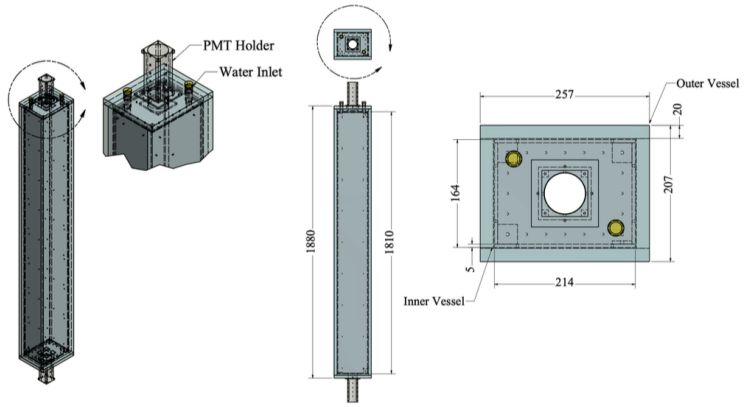

(a)

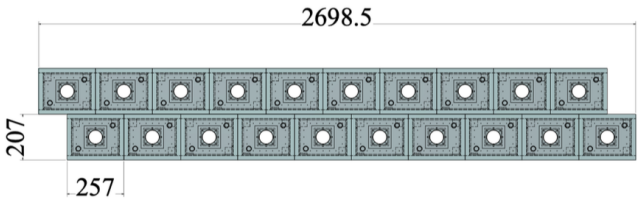

(b)

Figure 3.14: Schematic drawings of the WC detector.(a) A single module, illustrating the $257 \times 207 \times 1880$ mm^3 acrylic vessel, inner Tyvek reflector, and PMT readout at both ends. (b) Top view of the complete array, showing the arrangement of 20 modules stacked in two alternating layers. The detector is designed to suppress low-momentum protons (threshold 1.1 GeV/c) and is located at the most downstream position.

measurements for particle identification.

By combining the momentum analysis in the magnetic field with dE/dx information from the HypTPC and TOF information from the HTOF, the SHS achieves powerful particle identification (PID) capability over a wide kinematic range. Charged particle trajectories are reconstructed inside the HypTPC, which operates under a uniform 1 T magnetic field generated by Helmholtz-type superconducting coils. The curvature of these tracks provides momentum information, while the combination of dE/dx and TOF measurements allows discrimination among particle species.

The design and performance of the magnet, HypTPC, and HTOF subsystems are described in detail in the following subsections.

3.5.1 Superconducting Hyperon Spectrometer Magnet

The superconducting magnet of the SHS provides a highly uniform magnetic field for the tracking volume of the HypTPC. It is a Helmholtz-type dipole magnet designed to generate a vertical magnetic field so that the particle trajectories bend horizontally, allowing efficient momentum reconstruction for charged particles emitted from the target. The design value of the maximum magnetic field at the magnet center is 1.5 T, while the SHS was operated at 1.0 T during the E42 experiment.

The magnet structure consists of two superconducting coils with cryogenic cooling and current leads, thermal shielding against radiation, a vacuum vessel to prevent convective heat transfer, and an iron yoke for magnetic flux return. To ensure high uniformity of the magnetic field over the entire TPC volume, the two coils are axially separated by a distance equal to their radius (r = 500 mm), forming an optimized Helmholtz configuration.

Each coil is wound with 23.4 km of NbTi round superconducting wire, with a diameter of 0.77 mm and insulation of polyvinyl alcohol (PVA). The copper-to-superconductor ratio is 2.4, and the inductance of each coil is 103 H, resulting in a total system inductance of 231.3 H. The magnet was operated stably throughout the experimental period, and its field distribution was confirmed to be uniform within $\pm 0.5\%$ over the HypTPC region. A photograph and magnetic field map of the SHS magnet are shown in Fig. 3.15.

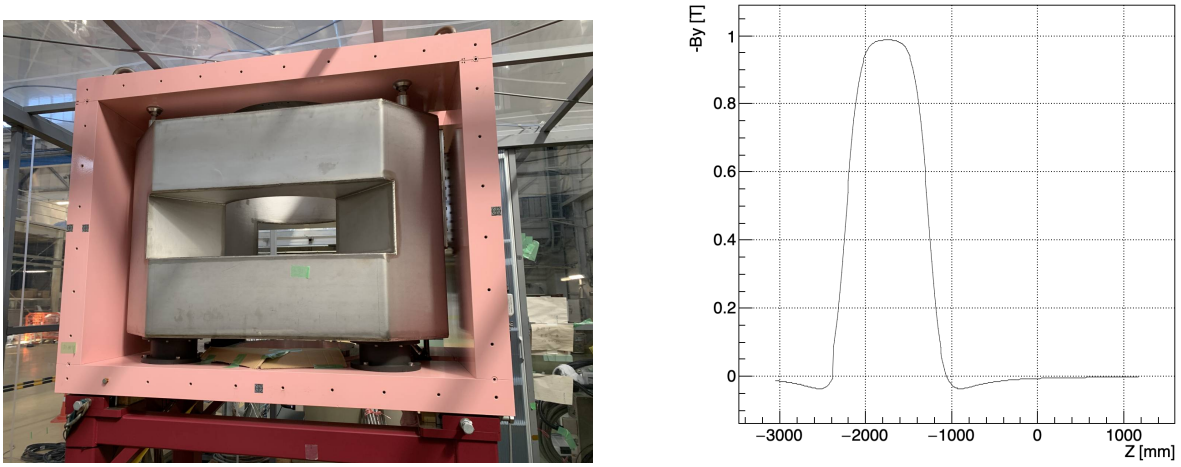

Figure 3.15: (a) Photograph of the SHS magnet. (b) Magnetic field distribution $-B_y$ at $x = 0$, $y = 0$ along the z-axis.

3.5.2 Hyperon Time Projection Chamber

The HypTPC is a cylindrical time projection chamber designed to reconstruct charged particle tracks with high spatial precision for the (K^-, p) reaction at $p_{K^-} = 1.8$ GeV/c. Its large acceptance and stable operation at high particle rates make it well suited for precision measurements of momentum and dE/dx for particle identification.

Fig. 3.16 shows the cross-section of the HypTPC internal structure. The readout plane, installed at the bottom of the drift volume, is composed of a gating grid, a triple-GEM stack, and an anode pad plane. The surrounding field cage and target holder are engineered to maintain a highly uniform electric field distribution.

The active volume is filled with Ar–CH_4 (P10) gas and provides a total vertical drift length of 550 mm. A uniform electric field of 130 V/cm is formed by applying a high voltage of -10 kV to the octagonal cathode plane. The average electron drift velocity under these conditions is 5.57 cm/μs. The field cage is constructed from 25 μm-thick flexible polyimide sheets printed with 2.0 mm-wide field strips at a pitch of 2.5 mm. The strips are arranged in parallel on both sides and connected via a 0.5 M resistor chain to create a linear voltage divider. To suppress charge accumulation caused by positive ions, the outer insulation layers between field strips were partially removed in the beam-through regions (upstream and downstream), each with an opening of 100×100 mm^2. The entire field cage is supported mechanically by a G-10 epoxy laminate frame. A target holder with a cross section of 34×24 mm^2 is positioned 143 mm upstream from

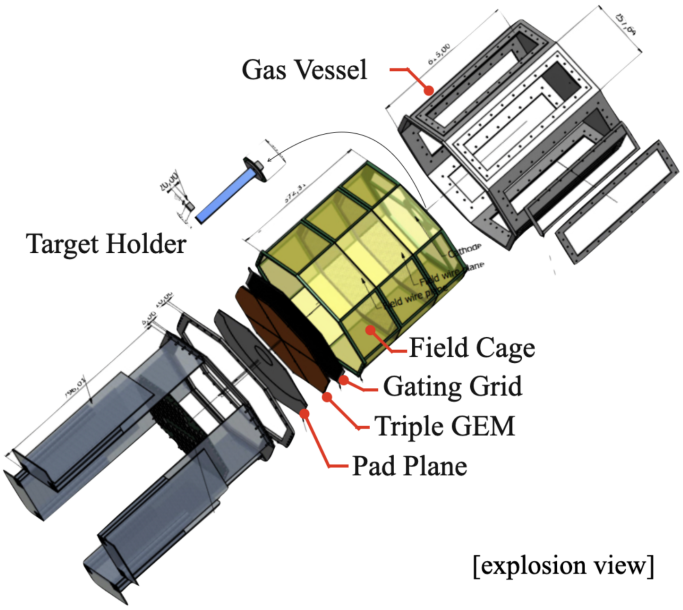

Figure 3.16: Cross-section of the HypTPC internal structure. The readout plane, installed at the bottom of the drift volume, is composed of a gating grid, a triple-GEM stack, and an anode pad plane. The surrounding field cage and target holder are engineered to maintain a highly uniform electric field distribution.

the TPC center.

Ionization electrons produced by charged particles drift downward toward the amplification region, which consists of a gating grid, a triple-GEM stack, and a pad readout plane. The gating grid is made of gold-plated Cu–Be wires with a diameter of 50 μm and a pitch of 1 mm, located 4.2 mm above the top GEM foil. The gate operates between $V_{\mathrm{Gate}} = \pm 25$ V and is synchronized with the trigger signal to minimize ion backflow. The triple-GEM stack provides a total gas gain of 10^4 with low discharge probability. The upper two GEM foils are 50 μm thick, while the bottom foil is 100 μm thick, and a voltage difference of approximately 307 V is applied across each foil. During physics runs, the HypTPC operated stably with an average spark rate of about six events per hour, and no damage to the GEM foils was observed.

The pad readout plane is divided into four azimuthal sectors. Each inner sector contains ten radial pad rows with pads 9 mm long and 2.1–2.7 mm wide, while each outer sector has 22 rows with pads 12.5 mm long and 2.3–2.4 mm wide. In total, the readout system has 5768 pads, with forward-going tracks typically producing signals

in up to 32 pad rows. Charge signals from the pads are read out using the General Electronics for TPCs (GET) system, which provides integrated digitization and scalable high-density data acquisition.

The performance of the HypTPC regarding spatial and momentum resolutions was evaluated using monochromatic π^- beam data. The momentum resolution $\Delta p/p$ was achieved to be approximately 3.0% at 0.5 GeV/c, and remained within 3.0–3.5% in the range of 0.3–0.6 GeV/c. The spatial resolution in the horizontal ($r\phi$) plane was approximately 400 μm on average. The intrinsic resolution σ_0 depends on the pad length, measured as 387 μm for the outer sector (12.5 mm length) and 750 μm for the inner sector (9.0 mm length), with additional dependencies on the track incident angle and diffusion. The details for the estimation of these values are explained in Ref. [72]. The vertical (y) spatial resolution was treated as a fixed value of 1.0 mm, as the dependence on drift length was negligible.

3.5.3 Hyperon Time-of-Flight Detector

The Hyperon Time-of-Flight (HTOF) system surrounds the HypTPC to provide precise timing information for charged particles emerging inside the HypTPC. It plays a crucial role in particle identification (PID) when combined with the momentum and specific energy loss (dE/dx) information obtained from the HypTPC. Through the measurement of flight time between the target and the HTOF counters, the SHS enables identification of primary charged particles produced in the (K^-, p) reaction—such as p, $\pi^\pm$, and K^-—as well as secondary neutral particles, including Λ and $\overline{K^0}$, reconstructed from their charged decay products.

The HTOF detector array consists of 34 plastic scintillator slats (EJ-232), each with a length of 1000 mm, arranged in an octagonal geometry around the HypTPC. Four scintillator slats are mounted on each face, except at the beam entrance, where two adjacent faces are replaced by four slats forming a beam window region. This configuration provides nearly full solid-angle coverage for particles emitted from the target while maintaining space for the incident beam.

Each central scintillator slat has a rectangular cross section of 70 mm $\times$ 10 mm, with an active area of approximately 800 mm in height excluding the light-guide regions. Both ends of the slat are tapered to 35 mm $\times$ 4 mm to couple with eight multi-pixel

photon counters (MPPCs, Hamamatsu S13360-3060PE), each with a sensitive area of 3 mm × 3 mm. The beam window consists of two shorter slats divided into upper and lower segments of 450 mm and 438 mm in length, respectively, allowing the beam axis to pass through a gap located 62 mm from the top edge and 50 mm from the bottom.

Signals from the MPPCs are first amplified by a differentiator-type preamplifier and subsequently shaped and summed by a wide-band amplifier circuit. The readout electronics employ the AD8000 ultra-fast operational amplifier to maintain high timing fidelity. Each processed signal is divided into two channels for simultaneous ADC and TDC readout, and individual MPPC gains are fine-tuned using onboard trimmers.

The intrinsic time resolution of a single HTOF counter is approximately 130 ps, which provides sufficient precision for distinguishing among protons, kaons, and pions over a flight path of about $350-400$ mm. By combining this TOF information with the dE/dx measurement from the HypTPC, a robust PID performance is achieved across a wide momentum range to around $1\,\mathrm{GeV}/c$.

A schematic drawing of the HTOF detector arrangement and the signal readout electronics is shown in Fig. 3.15.

3.6 Target

The target assembly of the E42 experiment comprises a diamond target, a polyethylene (CH_2) target, and a motorized vertical mover system. For wide angular acceptance, the target unit is positioned 143 mm upstream of the TPC center. The targets are mounted on a common support rod that is mechanically coupled to the arm of the motorized stage, enabling controlled vertical translation. The motion of the target is regulated through an external controller, which allows reproducible positioning and reliable switching between the two target configurations. By adjusting the vertical position, either the diamond or the CH_2 target can be placed in the beam line.

In addition, data were collected with the target system raised to its uppermost position, corresponding to an empty-target configuration, which was used for detector calibration purposes.

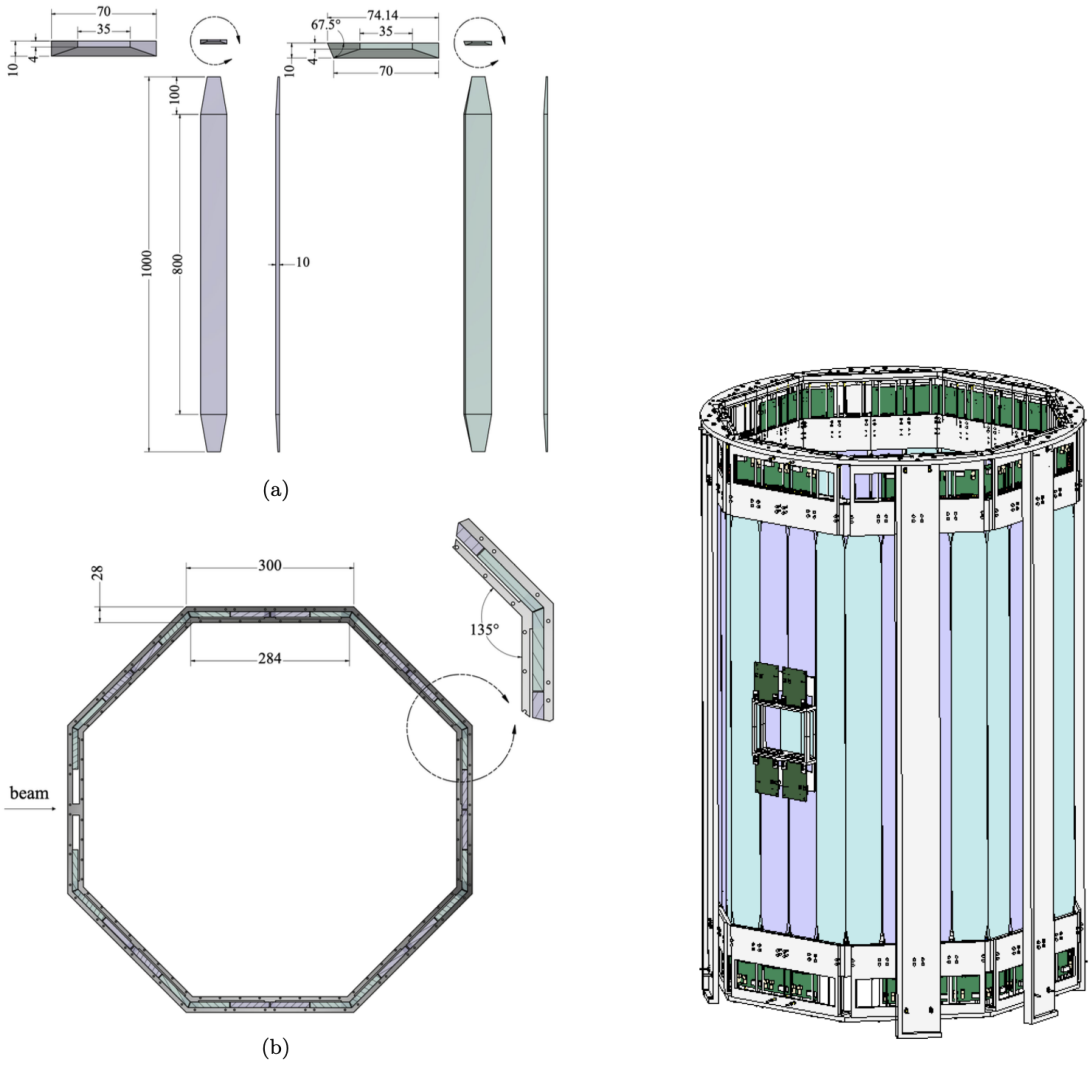

Figure 3.17: (Left) (a) A schematic of two kinds of HTOF scintillators placed on the sides (left) and on the corners (right). (b) A cross-sectional view of the HTOF scintillator array with the supporting frame. (Right) A schematic view of the HTOF assembly.

3.6.1 Diamond Target

The diamond target was fabricated by assembling twelve cubic diamond pieces, each with a volume of 1 cm^3. The individual blocks were bonded together using epoxy adhesive, forming a single composite structure. The resulting target block has an effective dimension of 30.3 mm in width, 20.2 mm in height, and 20.2 mm in thickness. The material density of the diamond used in the target was measured to be $\rho = 3.223$ g/cm^3.

3.6.2 Polyethylene Target

The polyethylene target was manufactured from high-density polyethylene material and mounted 5 mm above the diamond target by means of a G10 spacer. The block measures 33.5 mm in width, 50.0 mm in height, and 23.5 mm in thickness. Its extended height includes space for a screw hole used to attach the target assembly to the mover system. The density of the polyethylene target material is $\rho = 0.95$ g/cm^3.

3.7 Trigger and Data Acquisition

3.7.1 Trigger

The trigger system for the E42 experiment was implemented using a programmable logic module, referred to as the HUL module.This module receives input signals from various detector components, including the beam-line counters, scattered-particle hodoscopes, and matrix coincidence logic units. All input signals are synchronized with a 400 MHz internal clock, and their relative timing is adjusted for proper logical operation. Four independent trigger conditions, labeled Triggers A - D, were defined for data taking. Each condition was prescaled and logically combined within the HUL module, and the final trigger decision was sent to the Master Trigger Module (MTM).after coincidence with the accelerator spill gate.

Trigger A (inclusive (K^-, p) reaction):

Trigger A is designed to select inclusive (K^-, p) events by combining three logic components: the beam condition, the scattered-particle condition, and the matrix co-

incidence logic. The overall logic is expressed as:

$$KK \equiv K_{\mathrm{Beam}} \otimes p_{\mathrm{Scat}} \otimes \mathrm{Mtx}. \tag{3.1}$$

The beam condition K_{Beam} is defined by a triple coincidence among the beam counters:

$$K_{\mathrm{Beam}} \equiv \mathrm{BH1} \otimes \mathrm{BH2} \otimes \mathrm{BAC}, \tag{3.2}$$

where BH1 and BH2 are the OR-ed outputs of the beam hodoscope segments, and BAC is the analog-sum discriminator output used to reject pion contamination in the beam.

The scattered-particle condition is defined as:

$$p_{\mathrm{Scat}} \equiv \mathrm{TOF} \otimes \mathrm{LAC} \otimes \mathrm{WC}, \tag{3.3}$$

where TOF corresponds to the mean-timer outputs of segments #7 - 24, while LAC and WC provide veto signals to suppress π and p backgrounds, respectively.

The matrix coincidence condition (Mtx) ensures geometrical correlation between the beam and scattered particles. It is implemented as:

$$\mathrm{Mtx} \equiv \mathrm{2DMtx} \otimes \overline{\mathrm{3DMtx}}, \tag{3.4}$$

where 2DMtx represents a two-dimensional coincidence matrix between the SCH and TOF detectors ($64 \times 24 = 1{,}536$ possible combinations), and 3DMtx corresponds to a three-dimensional coincidence among BH2, SCH, TOF, and BVH segments ($8 \times 64 \times (24 + 4) = 14{,}336$ combinations). The 3DMtx veto is applied to suppress beam-related accidental backgrounds. The hit distribution between TOF and SCH segments, forming the 2DMtx basis, is shown in Fig. 3.18.

Although this trigger is optimized for (K^-, K^+) events, positively charged particles such as protons and π^+ produced in $(K^-,\ p)$ or other associated reactions can also satisfy the same coincidence condition. Consequently, the same trigger configuration allows simultaneous acquisition of (K^-, p) reaction data.

Trigger B (exclusive (K^-, p) reaction):

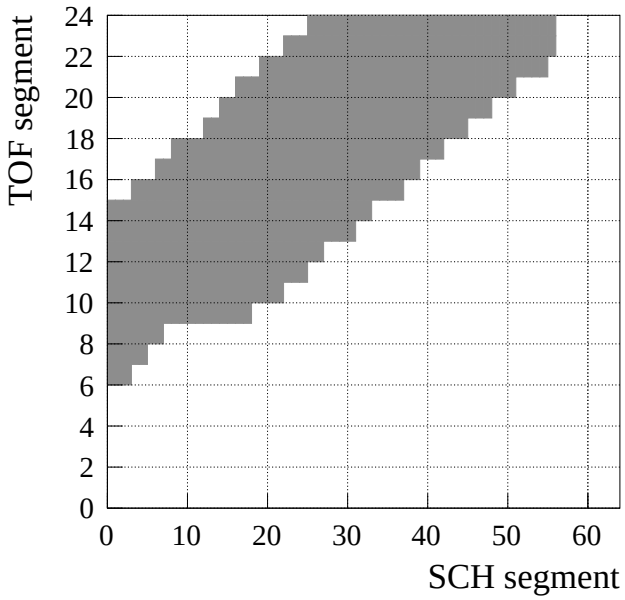

Figure 3.18: Hit combination of TOF and SCH segments used to define the 2D matrix trigger (2DMtx). Each entry corresponds to a valid coincidence between a TOF segment and an SCH segment.

Trigger B, denoted as KK_{excl}, is based on the same (K^-, p) coincidence logic as Trigger A but includes an additional multiplicity requirement on the HTOF detector. Specifically, events with at least two hits among the 34 HTOF segments (denoted as HTOF-Mp$\geq$ 2) are selected. This condition enhances the selection of exclusive events in which hyperons are produced and decay inside the TPC volume, providing sensitivity to hyperon final states such as Λ and Ξ decays.

Trigger C (scattered-particle calibration):

Trigger C is intended for detector calibration and timing alignment. It requires a beam particle passing through BH1 and BH2, in coincidence with TOF segments (#7 - 24) and BVH, while applying a 3D matrix veto. The (K^-, p) coincidence condition is not required, making this trigger useful for measuring detector responses independent of the main physics selection.

Trigger D (beam monitoring):

Trigger D is a pure beam trigger that only requires coincidence between BH1 and BH2, without any additional condition on scattering or matrix logic. It records unscattered beam particles to monitor the beam profile and to evaluate trigger bias effects by comparison with the main physics triggers. Because it accepts all beam-induced

reactions within the HypTPC acceptance, it is also used to study background rates and detector stability.

Trigger operation and prescale factors:

All four trigger conditions (A - D) were logically OR-ed, and prescale factors were applied before forming the final trigger output. Trigger B served as the primary physics trigger and was recorded without suppression, while Trigger A was also taken simultaneously for inclusive analysis. Triggers C and D were recorded with high prescale factors to reduce event rates during data taking. For a typical K^- beam intensity of 530 k/spill, the prescale factors were set to 600 for Trigger C and 13,200 for Trigger D, while the prescale for Trigger A varied depending on the run condition. Fig. 3.19 shows the logic circuit for Trigger A and B, and Fig. 3.20 shows the matrix coincidence logic of 2DMtx and 3DMtx signals.

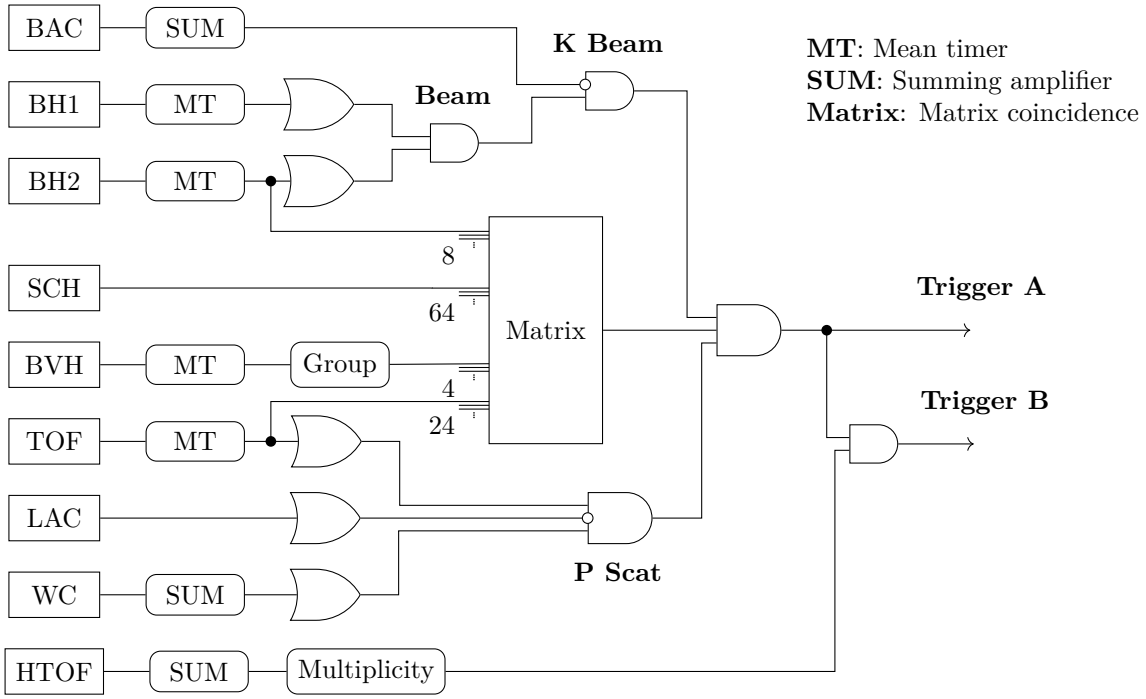

Figure 3.19: Logic diagram of the (K^-, p) reaction trigger.

3.7.2 Data Acquisition

Several types of readout architectures, including the VME, EASIROC, and HUL systems, were employed in the experiment. To achieve integrated data acquisition among the subsystems, a network-based framework, Hadron DAQ (HDDAQ), was adopted.

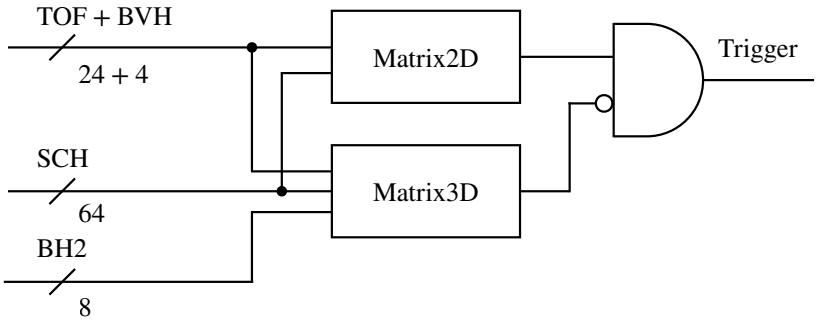

Figure 3.20: An additional HUL module was employed for the matrix coincidence logic, and the resulting 2DMtx and 3DMtx signals were sent to the HUL trigger module.

HDDAQ operated through the TCP/IP protocol and worked in conjunction with a trigger and event-tag distribution system implemented with a Master Trigger Module (MTM). A schematic diagram of the DAQ system is shown in Fig. **??**.

The MTM distributed trigger and event-tag signals to all subsystems. The trigger signal served as a gate for the ADC modules and as a common stop for the TDC modules. The event data of each subsystem were labeled with spill and event numbers to ensure synchronization. Busy signals from all subsystems were also sent back to the MTM. During beam extraction, triggers were accepted only within the spill gate and when no subsystem was in a busy state. This configuration maintained consistency of event numbering among all subsystems throughout data taking.

In the VME subsystem, QDC modules (CAEN V792) were used to digitize the energy-deposition signals from BH1, BH2, TOF, and AC detectors. The digitized data were transferred to a VME-based CPU module serving as a front-end processor. Timing information from the BFT and SCH detectors was digitized by EASIROC modules.

The HUL subsystem employed multiple dedicated modules. The HUL high-resolution multi-hit TDC (HUL HRTDC) was used for the timing measurements of BH1, BH2, TOF, and AC detectors, and additional MHTDC modules (HUL MHTDC) were used for the timing information of the wire chambers. Data from the EASIROC and HUL

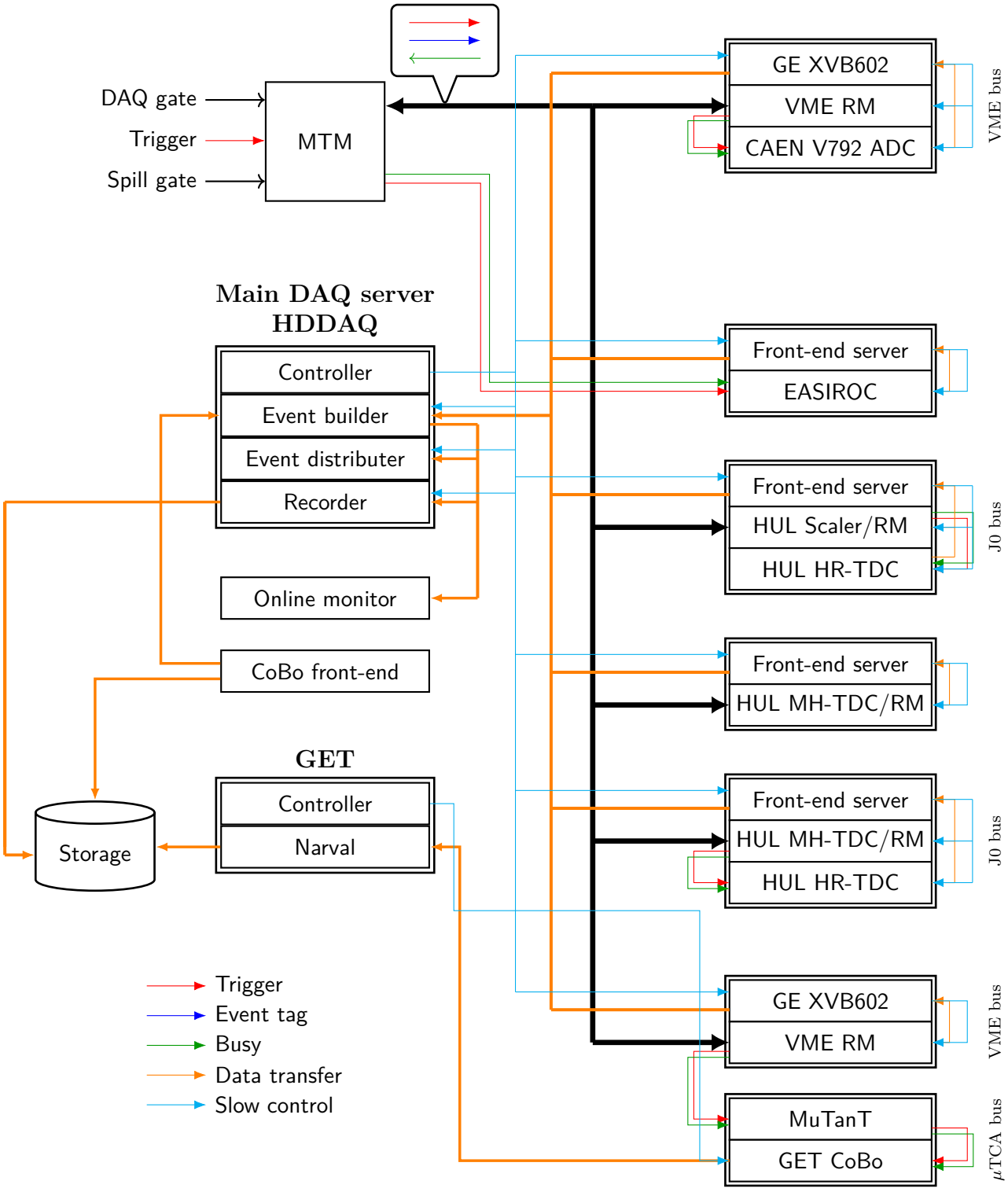
DAQ gate
Trigger
Spill gate
MTM
GE XVB602
VME RM
CAEN V792 ADC
VME bus
Main DAQ server
HDDAQ
Controller
Event builder
Event distributer
Recorder
Online monitor
CoBo front-end
Front-end server
EASIROC
Front-end server
HUL Scaler/RM
HUL HR-TDC
J0 bus
Front-end server
HUL MH-TDC/RM
Front-end server
HUL MH-TDC/RM
HUL HR-TDC
J0 bus
GET
Controller
Narval
Storage
GE XVB602
VME RM
VME bus
MuTanT
GET CoBo
μTCA bus
Trigger
Event tag
Busy
Data transfer
Slow control

modules were transferred to front-end computers through SiTCP communication.

The HypTPC system operated as an independent DAQ subsystem based on the General Electronics for TPCs (GET) platform. Trigger and busy signals were shared with the MTM via a VME-RM interface connected to the MuTanT module within the GET system. Each CoBo front-end digitized the signals from AGET chips and sent them to the main DAQ server, where HDDAQ combined the TPC data with those from other subsystems to form complete events. Each CoBo module processed up to four AsAd boards, corresponding to 1024 channels. In total, 31 AsAd boards and 8 CoBo modules, accommodating 124 AGET chips, were used to read out all HypTPC pads.

The spatial arrangement of the 31 AsAd boards on the TPC pad plane is illustrated in Fig. 3.21a. Each board corresponds to a specific region in the (X, Z) plane, and the four AGET chips on each board are assigned to distinct channel groups, with chip IDs 1–4 represented by blue, green, orange, and red, respectively, as shown in Fig. 3.21.

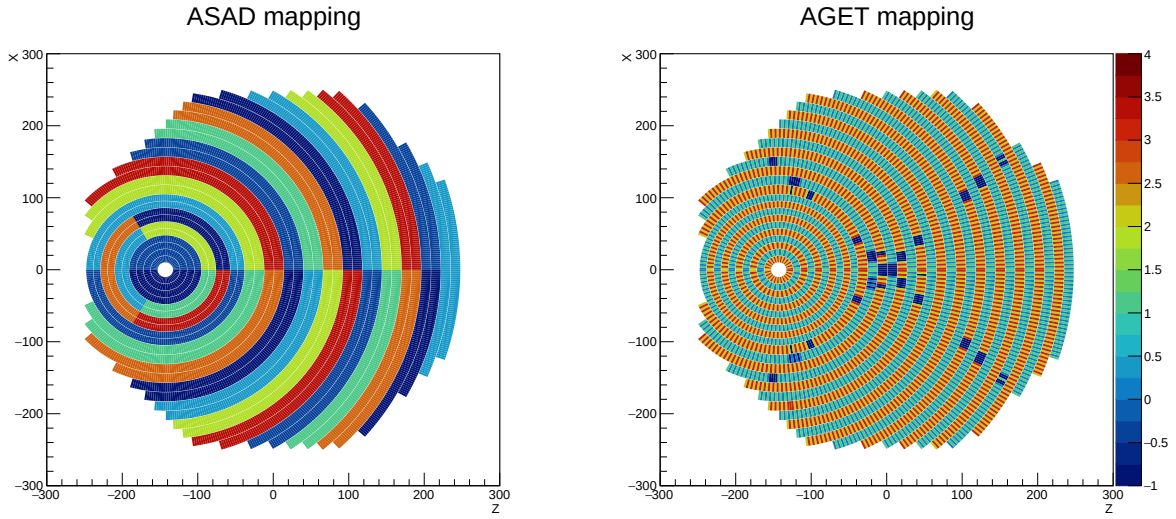

(a) (b)

Figure 3.21: (a) Spatial distribution of the 31 AsAd boards on the HypTPC pad plane. (b) Color-coded mapping of the four AGET chips on each AsAd board: blue (chip 1), green (chip 2), orange (chip 3), and red (chip 4).

The DAQ efficiency was evaluated for each run under different K^- beam intensities. Typical efficiencies ranged from 88% to 96%.

3.8 Data Summary

The E42 experiment was conducted at the J-PARC K1.8 beamline, comprising two distinct operation periods. The first stage, a commissioning run carried out between May 11 and 19, yielded 1.5 effective days of beam exposure. The subsequent physics run extended from May 25 to June 29, corresponding to 25.5 days of data acquisition with an overall downtime fraction of approximately 8%. Across both stages, data sets suitable for detector calibration as well as physics analyses were systematically collected.

The principal data set was obtained with a diamond target irradiated by a 1.8 GeV/c K^- beam. In total, around 1.8×10^{11} incident K^- events were accumulated. During the run, the GEM voltage was initially set to 285 V and progressively raised to 307 V. Data corresponding to voltages below the final setting (285–306 V) represent approximately 22% of the full statistics. For the present study, the analysis was restricted to the 1.4×10^{11} K^- events recorded under the stable condition of $V_{\mathrm{GEM}} = 307$ V.

In addition, dedicated data-taking with a hydrogen target were performed to investigate the K^- detection efficiency via the $p(K^-, pK^-)$ elastic scattering process and the Λ reconstruction efficiency via the $p(K^-, K^+)\Xi^-$ reaction. A polyethylene (CH_2) target served these purposes, providing a data sample of 6.2×10^9 K^- events.

Chapter 4

Inclusive Analysis

4.1 Overview

This chapter details the comprehensive analysis procedure for reconstructing the $^{12}\mathrm{C}(K^-, p)$ reaction and deriving its inclusive spectrum. The analysis integrates data from the entire experimental setup, establishing the foundation for the exclusive measurements presented in the subsequent chapter.

Fig. 4.1 shows the analysis flow which begins with the reconstruction of the incident K^- beam using the K1.8 beamline spectrometer. This involves particle identification, momentum determination, and tracking, which provide the initial state kinematics.

Next, the scattered proton is reconstructed. This is a multi-stage process that starts with local tracking in the KURAMA spectrometer's drift chambers (SDC1–SDC4). The analysis is then significantly enhanced by incorporating information from the Hyperon Time Projection Chamber (HypTPC). This chapter describes the full TPC analysis pipeline, including signal processing, hit clustering, track reconstruction via Hough transform and Kalman filtering, and detailed calibration procedures. The combination of KURAMA and HypTPC data allows for precise global tracking and momentum reconstruction of the scattered proton.

Finally, using the reconstructed four-momenta of the incident K^- and the scattered proton, the missing mass of the reaction is calculated. This chapter concludes with the derivation of the inclusive differential cross-section. The resulting spectrum is validated by comparing it with previous experimental data, confirming the reliability of our analysis framework. This inclusive spectrum serves as the essential baseline for the

exclusive analysis of the escape K^- process, which is the focus of Chapter 7.2.

In this chapter, the detection efficiency and the single-hit (single-track) efficiency are defined as $N(hit \geq 1)/N(all)$ and $N(hit = 1)/N(hit \geq 1)$, respectively

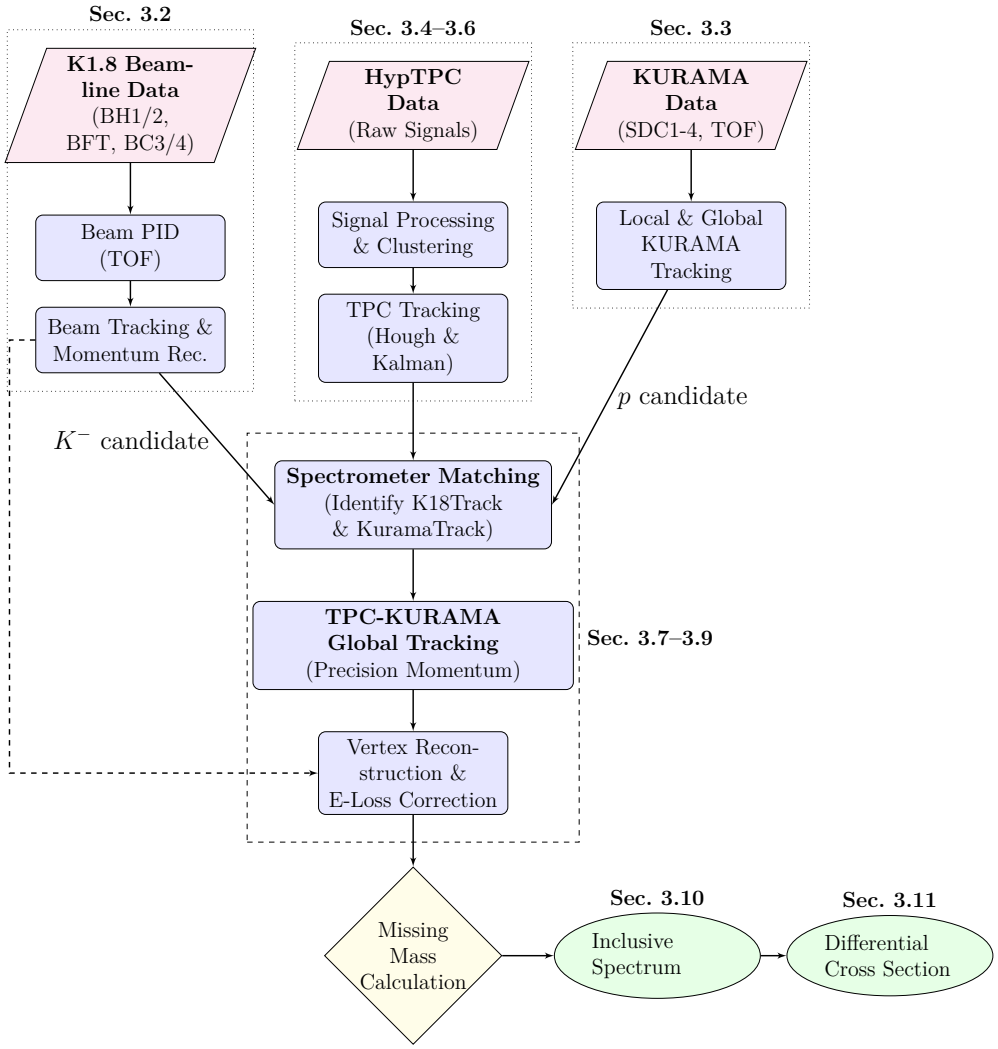

Figure 4.1: Flowchart of the analysis procedure for the $^{12}C(K^-, p)$ reaction inclusive spectrum.

4.2 K^- Beam Analysis

The analysis of the incident K^- beam was performed to accurately reconstruct the beam trajectory, momentum, and timing, which serve as the basis for the downstream (K^-, p) reaction analysis. The K1.8 beamline spectrometer and associated detectors provided precise information on the beam particle identification and tracking. This section describes the procedures for identifying K^- mesons, reconstructing their trajectories and momenta, and evaluating the overall beam-tracking efficiency.

4.2.1 Beam Identification

The K^- beam was identified using the beamline scintillation counters BH1 and BH2, the Beam Fiber Tracker (BFT), and the drift chambers BC3 and BC4. These detectors provided timing, position, and tracking information, respectively, for determining the particle species and beam trajectory on an event-by-event basis.

Particle identification was primarily achieved by measuring the time-of-flight (TOF) between BH1 and BH2. The two scintillators, located upstream and downstream of the QQDQQ magnet system, provided precise timing signals, allowing separation of K^- mesons from background π^- and protons. The distance between BH1 and BH2 is approximately 10 m, corresponding to a TOF difference of about 1.1 ns between K^- and π^- at a beam momentum of 1.8 GeV/c. A timing gate of ± 2 ns was applied to define valid K^- beam events, effectively suppressing contamination from lighter particles.

The BFT, consisting of multiple scintillating fibers with fine segmentation, provided precise spatial measurements of the beam profile at the entrance of the beamline spectrometer. A correlation analysis between the BFT hit position and the BH1 segment ID was performed to ensure spatial consistency. Events showing a one-to-one correspondence between BFT and BH1 hits were selected as well-defined K^- beam events, effectively removing accidental coincidences. The BFT hit efficiency, evaluated within a timing window of ± 5 ns, was found to be 98.6%, while the single-hit efficiency was 97.8%. These results demonstrated stable detector performance over the entire data-taking period.

4.2.2 Momentum Reconstruction

The incident beam momentum is reconstructed using the K18 beam line spectrometer. The tracking procedure involves analyzing data from the upstream fiber tracker (BFT) and the downstream drift chambers (BcOut) to reconstruct the particle trajectory through the K1.8 dipole magnet.

Upstream Tracking (BFT)

The BFT detects the beam position upstream of the QQDQQ magnet.

- **Time Window Cut**: A strict time window of ± 5 ns is applied to BFT hits to

reject accidental backgrounds.

- **Hodoscope Matching**: Reconstructed clusters in the BFT are required to be geometrically consistent with the hit segment in the upstream beam hodoscope (BH1).
- **Cluster Selection**: Events are required to have exactly one valid cluster in the BFT to ensure a clean single-track candidate.

Downstream Tracking (BcOut)

The BcOut drift chambers measure the track downstream of the magnet. The tracking in the BcOut is performed to reconstruct three-dimensional trajectories of beam particles using hit positions on BC3 and BC4.

Hit Selection To reduce noise and accidental hits, the following cuts are applied:

- **Time-over-Threshold (TOT)**: Hits with TOT less than 15 ns are rejected.
- **Drift Time**: Only hits with drift times within the range of -10 to 50 ns are accepted.
- **Multiplicity**: A maximum of 16 hits per plane is allowed.
- **Layer Requirement**: Hit combinations having at least 8 layers out of 12 layers are accepted as track candidates.

Track Reconstruction Tracks are reconstructed as straight lines using the method of least squares. The track is parameterized with x_0, y_0, u_0, and v_0, which denote the horizontal and vertical positions at the origin ($z = 0$) and the slopes dx/dz and dy/dz, respectively. The hit position s_i^{hit} typically has a left/right ambiguity. To solve this, a pair plane analysis method is applied. Each pair of planes (xx', uu', and vv') is considered as one unit. The combinations of hits are composed of six pairs. If hits exist in only one layer of a pair, both left and right hit positions are calculated and tested.

Candidates are sorted according to a reduced chi-squared (χ^2) defined as:

$$\chi^2 \equiv \frac{1}{n-4} \sum_{i=1}^{12} H_i \left(\frac{s_i^{hit} - s^{track}(z_i)}{\sigma_i} \right)^2 \tag{4.1}$$

where:

- $n = \sum H_i$ is the number of hits.
- $H_i = 1$ if the i-th layer has a hit, 0 otherwise.
- $s^{track}(z_i) = x(z_i)\cos\alpha_i + y(z_i)\sin\alpha_i$ is the calculated position with wire tilt angle α_i.
- $x(z_i) = x_0 + u_0 z_i$, $y(z_i) = y_0 + v_0 z_i$.
- σ_i is the position resolution of the i-th layer (typically around 180 μm).

Quality Cuts Sorted tracks with duplicate hits are rejected. Finally, a cut of $\chi^2 < 30$ is applied to ensure track quality and reject tracks with incorrect left/right resolution. Reconstructed track segments are also required to match the hit segment in the downstream beam hodoscope (BH2).

The single-track reconstruction efficiency of the K1.8 beamline spectrometer was found to be 96.6% with an uncertainty of ±0.004% (stat.), as evaluated using the BFT-tagged K^- beam events.

Momentum Reconstruction

The full beam trajectory is reconstructed by combining the upstream position measured by the BFT and the downstream track segment measured by the BcOut. The momenta of beam particles are reconstructed using a third-order transfer matrix M, which was calculated by the ORBIT code [**ORBIT**] based on the TRIO program [73]. The relationship between the phase space coordinates at the entrance and exit of the K1.8 beam line spectrometer is expressed as:

$$\vec{X}_{in} = M(\vec{X}_{out}, \delta) \tag{4.2}$$

where:

- $\vec{X}_{in} = (x_{in}, y_{in}, \frac{dx_{in}}{dz}, \frac{dy_{in}}{dz})$ denotes the horizontal and vertical positions and their slopes at the entrance ($z = 0$, BFT position).
- $\vec{X}_{out} = (x_{out}, y_{out}, \frac{dx_{out}}{dz}, \frac{dy_{out}}{dz})$ denotes those at the exit (BcOut position).
- δ is the momentum deviation from the central momentum p_0, defined as $p = p_0(1 + \delta)$.

The parameter x_{in} is determined from the hit cluster position on the BFT. The momentum deviation δ is obtained by solving the third-order equation derived from the transfer matrix elements, $x_{in} = f(\vec{X}_{out}, \delta)$. Finally, the beam track is extrapolated to the target position to define the interaction vertex.

The reconstructed momentum was then corrected for the energy loss in the upstream materials using the Bethe formula. The resulting momentum distribution showed a central value of approximately 1.82 GeV/c with a full width at half maximum (FWHM) of 3.6%, consistent with the designed beam optics as shown in Fig. **??**.

4.2.3 Efficiency for K^- Beam

The overall efficiency for identifying valid K^- beam tracks (ε_{K^-}) was evaluated as the product of multiple independent efficiency factors, including the detection efficiency of each subsystem, the K^- survival probability during flight, and the geometrical acceptance of the target. The efficiency can be expressed as:

$$\varepsilon_{K^-} = \varepsilon_{\mathrm{BH1\&BH2}} \cdot \varepsilon_{\mathrm{BTOF}} \cdot \varepsilon_{\mathrm{BFT}}^{\mathrm{single}} \cdot \varepsilon_{\mathrm{K1.8}}^{\mathrm{single}} \cdot \varepsilon_{K^-\text{-survival}} \cdot \varepsilon_{\mathrm{target}}.$$

Here, $\varepsilon_{\mathrm{BH1\&BH2}}$ represents the detection efficiency of the beam hodoscopes, and $\varepsilon_{\mathrm{BTOF}}$ denotes the efficiency of the time-of-flight cut. $\varepsilon_{\mathrm{BFT}}^{\mathrm{single}}$ and $\varepsilon_{\mathrm{K1.8}}^{\mathrm{single}}$ correspond to the single-track reconstruction efficiencies of the BFT and the K1.8 spectrometer, respectively. $\varepsilon_{K^-\text{-survival}}$ accounts for the survival probability of K^- against decay in flight, and $\varepsilon_{\mathrm{target}}$ is the geometrical acceptance of the beam on the target.

Each efficiency term was evaluated on a run-by-run basis, and the standard deviation across runs was treated as a systematic uncertainty to account for variations in beam intensity and detector conditions. The BTOF efficiency was fixed at 100.0%, as its inefficiency was found to be negligible. For the calibration data obtained with the CH_2 target, the overall beamline performance was highly stable. For the diamond target data, 13 run groups were analyzed separately to evaluate possible variations in tracking efficiency under different beam intensities.

The survival probability of the K^- meson was estimated considering its decay in flight between BH2 and the target. Using the measured path length of 0.59 ± 0.0004 m and the average beam momentum, the survival efficiency was calculated to be 95.8%.

Table 4.1: Summary of K^- beam tracking efficiencies for the diamond target data across all run groups. Quoted values show the observed range per group; fixed or common quantities are indicated accordingly.

Efficiency Factor	**Description**	**Value [%]**
$\varepsilon_{\mathrm{BH1\&BH2}}$	BH1 & BH2 detection efficiency	95.39 – 97.45
$\varepsilon_{\mathrm{BTOF}}$	BTOF cut efficiency	100.00 (fixed)
$\varepsilon_{\mathrm{BFT}}^{\mathrm{single}}$	BFT single-hit detection efficiency	97.65 – 98.19
$\varepsilon_{\mathrm{K1.8}}^{\mathrm{single}}$	K1.8 single-track reconstruction efficiency	95.30 – 97.59
$\varepsilon_{K^-\text{-survival}}$	K^- survival probability to the target	95.77 ± 0.01
$\varepsilon_{\mathrm{target}}$	Geometrical acceptance to the target cross section	89.35 ± 1.35
ε_{K^-}	**Total K^- beam tracking efficiency**	75.96 – 79.91

Table 4.2: Comparison of K^- beam tracking efficiencies for the CH_2 and diamond targets.

Efficiency Factor	**CH_2 Target [%]**	**Diamond Target [%]**
$\varepsilon_{\mathrm{BH1\&BH2}}$	97.42 ± 0.10	95.39–97.45
$\varepsilon_{\mathrm{BTOF}}$	100.00 (fixed)	100.00 (fixed)
$\varepsilon_{\mathrm{BFT}}^{\mathrm{single}}$	97.83 ± 0.10	97.65–98.19
$\varepsilon_{\mathrm{K1.8}}^{\mathrm{single}}$	96.61 ± 0.10	95.30–97.59
$\varepsilon_{K^-\text{-survival}}$	95.77 ± 0.01	95.77 ± 0.01
$\varepsilon_{\mathrm{target}}$	88.00 ± 2.51	89.35 ± 1.35
ε_{K^-}	**77.60±2.22**	**75.96–79.91**

The geometrical acceptance to the target cross section was evaluated by fitting the x- and y-position distributions of the incident beam at the target plane. For the diamond target, the acceptance efficiencies were found to be 93.7% in the x-direction and 95.3% in the y-direction, yielding a combined efficiency of $89.35 \pm 1.35\%$.

By combining all factors, the total K^- beam-tracking efficiency for the diamond target runs ranged from 76.0% to 79.9%, depending on the beam conditions. For the CH_2 target runs, a representative total efficiency was determined to be $77.6 \pm 2.2\%$. A summary of the efficiency components for the diamond target is provided in Table 4.1, and a comparison with the CH_2 target data is shown in Table 4.2. These results demonstrate that the beamline detectors and reconstruction framework provided stable and high-quality K^- beam information, sufficient for use in the downstream (K^-, p) physics analysis.

4.3 KURAMA Particle Tracking

4.3.1 Track Reconstruction

The momentum of scattered particles is reconstructed using the Kurama spectrometer referred to as KURAMA Tracking. The tracking system consists of input drift chambers (SdcIn) located upstream of the Kurama magnet, output drift chambers (SdcOut) located downstream, and a Time-of-Flight (TOF) wall. The local tracking in SdcIn and SdcOut is performed solely for the selection of track candidates. Using proton-identified tracks from this KURAMA tracking, a more precise track reconstruction—called TPC-KURAMA tracking—was performed by incorporating the HypTPC clusters into the global fit, further improving the accuracy of the reconstructed proton momentum and spatial resolution, which is explained in Sec. 4.7.

Upstream Tracking (SdcIn)

The local track reconstruction at the entrance of the Kurama magnet is performed using the SDC1 and SDC2 drift chambers. SDC1 consists of six wire planes with $uu'xx'vv'$ orientation and tilt angles of 15°, 0°, and −15°, while SDC2 comprises four wire planes in the $xx'yy'$ configuration tilted at 0° and 90°.

- **Hit Selection**: Valid hits are selected based on Time-over-Threshold (TOT) cuts (min. 20 ns for SDC1, 90 ns for SDC2) and drift time windows. A multiplicity cut (max. 16 hits per plane) is applied.

- **Track Reconstruction**: A straight-line approximation is adopted for track fitting. Track parameters are defined as (x_0, y_0, u_0, v_0), where x_0, y_0 differ from the magnet center. The hit position is calculated based on the measured drift length dl and the incident angle θ. The track parameters are iteratively optimized by minimizing the reduced chi-square defined as:

$$\chi^2_j = \frac{1}{n-4} \sum_{i=1}^{n} w_i^j \left(X_i^j - X_i^{track,j} \right)^2 \tag{4.3}$$

where $w_i^j = (W_i/\sigma_i^2) \cos\theta_i^{j-1}$ is the weight including the angle correction, and X_i^j is the hit position updated at each iteration j using the incident angle from

the previous step. The iterative process continues until the convergence criterion $|\chi^2_{j+1} - \chi^2_j|/\chi^2_j < 0.003$ is satisfied. The typical χ^2 distribution in SDCIn tracking is shown in Fig. 4.2. Spatial resolutions of SDC1 and SDC2 were typically 199-225 μm and 280-328 μm, respectively.

- **Quality Cut**: A quality cut of $\chi^2 < 30$ is applied to the final track candidates. Tracks are required to have at least 8 valid hits across the two chambers.

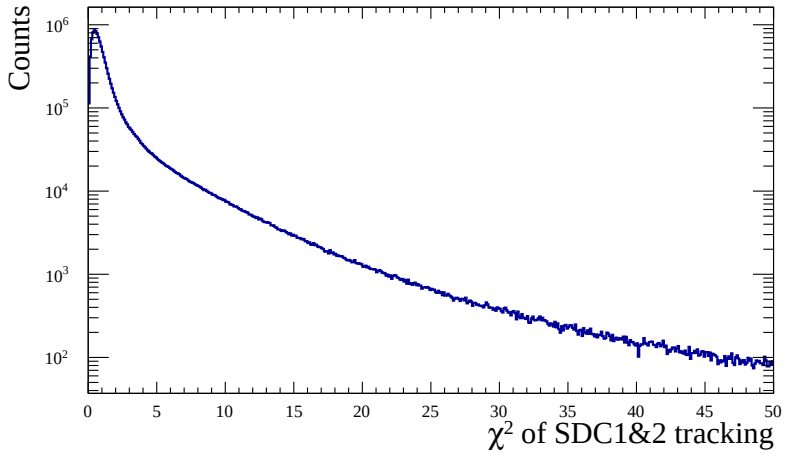

Figure 4.2: Distribution of the reduced χ^2 for SDC1 and SDC2 tracking.

Downstream Tracking (SdcOut)

Local track reconstruction at the exit of the Kurama magnet is performed using the SDC3 and SDC4 drift chambers. SDC3 features a wire spacing of 8 mm with planes oriented in $xx'yy'$ and tilted at 0° and 90°. SDC4 has a larger wire spacing of 20 mm with $yy'xx'$ planes tilted at 90° and 0°. Due to the similar honeycomb structure, the tracking method is identical to that used for SdcIn (iterative least-squares fit with straight-line approximation).

- **Hit Selection**: Hits are selected based on TOT cuts (min. 50 ns for SDC3, 20 ns for SDC4) and drift time windows. A multiplicity cut (max. 16 hits per plane) is applied.

- **Track Reconstruction**: Only tracks with hits in at least 6 layers across the two chambers are reconstructed. Since both SDC3 and SDC4 measure x and y

positions, the TOF detector is also utilized for tracking. The extrapolated track position at the TOF wall is compared with the TOF hit position in both x and y directions. The typical χ^2 distribution in SdcOut tracking is shown in Fig. 4.3. The spatial resolutions were typically 364-425 μm for SDC3 and 463-533 μm for SDC4. The vertical (y) hit position in the TOF is calibrated using experimental data (e.g., beam-through π^-).

- **Quality Cut**: Reconstructed tracks in SdcOut are required to have a $\chi^2 < 40$.

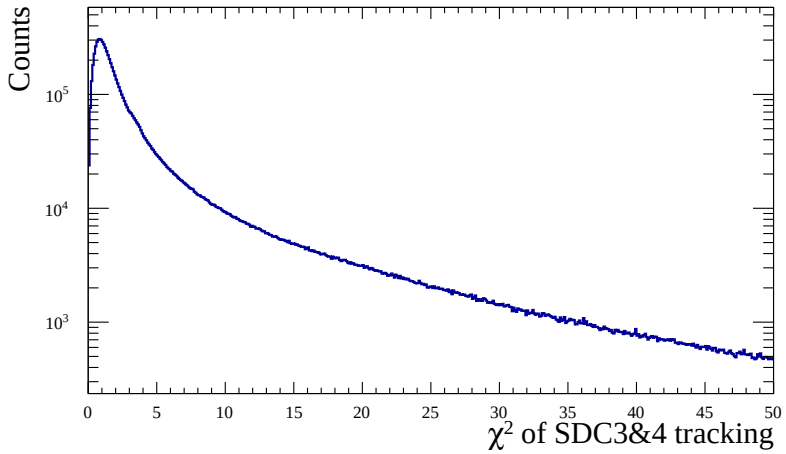

Figure 4.3: Distribution of the reduced χ^2 for SDC3 and SDC4 tracking.

Full Track Reconstruction

The full trajectory of the scattered particle is reconstructed by determining the momentum that best matches the upstream (SdcIn) and downstream (SdcOut) track candidates through the Kurama magnetic field. This tracking is performed solely for the selection of track candidates.

- **Matching**: The SdcIn and SdcOut tracks are connected using a Runge-Kutta method or a transport matrix integration through the magnetic field map.
- **Global Cut**: A final quality cut of $\chi^2 < 40$ is applied to the full track fit. The typical χ^2 distribution in Kurama tracking is shown in Fig. 4.4.
- **Track Selection**: Events are required to have exactly one successfully reconstructed track in the Kurama spectrometer to ensure a unique definition of the scattered particle kinematics.

- **Particle Identification**: The time-of-flight is measured between the experimental Time-Zero (determined by BH2) and the TOF wall. Combined with the reconstructed path length and momentum, the mass-squared (m^2) of the particle is calculated for particle identification.

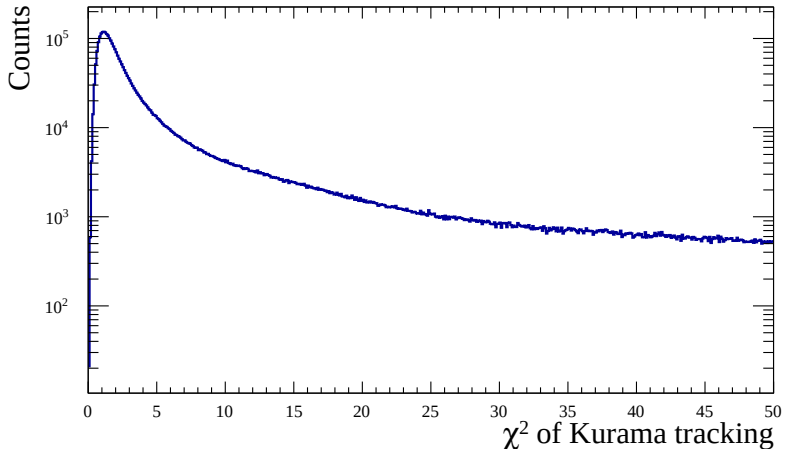

Figure 4.4: Distribution of the reduced χ^2 for KURAMA tracking.

4.3.2 Tracking Efficiency

SdcIn Local Tracking Efficiency

The tracking efficiency of SDC1 and SDC2 was evaluated using well-identified K^- beam events. Beam particles were selected by requiring a single hit in the HTOF detector and applying a spatial cut on the vertical hit position, $|y_{\mathrm{HTOF}}| < 100$ mm as shown in Fig. 4.5. Events satisfying these conditions were defined as

$$N(K\mathrm{Beam} = 1).$$

The local tracking efficiency was calculated as the fraction of selected beam events in which at least one SDCIn track was successfully reconstructed:

$$\varepsilon_{\mathrm{SdcIn}} = \frac{N(\mathrm{SdcInTrack} \geq 1 \times K\mathrm{Beam} = 1)}{N(K\mathrm{Beam} = 1)}.$$

This procedure isolates clean beam events and provides an unbiased estimate of the intrinsic tracking performance of the SDC1 and SDC2 chambers.

The tracking efficiency was found to be $99.87 \pm 0.002\%$(stat.) with the condition of $\chi^2 < 30$.

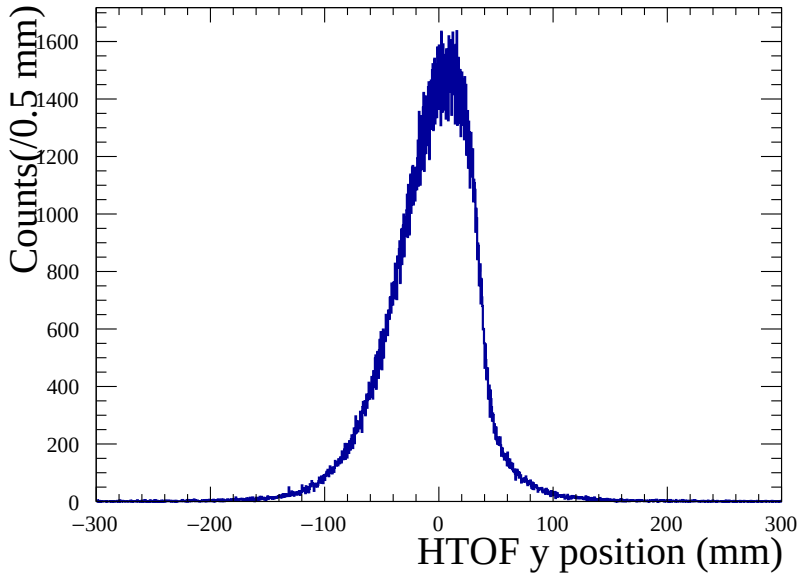

Figure 4.5: Distribution of the vertical hit coordinate (y) in the HTOF. Only events satisfying $|y| < 100$ mm were used in the evaluation of the SDCIn tracking efficiency.

SdcOut Local Tracking Efficiency

Events satisfying these conditions were defined as

$$N(\text{Proton} = 1) \equiv N(K\text{Beam} = 1 \times \text{SdcInTrack} \geq 1 \times \text{PID}_{\text{proton}}).$$

The SdcOut tracking efficiency was then calculated as

$$\varepsilon_{\text{SdcOut}} = \frac{N(\text{SdcOutTrack} \geq 1 \times \text{Proton} = 1)}{N(\text{Proton} = 1)}.$$

Using a reduced-χ^2 threshold of $\chi^2 < 40$, the tracking efficiency of the SDC3–SDC4 system was determined to be $98.87 \pm 0.04\%$ (stat.).

4.4 TPC Signal Processing and Hit Clustering

The following sections detail the analysis of data from the HypTPC, a central detector in this study. The analysis pipeline described here—encompassing signal processing,

hit clustering, track reconstruction, and calibration—forms the common foundation for both the inclusive analysis presented in this chapter (particularly for refining the momentum reconstruction of the scattered proton) and the exclusive analysis of escape K^- events, which will be detailed in Chapter 7.2.

The fundamental step in data processing is the analysis of the raw signal waveform acquired on the readout pad plane. A hit is formally registered whenever a pad records a signal amplitude that exceeds a predefined threshold. However, the raw digitized signal is often contaminated by common-mode noise, which is predominantly induced by the operational cycles of the TPC's gating grid. Accurate track reconstruction necessitates the precise subtraction of this noise component.

To isolate the pure ionization signal, an event-by-event baseline correction procedure is implemented. This method constructs a reference noise waveform for each event by selecting a pad within the expected signal region that exhibits the minimum peak ADC value, assuming this pad contains no real ionization signal. The noise model is then applied to the raw signals of all other pads by scaling and shifting the reference waveform $h(x)$ according to the function:

$$f(x) = p_0 + p_1 \cdot h(x + p_2), \tag{4.4}$$

where p_0 is the ADC offset, p_1 is the scaling factor, and p_2 represents the time bucket shift. Subtracting this modeled noise from the raw signal yields the corrected waveform.

Following noise subtraction, the waveform is fitted to extract the two essential physical observables: the drift time and the integrated charge. Due to the inherent non-symmetric profile of the signal pulse shaped by the shaping amplifier, the fitting utilizes a sum of multiple asymmetric Modified Gumbel functions:

$$f(t) = \sum_{i=1}^{n} A_i \cdot \exp\left(-\frac{t - t_i}{\tau_i}\right) \cdot \exp\left(-\exp\left(-\frac{t - t_i}{\tau_i}\right)\right) + C, \tag{4.5}$$

where A_i, t_i, and τ_i correspond to the amplitude, peak drift time, and width parameter of the i-th hit component, respectively, and C is a constant pedestal. The drift time t_i determines the particle's vertical position (y-coordinate) relative to the pad plane.

To reconstruct the spatial position of ionization, hits on adjacent pad rows are spatially correlated and grouped into a "cluster". A cluster is defined as a sequence of

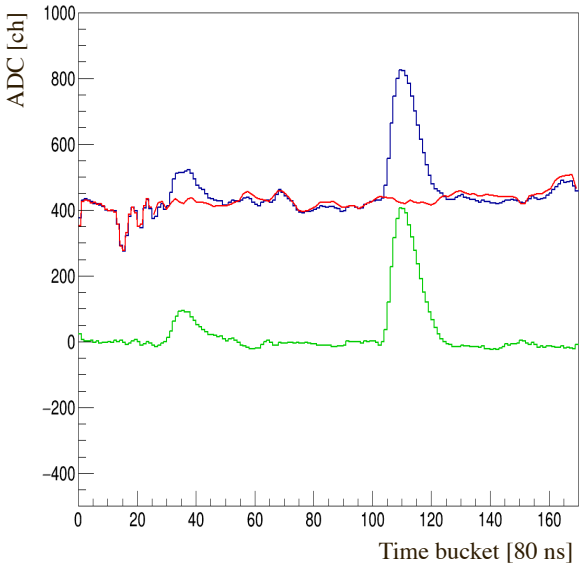

Figure 4.6: Example of waveform processing. (Left) Raw waveform contaminated with common-mode noise. (Right) Corrected waveform after baseline subtraction showing clear signal peaks.

two or more consecutive active pads. The precise coordinate of the cluster along the pad row is determined by calculating the charge-weighted center of gravity:

$$X_{\text{cluster}} = \frac{\sum_i x_i Q_i}{\sum_i Q_i}, \tag{4.6}$$

where x_i is the position of the i-th pad and Q_i is the measured charge. This method effectively utilizes charge sharing between pads to achieve a spatial resolution significantly better than the physical pad pitch.

The cluster charge is also used to calculate the specific energy loss, dE/dx, which is vital for particle identification. Due to the long tail of the Landau distribution characterizing energy deposition, a simple arithmetic mean would be biased by large fluctuations. To mitigate this, a truncated mean method is applied:

$$\left\langle \frac{dE}{dx} \right\rangle = \frac{1}{N_{\text{trunc}}} \sum_{j=1}^{N_{\text{trunc}}} \frac{Q_j^{\text{cl}}}{L_{\text{path}}}, \tag{4.7}$$

where Q_j^{cl} is the cluster charge, L_{path} is the track path length over the pad row, and the summation runs over the lowest 80% of the clusters (discarding the top 20% with the highest charge).

4.5 TPC Track Reconstruction

Track reconstruction from the set of 3D space points (clusters) is performed in two stages: initial track finding using the Hough transform and precise track fitting using the Kalman Filter.

4.5.1 Track Finding via Hough Transform

The objective of track finding is to identify subsets of clusters that form continuous helical trajectories in the TPC volume. The Hough transform technique is employed for its robustness against noise and high hit multiplicity. In the conformal projection of the xz-plane (perpendicular to the magnetic field), a circular trajectory passing through the origin can be mapped to a straight line or a peak in parameter space. Specifically, we utilize a modified Hough space defined by:

$$r = x \cos\theta + z \sin\theta, \tag{4.8}$$

where (x, z) are the cluster coordinates, and (r, θ) are the Hough parameters. Clusters belonging to the same helical track create a local maximum (peak) in the (r, θ) density map. By identifying these peaks, track candidates are extracted. This process is iterative; once a track candidate is found, its associated clusters are removed, and the transform is repeated to find subsequent tracks.

4.5.2 Kalman Filter Fitting

The track candidates obtained from the Hough transform are used as seeds for a precise fit. The fitting is performed using a Kalman Filter algorithm implemented within the GENFIT library [**genfit**]. The Kalman Filter is an iterative estimator that optimally updates the track state vector (position, momentum, and charge) by incorporating measurements layer by layer. Crucially, this framework accounts for physical effects such as continuous energy loss and multiple Coulomb scattering as the particle traverses the detector gas and materials.

The track state is initialized with the parameters from the Hough transform. During the fit, the algorithm also attempts to attach nearby clusters that were missed in the

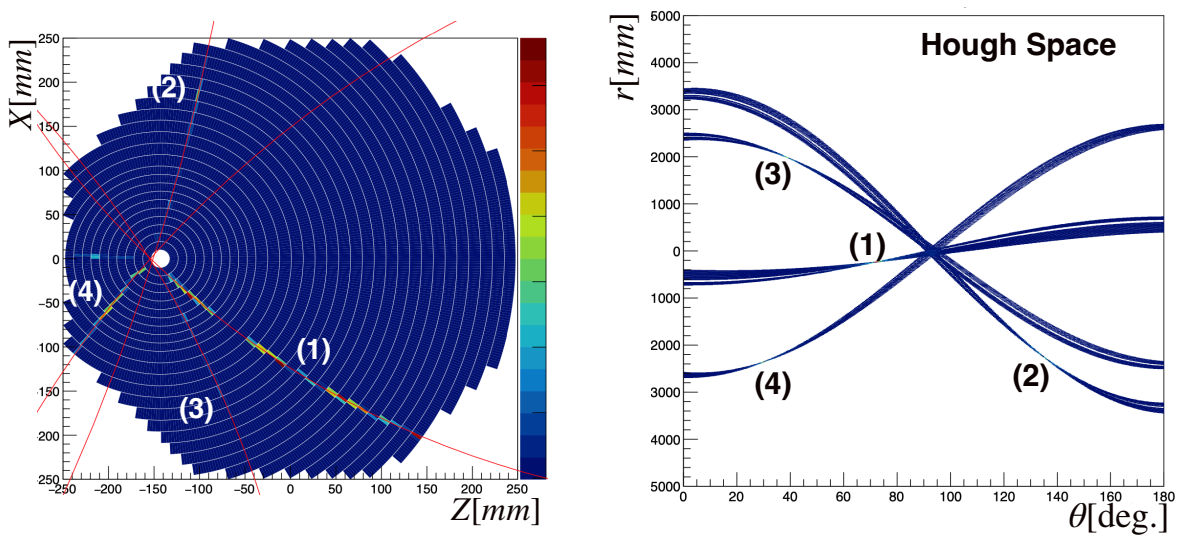

(a) (b)

Figure 4.7: (a) Reconstructed helix tracks from a single HypTPC event. (b) Hough space in the (r, θ) plane, where each cluster maps to a sinusoidal curve. Local maxima formed by curve intersections correspond to track candidates. Track numbers in (b) match those in (a).

finding stage or to reject outliers that degrade the fit quality (χ^2). In this analysis, valid tracks are required to originate from the target region defined by the spectrometer vertex reconstruction, ensuring they correspond to particles emitted from the (K^-, p) reaction. Tracks with a low number of clusters or poor χ^2 are discarded to maintain high reconstruction purity.

4.6 TPC Track Categorization and Selection

Following the track reconstruction and calibration steps, a high-level categorization is performed for all reconstructed HypTPC tracks. Since the HypTPC operates under a high-intensity beam condition, the reconstructed tracks include not only the reaction products of interest but also unreacted beam particles, scattered beam backgrounds, and accidental pile-up tracks. To ensure a clean sample for the subsequent particle identification (PID) and missing-mass analysis, tracks are classified into specific categories based on their geometric association with external spectrometers, kinematic properties, and topological features.

4.6.1 Spectrometer Matching

The primary tracks associated with the (K^-, p) reaction—the incident kaon and the scattered proton—are identified by matching HypTPC tracks with trajectories reconstructed by the external spectrometers.

- **Incident Beam Matching (K18Track):** A HypTPC track is identified as the incident K^- if it geometrically matches the trajectory reconstructed by the K1.8 beamline spectrometer. The matching criteria require the presence of TPC clusters in the upstream region ($z < z_{target} - 10$ mm) and spatial consistency with the extrapolated K1.8 track. The residual windows for this matching are defined as 10.5 mm in the xz-plane and 15.0 mm in the y-direction. TPC Tracks satisfying these conditions are flagged as `K18Track`.

- **Scattered Proton Matching (KuramaTrack):** Similarly, the scattered proton is identified by matching a HypTPC track with a track reconstructed by the KURAMA spectrometer. Candidates are selected based on charge consistency (positive) and the presence of clusters downstream of the target ($z > z_{target}$). The spatial matching windows at the target plane are set to 45.0 mm in the xz-plane and 30.0 mm in the y-direction. TPC Tracks satisfying these criteria are flagged as `KuramaTrack`.

4.6.2 Beam and Accidental Background Suppression

To isolate the reaction vertex and decay products, tracks originating from beam-through events or accidental coincidences must be suppressed.

- **Beam-through Tracks (BeamTrack):** Tracks that traverse the sensitive volume passing through the target region with high momentum and a small dip angle are categorized as beam-through tracks. specifically, tracks with a radius of curvature $r > 3000$ mm and a slope $|dz/ds| < 0.05$ are flagged as `BeamTrack`. These tracks are excluded from the candidate list for scattered kaon and other decay products.

- **Accidental Tracks (AccidentalTrack):** Tracks that do not originate from the reaction vertex or are inconsistent with the reaction timing are classified as

accidental tracks. This category includes:

1. High-momentum tracks ($r > 3000\,\mathrm{mm}$) with a large dip angle ($|dz/ds| \geq 0.05$).
2. Scattered beam-like particles ($r > 1200\,\mathrm{mm}$) that do not satisfy the K1.8 matching criteria.
3. Tracks associated with a vertex significantly displaced from the target volume (e.g., $|y_{vtx}| \geq 30\,\mathrm{mm}$), indicating accidental pile-up events.

Tracks flagged as `AccidentalTrack` are rejected from the physics analysis.

4.6.3 Topological Classification

In addition to the geometric classification, tracks with specific topological features are identified to improve the reconstruction quality and purity.

- **Electron Rejection (ElectronTrack):** Low-momentum background electrons are produced primarily by electromagnetic interactions in the target. To improve the purity of hadronic tracks, electron candidates are identified based on a momentum cut ($|p/q| < 0.1\,\mathrm{GeV/c}$) and specific energy loss (dE/dx) conditions. TPC Tracks exhibiting a dE/dx value consistent with electrons ($|n\sigma_e| < 3.5$) and inconsistent with pions ($n\sigma_\pi < -3.5$) are flagged as `ElectronTrack` and removed from the hadron candidate list.

Figure 4.8 demonstrates a typical event display after applying the categorization algorithms. In the high-intensity beam environment of the J-PARC E42 experiment, multiple tracks are often recorded simultaneously within the TPC sensitive volume, as shown in the figure. By utilizing the geometric associations with the external spectrometers and topological event features, the analysis framework successfully classifies these tracks. The incident beam (red) and the scattered proton (magenta) are correctly assigned, while unreacted beam particles and accidental pile-up tracks are isolated as background (grey). Consequently, the remaining track (cyan) is exclusively selected as a signal candidate. This categorization ensures that only relevant tracks are utilized for the missing-mass reconstruction of the (K^-, p) reaction and the analysis of hyperon decay products.

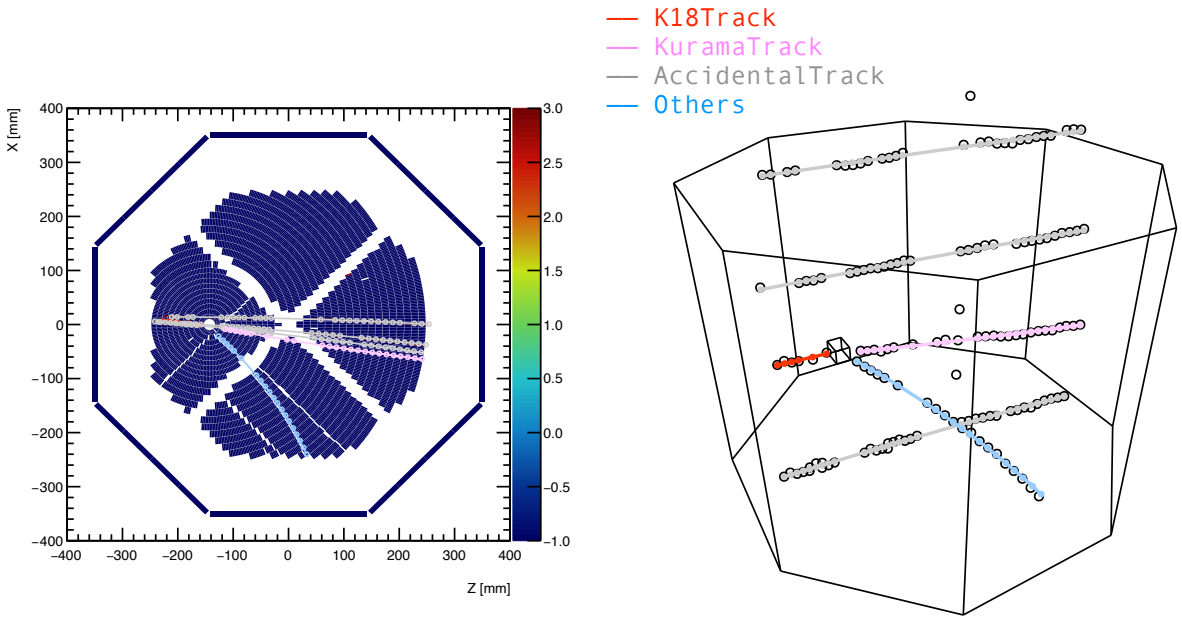

Figure 4.8: Typical event display reconstructed in the HypTPC. The left panel shows the projection on the horizontal (xz) plane, where the beam direction corresponds to the positive z-axis. The right panel presents the three-dimensional view of the same event. Reconstructed tracks are categorized based on the selection criteria described in the text: the incident K^- track matched with the K1.8 spectrometer (red, `K18Track`), the scattered proton track matched with the KURAMA spectrometer (magenta, `KuramaTrack`), and beam-through or pile-up tracks identified as background (gray, `AccidentalTrack`). The remaining track (cyan) is selected as a candidate for a reaction product, such as a scattered K^- or a hyperon decay particle, to be used in the subsequent physics analysis.

This track categorization is fundamental to the analyses in both this chapter and the next. The tracks identified as `KuramaTrack` are utilized in the subsequent sections of this chapter to refine the momentum reconstruction of the scattered proton for the inclusive analysis. The same categorization procedure is also applied in the exclusive analysis detailed in Chapter 7.2. In that chapter, tracks that are not classified as `K18Track`, `KuramaTrack`, `AccidentalTrack`, or `ElectronTrack` are treated as candidates for the escape K^-, and are subjected to a detailed particle identification procedure to purify the signal.

4.7 Scattered Proton Analysis

4.7.1 Global TPC-KURAMA Tracking

The local SdcIn and SdcOut tracks were connected through the KURAMA magnetic field using a fourth-order Runge - Kutta integration of the particle equations of motion. Input parameters were the track positions and slopes at the entrance and exit of the field region. The 3D magnetic field map of the SHS and KURAMA magnets was calculated using ANSYS Maxwell 3D, and the combined field was tabulated with a grid size of 1 mm^3.

The trajectory and momentum were obtained by minimizing the reduced chi-square:

$$\chi^2 = \frac{1}{n-5}\sum_{i=1}^{n} w_i \left(X_i^{\rm hit} - X_i^{\rm track}\right)^2,$$

where n is the number of valid hits and w_i is the weight determined by the detector resolution. The typical χ^2 distribution in the KURAMA tracking is shown in Fig. 4.4. Convergence was defined when $\left|\chi^2_{j+1} - \chi^2_j\right| / \chi^2_j < 2 \times 10^{-4}$ or when 100 iterations were reached.

The selected (K^-, p) candidates were further analyzed using the HypTPC. For a more accurate determination of the scattered p momentum and trajectory, a TPCK-URAMA global tracking method was employed, combining the information from both the HypTPC and the KURAMA spectrometer.

To identify the scattered p among HypTPC tracks, the KURAMA track was extrapolated upstream to the target position, and a rectangular matching window was

applied (± 45 mm in the XZ plane and ± 30 mm in Y). HypTPC tracks whose hit clusters lay within this window and had the same charge as the scattered p were selected as matching candidates. The residuals were defined as the differences between each TPC cluster and the extrapolated KURAMA track position.

The reduced chi-square used in the global fit was defined as

$$\chi^2_j = \frac{1}{n + 2n_{\mathrm{TPC}} - 5}\left[\sum_{i=1}^{n} w_i^j \left(X_i^j - X_i^{\mathrm{track},j}\right)^2 + \sum_{i=1}^{n_{\mathrm{TPC}}} \left(\frac{x_i^{\mathrm{TPC}} - x_i^{\mathrm{track}}}{\sigma_{x,i}}\right)^2 + \sum_{i=1}^{n_{\mathrm{TPC}}} \left(\frac{y_i^{\mathrm{TPC}} - y_i^{\mathrm{track}}}{\sigma_{y,i}}\right)^2\right] \tag{4.9}$$

where the first term accounts for the SDC residuals, while the second and third terms represent the x- and y-coordinate residuals of the HypTPC clusters with respect to the extrapolated KURAMA track.

The reconstructed p momentum was corrected in two ways; one is for removing angle dependence as explained in Sec. 4.8.4, and the other is for energy loss in materials upstream of the TOF detector using the Bethe formula. After determining the (K^-, p) reaction vertex, an additional correction was applied for the energy losses of both the K^- and p inside the target material.

To ensure that the tracks reconstructed in the HypTPC and the KURAMA spectrometer originate from the same particle, a track matching procedure was applied. The matching quality represents the consistency between the inner track (HypTPC) and the outer track (KURAMA). The tracks from the KURAMA spectrometer were extrapolated to the target position, and the spatial deviations from the corresponding HypTPC tracks were evaluated.

Figure 4.9 displays the distributions of the positional residuals between the HypTPC tracks and the extrapolated KURAMA tracks. The left panel shows the residual in the horizontal (x-z) plane, defined as the radial distance:

$$\delta_{xz} = \sqrt{(x_{\mathrm{HypTPC}} - x_{\mathrm{KURAMA}})^2 + (z_{\mathrm{HypTPC}} - z_{\mathrm{KURAMA}})^2} \tag{4.10}$$

The right panel shows the residual in the vertical (y) direction, defined as:

$$\delta_y = y_{\mathrm{HypTPC}} - y_{\mathrm{KURAMA}} \tag{4.11}$$

Both histograms are plotted for the track candidates that fall within the predefined matching window.

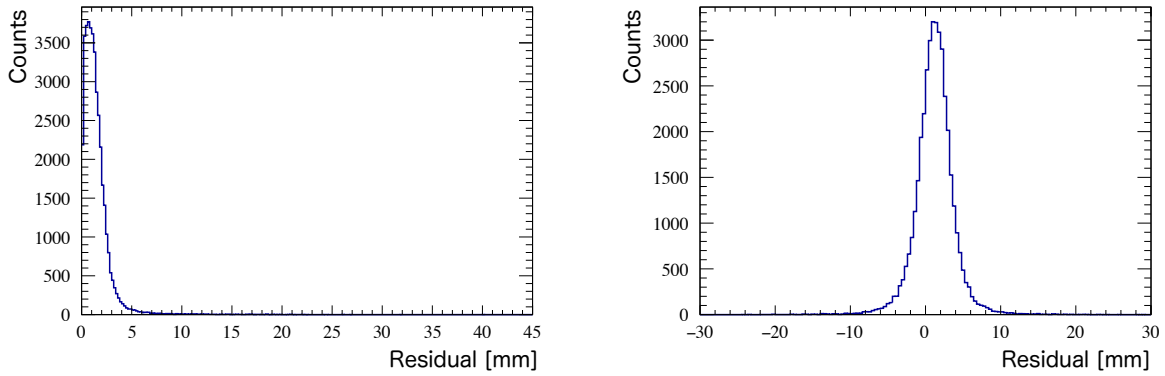

Figure 4.9: Distributions of positional residuals between HypTPC tracks and extrapolated KURAMA tracks at the target position. The left panel shows the radial residual in the x-z plane, and the right panel shows the residual in the y direction. Both histograms are plotted for tracks within the defined matching window.

4.7.2 Efficiency for Scattered Proton Tracking

The tracking efficiency of the KURAMA spectrometer for scattered protons was evaluated using a sample of proton candidates identified by the upstream drift chambers (SdcIn) and the Time-of-Flight (TOF) wall. The efficiency, $\varepsilon_{\mathrm{KURAMA}}$, is defined as the probability that a proton track detected in the upstream region is successfully connected to the downstream system (SdcOut) and reconstructed as a global track:

$$\varepsilon_{\mathrm{KURAMA}} = \frac{N(\mathrm{KURAMA\ Track} \geq 1 \wedge \mathrm{Proton} = 1)}{N(\mathrm{Proton} = 1)}, \tag{4.12}$$

where $N(\mathrm{Proton} = 1)$ denotes the number of events with a valid SdcIn track identified as a proton by PID, and the numerator represents the subset of those events where at least one global KURAMA track was reconstructed.

The "Proton" sample used in the denominator was selected by combining kinematic and PID cuts to ensure high purity. To reject non-interacting beam particles, a cut on the incident track slope in the upstream drift chambers (SdcIn) was applied: incident tracks with $-0.25 < dx/dz < 0.1$ were excluded. Particle identification was performed using the time-of-flight (TOF) measured between the BH2 and TOF counters. A selection window of $16.0 < \mathrm{TOF} < 17.5$ ns was applied, which effectively separates protons from faster pions and kaons. Furthermore, consistent hit information in the water Cherenkov (WC) detector was required to further suppress background. This selection resulted in a proton sample purity of approximately 97.8%. The detail is explained in Ref. [72].

To ensure high track quality, a threshold of reduced chi-square, $\chi^2 < 40$, was applied to the reconstructed tracks. Under these conditions, the average reconstruction efficiency was determined to be approximately $91.75 \pm 0.55\%$ (stat.). The efficiency was also evaluated as a function of the incident angle, $\theta_p^{\mathrm{SDCIn}}$, and was found to remain above 90% over the full TOF acceptance coverage.

4.7.3 Proton Identification

The mass of the scattered particle was determined using the reconstructed momentum and time-of-flight (TOF) between BH2 and TOF. The squared mass was calculated as

$$M^2 = p^2 \left(\frac{1}{\beta^2} - 1 \right), \quad \text{where } \beta = \frac{L}{Tc}.$$

Here, L is the flight length, T is the measured time-of-flight, and c is the speed of light. A correction of $T_{\mathrm{beam}} = 2.0378\,\mathrm{ns}$ was applied to account for the beam flight time from BH2 to the target, assuming a 1.8 GeV/c beam momentum.

Candidate protons were selected within the squared-mass window, based on the (p, M^2) distribution shown in Fig. 4.10.

The mass resolution σ_{M^2} was parameterized as a function of momentum:

$$\sigma_{M^2}^2 = 4m^4 \left(1 + \frac{m^2}{p^2} \right) a_1^2 + 4m^4 p^2 a_2^2 + 4p^2(p^2 + m^2)\frac{c^2}{L^2} a_3^2,$$

where a_1, a_2, and a_3 represent the timing, momentum, and path-length uncertainties, respectively.

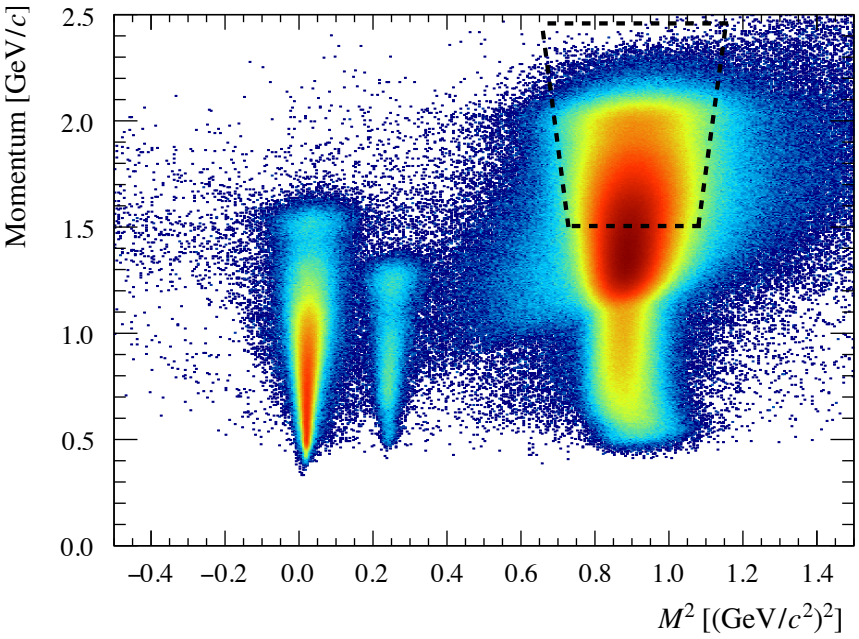

Figure 4.10: Correlation between M^2 and momentum measured with Kurama spectrometer. Selection region is shown in black dashed line.

4.7.4 HypTPC Tagging Efficiency for the (K^-, p) Reaction

To quantify the proton detection performance of the HypTPC, the tagging efficiency for the (K^-, p) reaction was evaluated.

As described in the previous section, the events were categorized based on the number of proton track candidates found in the HypTPC (N_p). If one or more proton candidates were found ($N_p \geq 1$), the event was classified as a tagged event. If no proton candidate was found ($N_p = 0$), the event was classified as an untagged event. The latter category ($N_p = 0$) consists of two contributions: (1) genuine (K^-, p) signal events where the proton track was not reconstructed due to detector inefficiency, and (2) background events where no proton track originating from the target is expected.

Figure 4.11 shows the reconstructed vertex Z distributions for the angular bins of $2^\circ < \theta_{K^-,p} < 4^\circ$ and $4^\circ < \theta_{K^-,p} < 6^\circ$ as typical examples. The black, red, and blue lines correspond to all events, events with $N_p = 1$ (tagged), and events with $N_p = 0$ (untagged), respectively. A distinct peak at the target position ($Z \approx 0$ mm) is observed in the $N_p = 1$ distribution, indicating successful reconstruction. A small signal

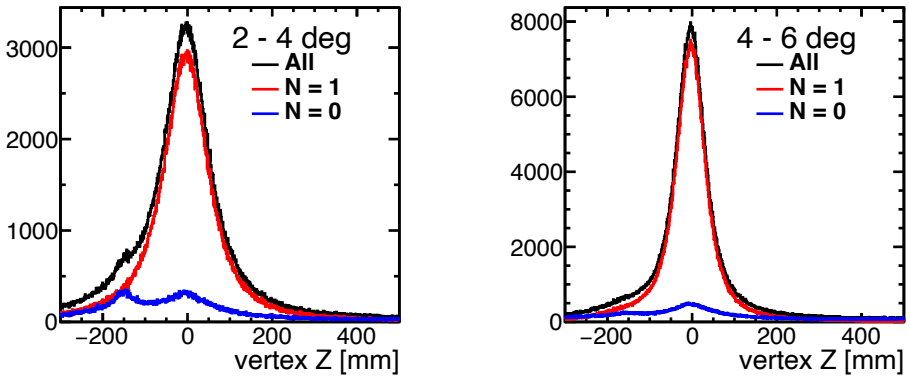

Figure 4.11: Reconstructed vertex Z distributions for (K^-, p) events in the scattering angle ranges of 2°–4° (left) and 4°–6° (right). The black lines represent all events, while the red and blue lines correspond to events with one proton candidate ($N_p = 1$) and no proton candidate ($N_p = 0$), respectively.

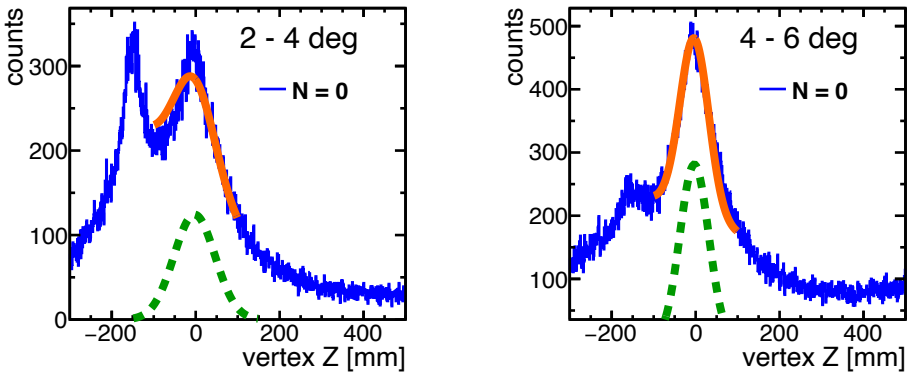

Figure 4.12: Template fitting results of vertex Z distributions for untagged events ($N_p = 0$) in the scattering angle ranges of 2°–4° (left) and 4°–6° (right). The blue histograms represent the experimental data. The green dashed lines indicate the signal component modeled by the resolution function, and the orange solid lines show the total fit result including the linear background.

component is also visible in the $N_p = 0$ distribution at the same position, corresponding to the inefficient events.

To quantitatively estimate the number of these inefficient events, a template fit was performed on the Z distribution of the $N_p = 0$ sample. The signal component was described by the measured resolution function defined in Eq. **??**. The background component was modeled as a first-order polynomial in the Z direction locally around the target region. The fitting was performed in scattering angle bins of 2° width.

The results of the template fitting for these angular bins are displayed in Fig. 4.12. The blue histograms show the experimental data for the $N_p = 0$ category. The green dashed lines represent the extracted signal component (inefficient events), and the orange solid lines indicate the total fit result (signal + background). Based on the integral of the signal components in the $N_p = 1$ and $N_p = 0$ distributions, the HypTPC tagging efficiency was calculated.

The tagging efficiency, denoted as $\varepsilon_{\text{HypTPC-Tagging}}$, was calculated as the ratio of the number of tagged events ($N_p \geq 1$) to the estimated total number of genuine (K^-, p) events (the sum of tagged events and the signal component of untagged events). For the diamond target, the efficiency was found to range from 93.30% to 95.14% depending on the kinematic region. For the CH_2 target, the efficiency was estimated to be $95.14 \pm 0.04\%$. These high efficiency values demonstrate the reliable proton detection capability of the HypTPC for the (K^-, p) reaction analysis.

4.7.5 Total Proton Efficiency

The total proton tracking efficiency, denoted as ε_p, was obtained by combining the efficiency factors from the individual detector components. The total efficiency is defined as the product of the following four factors:

$$\varepsilon_p = \varepsilon_{\text{SdcIn}} \times \varepsilon_{\text{SdcOut}} \times \varepsilon_{\text{KURAMA}} \times \varepsilon_{\text{HypTPC-Tagging}} \tag{4.13}$$

where each factor is defined as follows:

- $\varepsilon_{\text{SdcIn}}$: The local tracking efficiency of the upstream drift chambers, SDC1 and SDC2.
- $\varepsilon_{\text{SdcOut}}$: The local tracking efficiency of the downstream drift chambers, SDC3

and SDC4.

- $\varepsilon_{\mathrm{KURAMA}}$: The track reconstruction efficiency of the KURAMA spectrometer.
- $\varepsilon_{\mathrm{HypTPC\text{-}Tagging}}$: The tagging efficiency of the HypTPC, as evaluated in the previous section.

Table 4.3 summarizes the efficiencies evaluated for both the CH_2 and diamond target data. The local tracking efficiencies for the drift chambers ($\varepsilon_{\mathrm{SdcIn}}$ and $\varepsilon_{\mathrm{SdcOut}}$) were found to be high, exceeding 99% for most cases. The KURAMA tracking efficiency ($\varepsilon_{\mathrm{KURAMA}}$) was approximately 91–93%.

Reaction loss due to hadronic interactions inside the 20-mm thick diamond target was evaluated using the material's nuclear interaction length. The calculation indicates that approximately 7.3% of the protons are lost before exiting the target volume. This effect was accounted for by applying a correction to the total efficiency.

By combining these factors with the HypTPC tagging efficiency, the total proton tracking efficiency ε_p was determined. For the CH_2 target, the total efficiency was estimated to be $87.5 \pm 0.8\%$. For the diamond target, the efficiency ranges from 84.2% to 87.1%, depending on the kinematic conditions.

Table 4.3: Comparison of proton tracking efficiencies between CH_2 and diamond targets. The quoted values include combined statistical and systematic uncertainties (in %).

Efficiency Factor	**CH_2 [%]**	**Diamond [%]**
$\varepsilon_{\mathrm{SdcIn}}$	99.87 ± 0.02	99.81–99.89
$\varepsilon_{\mathrm{SdcOut}}$	98.87 ± 0.17	99.07–99.33
$\varepsilon_{\mathrm{KURAMA}}$	93.22 ± 0.42	91.20–92.30
$\varepsilon_{\mathrm{HypTPC\text{-}Tagging}}$	95.14 ± 0.04	93.30–95.14
ε_p	$\mathbf{87.5 \pm 0.8}$	**84.2–87.1**

4.7.6 Proton Acceptance of KURAMA Spectrometer

The acceptance of the KURAMA spectrometer for scattered protons was evaluated using a dedicated Monte Carlo simulation incorporating the full detector geometry and trigger configuration of the J-PARC E42 experimental setup. The simulation included realistic materials, magnetic field maps, and trigger conditions based on hit information from the SCH, TOF, and BVH detectors.

Scattered protons were uniformly generated within the momentum range of 0.3 − 2.5 GeV/c and the angular range of 0° − 30°, assuming isotropic emission in both the polar angle θ and the azimuthal angle ϕ. Each simulated event was tracked through the full detector system, and the detection and reconstruction conditions applied in the real analysis were imposed to estimate the effective acceptance.

The resulting acceptance was obtained as a function of scattering angle and momentum, after averaging over the azimuthal angle ϕ. The acceptance map is shown in Figure 4.13, which serves as a correction factor for the measured (K^-, p) yield in the differential cross-section analysis.

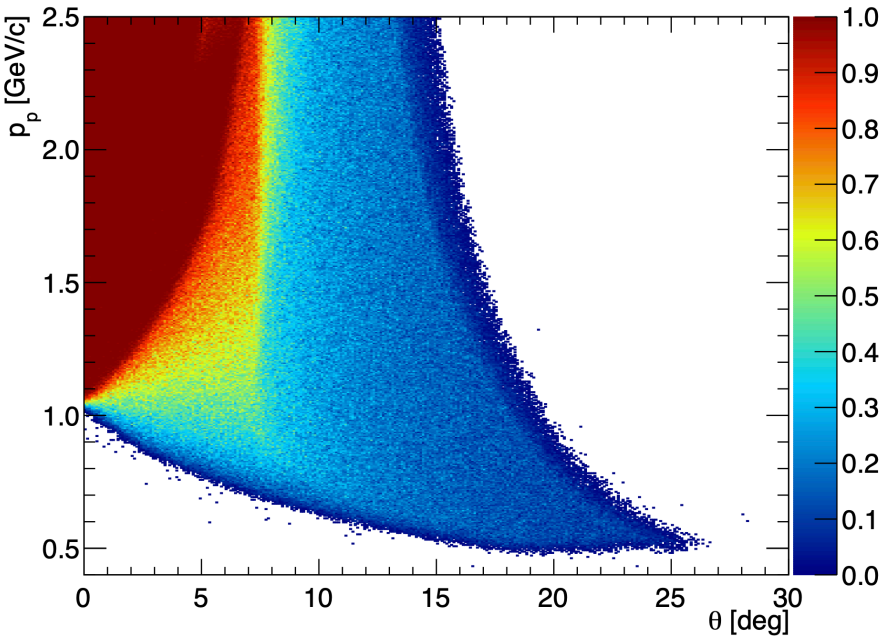

Figure 4.13: Acceptance of the KURAMA spectrometer for protons as a function of scattered angle and momentum

4.8 (K^-, p) Analysis

4.8.1 Event Selection and Reaction Reconstruction

The final physics analysis integrates the tracking information from the K1.8 beam line, the Kurama spectrometer, and the TPC to reconstruct the (K^-, p) reaction events. The event selection procedure aims to identify minimal (K^-, p) scattering candidates

using beam K^- and TPC-Kurama tracks.

Pre-selection

Events are selected based on the following criteria:

- **Track Multiplicity**: Exactly one good track is required in the K1.8 beam spectrometer. For the scattered particle, exactly one "TPC-Kurama track"—a track reconstructed by the Kurama spectrometer and successfully matched with TPC tracking—is required.
- **Tracking Quality**:
  - K^- Beam: $\chi^2 < 30$.
  - TPC-Kurama Track (p): $\chi^2 < 30$.
- **Particle Identification**:
  - **Beam** K^-: Identified by upstream detectors in the K1.8 beamline analysis as described in Sec. 4.2.
  - **Scattered** p: Identified using the momentum, the reconstructed mass-squared (m^2), and, charge from the TPC-Kurama track with $N\sigma$ cut (3σ) based on the momentum-dependent mass resolution as shown in Sec. 4.7.3.
- **Scattering Angle Selection**: Cut region of the angle between K^- and proton in the laboratory frame is $3.5° < \theta_{K^-p} < 4.5°$ as explained in Sec. 4.8.2.

4.8.2 Scattering Angle

The scattering angle, θ_{K^-p}, is defined as the angle between the momentum vector of the incident K^- and that of the scattered proton in the laboratory frame. This angle is a fundamental kinematic variable of the (K^-, p) reaction.

Figure 4.14 shows the distribution of the reconstructed scattering angle for all (K^-, p) candidate events. The shape of this distribution is determined by a combination of the reaction dynamics and the geometrical acceptance of the KURAMA spectrometer, as discussed in Section 3.8.6. For the subsequent analysis, particularly the

calculation of the inclusive cross-section, a specific angular range is selected. This selection is crucial for comparing the experimental results with theoretical calculations. The region around four degrees is particularly important because contributions from higher partial waves are suppressed, which simplifies the theoretical interpretation. Therefore, we apply a selection of $3.5° < \theta_{K^-p} < 4.5°$ for the primary analysis in this study. This angular cut is also consistent with that used in the previous J-PARC E05 experiment, facilitating a direct comparison.

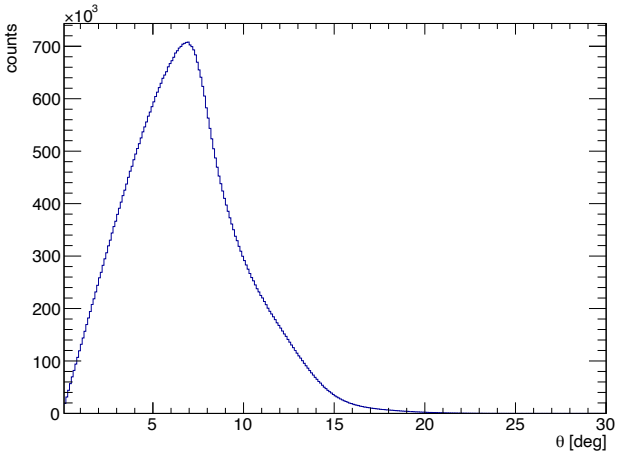

Figure 4.14: Distribution of the reconstructed (K^-, p) scattering angle in the laboratory frame. The region between 3.5° and 4.5° (indicated by arrows or a shaded area) is selected for the inclusive cross-section analysis.

Vertex Reconstruction

The reaction vertex is reconstructed as the closest point of approach between the incoming K^- beam track (extrapolated from K1.8) and the scattered TPC-Kurama track (extrapolated from Kurama and TPC).

- **Target Region Cut**: The reconstructed vertex (x, y, z) is required to be within the target volume.
  - $|x| < 15$ mm
  - $|y| < 15$ mm
  - $|z| < 70$ mm (from target center)

– Closest distance between tracks < 30 mm.

Further explanation about vertex reconstruction is in Sec. 4.8.5.

Kinematic Reconstruction

For the selected (K^-, p) events, the missing mass spectrum is calculated.

- **Momentum Correction**: The momenta of TPC-Kurama tracks are corrected for:
  - Angular dependence (polynomial correction based on horizontal/vertical angles). (For the detail, see Sec. 4.8.4)
  - Momentum scaling (correction based on quadratic scaling function). (For the detail, see Sec. 4.8.4)
  - Energy loss in the target and detector materials (calculated using Bethe-Bloch formula for specific path lengths).

Finally, the missing mass analysis of the $^{12}\mathrm{C}(K^-, p)$ reaction is performed for the events satisfying all the selection criteria described above.

4.8.3 Missing Mass Reconstruction

The missing mass M_X of the $^{12}\mathrm{C}(K^-, p)X$ reaction is calculated from the corrected four-momenta of the beam (P_{K^-}), target ($P_{^{12}\mathrm{C}}$), and scattered proton (P_p) as:

$$M_X = \sqrt{(P_{K^-} + P_{^{12}\mathrm{C}} - P_p)^2}. \tag{4.14}$$

To discuss the physics of the kaonic nucleus, it is convenient to define the K^- binding energy, B_K, with respect to the $^{11}\mathrm{B} + K^-$ threshold. The binding energy is defined as:

$$B_K = M_{^{11}\mathrm{B}} + M_{K^-} - M_X, \tag{4.15}$$

where $M_{^{11}\mathrm{B}}$ is the ground state mass of the recoil ^{11}B nucleus, and M_{K^-} is the K^- mass. In the final spectrum, we adopt $-B_K$ as the horizontal axis. This definition provides an intuitive representation where the bound region corresponds to negative values ($-B_K < 0$) and the unbound region corresponds to positive values ($-B_K > 0$).

4.8.4 Momentum Correction

The momenta of particles scattered into the KURAMA spectrometer were initially reconstructed based on the calculated magnetic field map. However, discrepancies between the modeled and actual magnetic field distributions led to systematic deviations in the reconstructed momenta. To mitigate these effects, a two-step correction procedure—accounting for angular dependencies and absolute momentum nonlinearities—was implemented.

Angular Dependence Correction

Systematic biases were evaluated using three kinematic reference channels: Ξ^- and $\Xi(1530)^-$ production via the (K^-, K^+) reaction, and K^-p elastic scattering. Since the missing mass of these states is independent of the laboratory emission angle, any correlation between the reconstructed momentum and the track angles indicates a systematic bias. Significant dependencies were observed with respect to the horizontal ($u = dx/dz$) and vertical ($v = dy/dz$) angles at the spectrometer entrance.

To eliminate these geometrical biases, correction functions were modeled using polynomial fits to the momentum residuals. A third-order polynomial was applied for the horizontal angle, and a fourth-order polynomial for the vertical angle:

$$f(u) = p_0 + p_1 u + p_2 u^2 + p_3 u^3, \tag{4.16}$$

$$g(v) = q_0 + q_1 v + q_2 v^2 + q_3 v^3 + q_4 v^4, \tag{4.17}$$

$$p_{\mathrm{ang}}^{\mathrm{corr}} = p^{\mathrm{meas}} - f(u) - g(v), \tag{4.18}$$

where p^{meas} denotes the initially reconstructed momentum, and p_i, q_i are coefficients determined from the experimental data. This correction effectively suppressed the observed angular correlations.

Absolute Momentum Correction

Following the angular correction, a residual nonlinearity dependent on the absolute momentum magnitude was identified. The momentum residuals, defined as $\Delta p = p^{\mathrm{meas}} - p^{\mathrm{calc}}$, were analyzed across three momentum regions covered by the calibration

reactions: ~ 0.9 GeV/c ($\Xi(1530)^-$), ~ 1.3 GeV/c (Ξ^-), and ~ 2.0 GeV/c (K^-p elastic).

The difference between the angle-corrected momentum (p^{meas}) and the kinematically calculated momentum (p^{calc}) was modeled as a quadratic function:

$$\Delta p = p^{\mathrm{meas}} - p^{\mathrm{calc}} = a_0 + (a_1 - 1)p^{\mathrm{calc}} + a_2(p^{\mathrm{calc}})^2, \tag{4.19}$$

where a_0, a_1, and a_2 are fitting parameters. To obtain the final corrected momentum p^{corr} corresponding to the true value (p^{calc}), the quadratic equation was solved as follows:

$$p^{\mathrm{corr}} = \frac{-a_1 + \sqrt{a_1^2 + 4a_2(p^{\mathrm{meas}} - a_0)}}{2a_2}. \tag{4.20}$$

Validation and Resolution

The validity of the momentum calibration was verified using missing mass spectroscopy. For the reconstruction of the proton mass via the (K^-, p) elastic scattering channel, the background contribution from carbon was subtracted from the inclusive polyethylene (CH_2) spectrum. The carbon spectrum was scaled appropriately by considering the effective number of the target nuclei to isolate the hydrogen contribution. The resulting difference spectrum was fitted with a Gaussian function combined with a first-order polynomial background. The spectrum exhibited peak consistent with the nominal PDG masses for the kaon where the mean value is 488 MeV/c^2 as the result of fitting. The resulting mass resolution (σ) for the kaon was evaluated to be 35.0 MeV/c^2 (corresponding to a FWHM value of 82.4 MeV/c^2), as illustrated in Fig. 4.15.

4.8.5 Reaction Vertex Reconstruction

The interaction vertex is defined as the midpoint of the segment connecting the points of closest approach between the incident K^- beam and the scattered proton (p) tracks. These tracks are reconstructed following the procedures detailed in Sec. 4.8.1. The optimal vertex position was determined using a two-step iterative search algorithm. Initially, a coarse scan was performed along the beam axis (z-axis) over a range of 1 mm with a step size of 1 mm to locate the approximate minimum of the closest approach distance. Subsequently, a fine search with a precision of 0.01 mm was conducted around the local minimum to pinpoint the precise vertex coordinates.

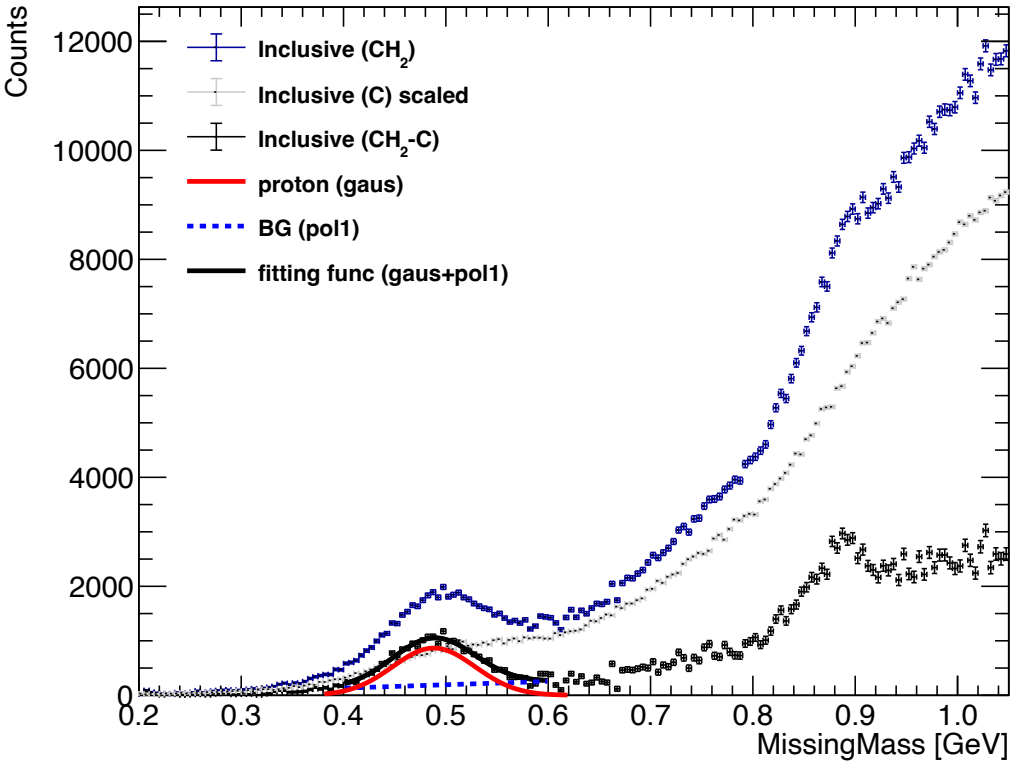

Figure 4.15: Missing mass spectrum of the (K^-, p) reaction. The black points represent the inclusive data from the CH_2 target after subtracting the scaled carbon contribution. The spectrum is fitted with a Gaussian function for the proton peak (red solid line) and a first-order polynomial for the background (blue dashed line). The black solid line indicates the total fit function.

Energy loss corrections were applied to both the incoming K^- and the outgoing proton trajectories. Based on the reconstructed vertex position, the path lengths traversed within the target material were calculated. The energy loss was then estimated using the Bethe–Bloch formula, and the corrected momenta were utilized in the subsequent kinematic analysis.

In the preliminary stage of event selection, the vertex was reconstructed relying solely on the proton track detected by the KURAMA spectrometer, without mandating a tag in the HypTPC. To retain genuine reaction events while minimizing selection bias, a broad spatial gate was applied: the vertex position was required to be within ±50 mm in x, ±40 mm in y, and ±400 mm in z. Additionally, the distance of closest approach between the two tracks was required to be less than 100 mm. This preselection window is significantly wider than the physical dimensions of the target, even when accounting for tracking resolution.

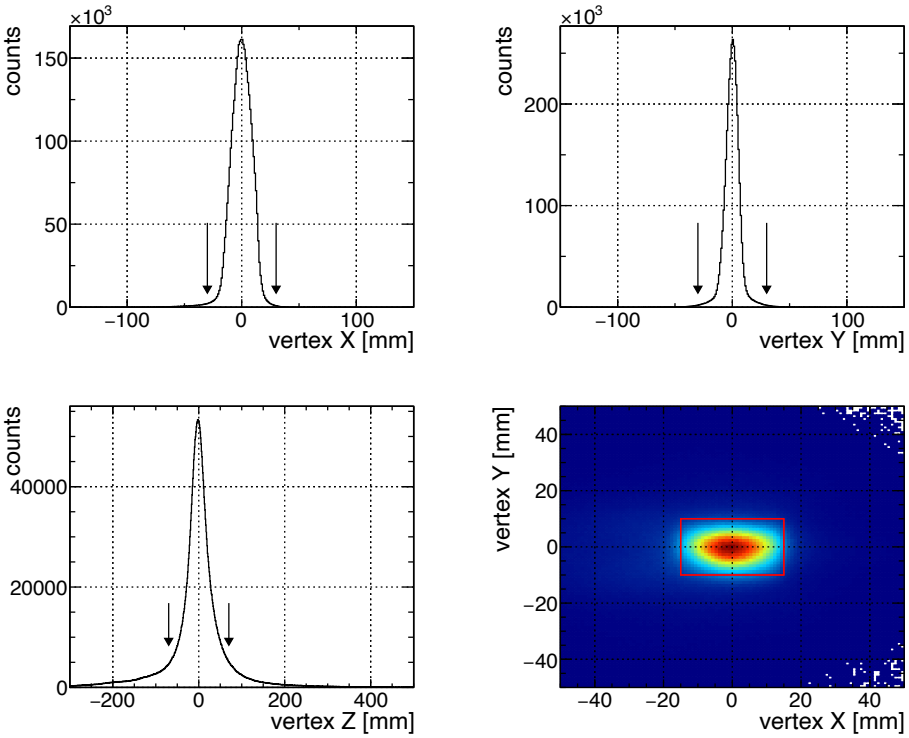

Figure 4.16: Reconstructed vertex distributions for (K^-, p) events. The 1D histograms show the distributions in x, y, and z coordinates. The arrows indicate the cut positions applied to select events within the target region. The bottom-right plot shows the correlation between x and y vertex positions, with the red box indicating the volume cut.

Events surviving this preselection were subjected to a secondary reconstruction phase using the TPC-KURAMA tracking algorithm, which integrates proton track information from the HypTPC. In this step, the vertex was re-evaluated, and a stricter longitudinal cut of $|z| < 70$ mm was imposed to further reject background events originating outside the target region.

The resulting vertex distributions are displayed in Fig. 4.16. The arrows in the one-dimensional histograms and the red box in the two-dimensional plot indicate the strict vertex selection gates applied for the analysis. The vertex position was required to be within $|x| \leq 15$ mm, $|y| \leq 15$ mm, and $|z| \leq 70$ mm from the target center.

The performance of the vertex reconstruction was evaluated by analyzing the vertex Z distributions categorized by the scattering angle $\theta_{K^-,p}$. Since the vertex position is determined by the intersection of two tracks, the longitudinal resolution (σ_z) is geometrically sensitive to the opening angle between the incident K^- and the scattered proton. At forward angles, where the two tracks are nearly parallel, the intersection point becomes less constrained along the beam axis, resulting in a broader distribution.

Figure 4.17 shows the vertex Z distributions for various angular bins. Each distribution was fitted with a Gaussian function to estimate the resolution σ_z. The resulting σ_z values and the selection efficiency for the $|z| \leq 70$ mm cut are summarized in Fig. 4.18. As expected, the resolution improves significantly as the scattering angle increases, decreasing from ~ 90 mm at the most forward angles to ~ 10 mm at larger angles. Consequently, the coverage of the $|z| \leq 70$ mm cut, defined as the ratio of the Gaussian integral within the cut range to the total integral, increases from $\sim 45\%$ at 0° to $> 95\%$ for angles larger than 10°. Despite the lower resolution at very forward angles, this cut was chosen to maintain a high signal-to-noise ratio by rejecting background events originating outside the target.

Finally, the global vertex selection efficiency, denoted as $\varepsilon_{\mathrm{vertex}}$, was evaluated by integrating over the experimental acceptance. This efficiency represents the fraction of genuine (K^-, p) events retained after applying the spatial gates, specifically the longitudinal cut of $|z| \leq 70$ mm. For the CH_2 target, the efficiency was determined to be $75.20 \pm 0.02\%$. For the diamond target, the efficiency ranges from 71.36% to 75.28% depending on the kinematic conditions. These values are consistent with the angular dependence shown in Fig. 4.18, where the integrated efficiency is dominated by the

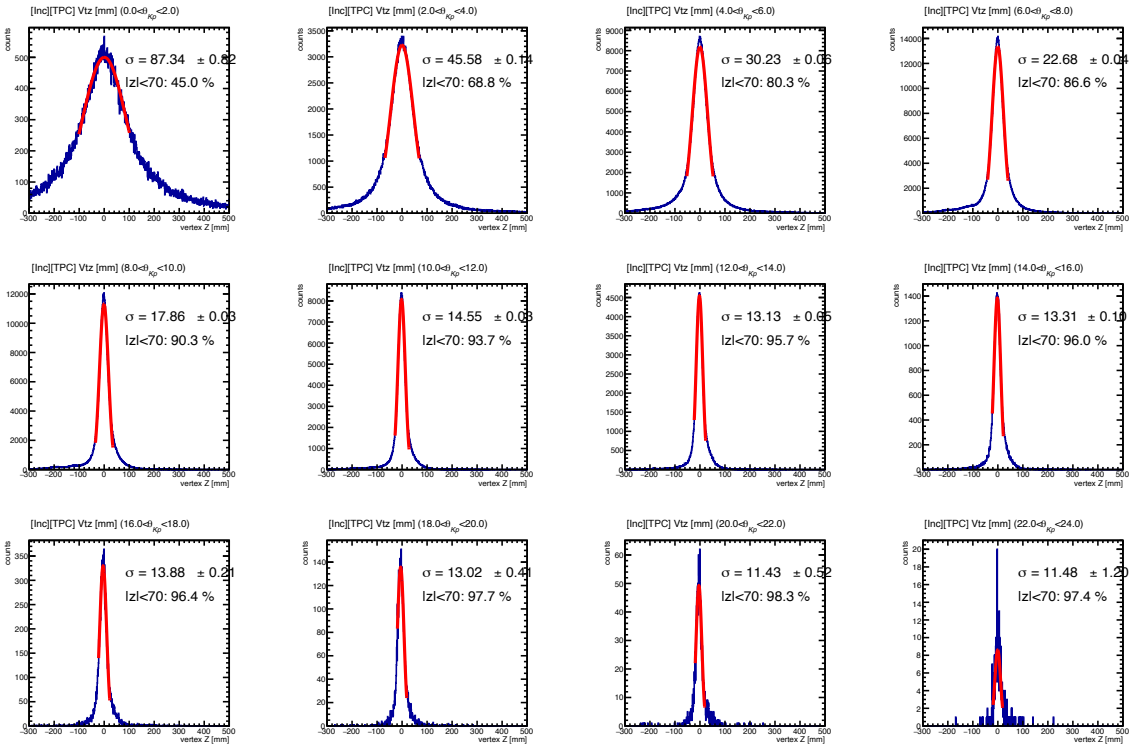

Figure 4.17: Reconstructed vertex Z distributions for inclusive (K^-, p) events categorized by the scattering angle $\theta_{K^-,p}$. The red curves indicate the Gaussian fits applied to the peaks. The estimated resolution (σ) and the fraction of events within $|z| < 70$ mm are indicated in each panel.

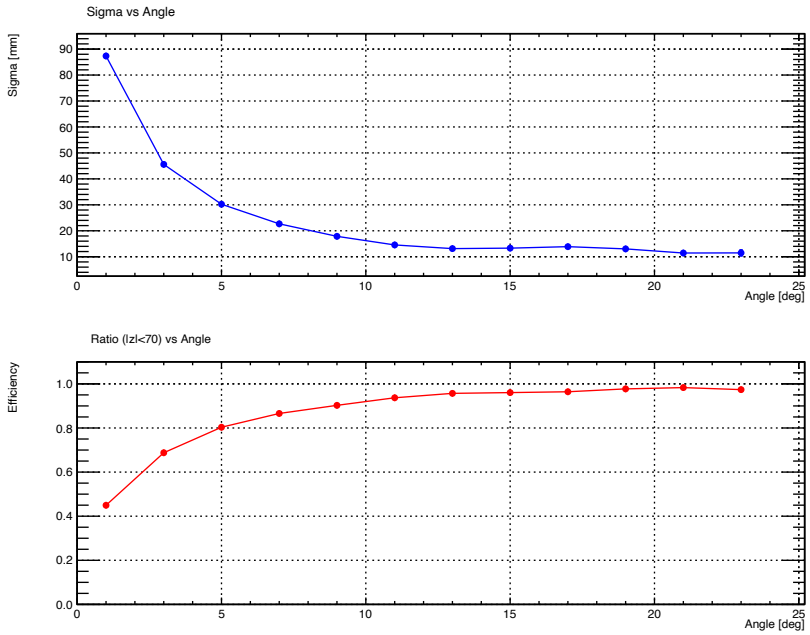

Figure 4.18: Angular dependence of the vertex reconstruction performance. (Top) The vertex Z resolution (σ) as a function of the scattering angle. (Bottom) The efficiency of the vertex selection cut ($|z| \leq 70$ mm) as a function of the scattering angle, calculated based on the Gaussian fits.

contribution from forward scattering angles where the vertex resolution is limited.

4.8.6 Summary of Efficiency for (K^-, p) Reaction

The overall efficiency for identifying a (K^-, p) reaction event is determined by the product of the individual tracking efficiencies for the incident K^- and the outgoing proton. This combined efficiency, $\varepsilon_{(K^-,p)}$, is a crucial normalization factor for the cross-section calculation presented in Section 4.10. It is defined as:

$$\varepsilon_{(K^-,p)} = \varepsilon_{K^-} \cdot \varepsilon_p \cdot \varepsilon_{\text{vertex}} \cdot \varepsilon_{\text{daq}}, \tag{4.21}$$

where ε_{K^-} is the total K^- beam tracking efficiency (Section 4.2) and ε_p is the total proton tracking efficiency (Section 4.3).

The values for these efficiencies, derived in the preceding sections, are summarized in Table 4.4. For the diamond target runs, the combined efficiency for the (K^-, p) reaction ranged from 63.0% to 67.5%, reflecting the run-by-run variations in beam and detector conditions. For the CH_2 target runs, a representative total efficiency was

determined to be $64.8 \pm 2.0\%$. This comprehensive efficiency evaluation ensures the accurate normalization of the measured event yields.

Table 4.4: Summary of the combined tracking efficiency for the (K^-, p) reaction.

Efficiency Factor	**CH_2 Target [%]**	**Diamond Target [%]**
Incident K^- Efficiency (ε_{K^-})		
$\varepsilon_{\mathrm{BH1\&BH2}}$	97.42 ± 0.10	95.39–97.45
$\varepsilon_{\mathrm{BTOF}}$	99.99 ± 0.01	99.99 ± 0.01
$\varepsilon_{\mathrm{BFT}}^{\mathrm{single}}$	97.83 ± 0.10	97.65–98.19
$\varepsilon_{\mathrm{K1.8}}^{\mathrm{single}}$	96.61 ± 0.10	95.30–97.59
$\varepsilon_{K^-\text{-survival}}$	95.77 ± 0.01	95.77 ± 0.01
$\varepsilon_{\mathrm{target}}$	88.00 ± 2.51	89.35 ± 1.35
Total K^- efficiency (ε_{K^-})	**77.6 ±2.2**	**76.0–79.9**
Scattered Proton Efficiency (ε_p)		
$\varepsilon_{\mathrm{SdcIn}}$	99.87 ± 0.02	99.81–99.89
$\varepsilon_{\mathrm{SdcOut}}$	98.87 ± 0.17	99.07–99.33
$\varepsilon_{\mathrm{KURAMA}}$	93.22 ± 0.42	91.20–92.30
$\varepsilon_{\mathrm{HypTPC-Tagging}}$	95.14 ± 0.04	93.30–95.14
Total KURAMA efficiency (ε_p)	**87.5 ±0.8**	**84.2–87.1**
Other Efficiency Factors		
$\varepsilon_{\mathrm{vertex}}$	75.20 ± 0.02	71.36–75.28
$\varepsilon_{\mathrm{DAQ}}$	94.0–96.0	88.0–96.0
Total	**71.4 ±0.5**	**62.7–72.2**
Total (K^-, p) efficiency ($\varepsilon_{(K^-,p)}$)	76.0 ± 0.4	40.1–50.24

4.9 Inclusive Spectrum for $^{12}\mathrm{C}(K^-, p)$ Reaction

For the physics discussion related to the kaonic nuclear state, we construct the binding energy spectrum of the K^- in the $^{12}\mathrm{C}(K^-, p)$ reaction. This spectrum is derived from the missing mass technique, utilizing the precise particle identification and momentum information obtained from the beamline and KURAMA spectrometers, as well as the high-resolution tracking from the HypTPC, as shown in the sections above.

4.9.1 Inclusive Spectrum

We define the inclusive spectrum for the $^{12}\mathrm{C}(K^-, p)$ reaction as the spectrum constructed without requiring the detection of any additional particles in the HypTPC

other than the outgoing proton used for the missing mass calculation. Figure 4.19 shows the obtained count-based inclusive spectrum plotted against the negative binding energy, $-B_K$. This spectrum represents the baseline for subsequent analyses where specific process like escape K^- of event of interest are selected using HypTPC data. The evaluation of differential cross-sections will be presented in the chapter 7.2.

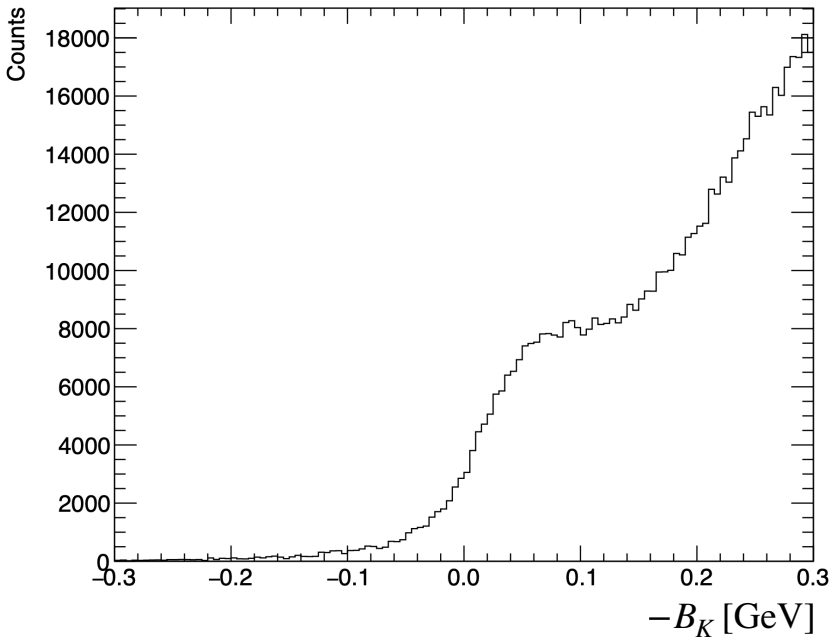

Figure 4.19: Count-based inclusive spectrum of the $^{12}\mathrm{C}(K^-, p)$ reaction plotted as a function of negative binding energy, $-B_K$. The region $-B_K < 0$ corresponds to the bound region, and $-B_K > 0$ corresponds to the unbound region.

4.10 Inclusive Cross Section for $^{12}\mathrm{C}(K^-, p)$ Reaction

4.10.1 Definition

First, we establish the reliability of the current analysis by examining the inclusive (K^-, p) spectrum. The double differential cross-section was calculated using the following formula:

$$\left\langle \frac{d^2\sigma}{d\Omega dE} \right\rangle_{\mathrm{inc}} = \frac{A}{N_A \rho x} \cdot \frac{N_{K^- p}}{N_{\mathrm{beam}} \Delta\Omega_{\theta_1 - \theta_2} \Delta E \varepsilon}, \tag{4.22}$$

where A is the atomic mass number of the target, N_A is Avogadro's number, ρ is the area density of the target, and x is the thickness of the target. N_{K^-p} denotes the number of reconstructed (K^-, p) events, and $N_{\rm beam}$ is the total number of incident K^- particles. It should be noted that the energy spectrum is presented as a function of the binding energy (B_K). As described in the previous chapter, this binding energy is calculated from the missing mass of the reaction. ΔE corresponds to the bin width of this binding energy.

$\Delta\Omega_{\theta_1-\theta_2}$ is the effective solid angle as a function of the proton momentum, defined as:

$$\Delta\Omega_{\theta_1-\theta_2} = \int_0^{2\pi}\int_{\theta_{\rm min}}^{\theta_{\rm max}} \varepsilon_{acc}(\theta, p_p)\sin\theta d\theta d\phi, \tag{4.23}$$

where $\varepsilon_{acc}(\theta, p_p)$ represents the proton acceptance of the spectrometer system. In this analysis, the scattering angle range is selected to be $3.5^\circ < \theta < 4.5^\circ$. This angular selection is consistent with the condition used in the past J-PARC E05 experiment.

The overall experimental efficiency ε is defined in Eq. 4.21.

4.10.2 Result

Figure 4.20 shows the obtained inclusive differential cross-section as a function of the binding energy, $-B_K$. The spectrum exhibits a clear quasi-free elastic scattering (QFES) peak in the unbound region ($-B_K > 0$) and a continuum component from inelastic background processes. The prominent peak structure in the unbound region is considered to originate mainly from the quasi-free elastic scattering process ($K^-N \to K^-N$) and the quasi-free charge exchange scattering process ($K^-p \to \bar{K}^0 n$). The continuum component extending further into the unbound region arises from inelastic K^-p reactions, which are primarily background events caused mainly by forward-decaying protons from hyperons produced in the forward direction like $K^-p \to Y\pi \to p_0\pi\pi$ or $K^-p \to Y\pi\pi \to p_0\pi\pi\pi$, where p_0 is denoted as a KURAMA-detected proton.

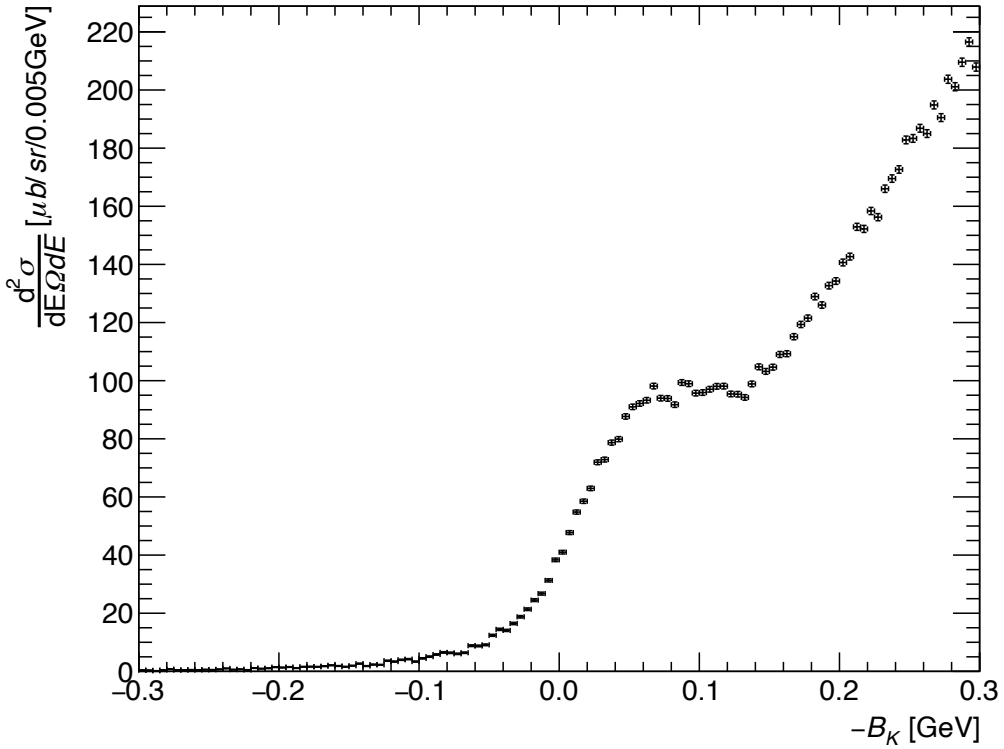

Figure 4.20: Inclusive differential cross-section spectrum of the ^{12}C(K^-, p) reaction (black dots) for the scattering angle range $3.5° < \theta_{lab} < 4.5°$.

Chapter 5

Coincidence Analysis

5.1 Overview

This chapter presents the exclusive analysis of the $^{12}\mathrm{C}(K^-, p)$ reaction, focusing on the measurement of the "escape K^-" channel. This channel corresponds to events where the scattered K^- from the quasi-free elastic process ($K^-N \to K^-N$) exits the nucleus and is detected in the Hyperon Time Projection Chamber (HypTPC). The resulting escape cross-section is a key observable for probing the absorptive nature of the $\bar{K}$-nucleus interaction.

The analysis builds upon the foundational framework established in Chapter 4, which provided the inclusive spectrum and the precise kinematics of the incident K^- and scattered proton. The main objective of this chapter is to isolate the pure escape K^- signal from various backgrounds and to correct for detection efficiencies, ultimately leading to the differential cross-section.

The analysis procedure is structured as shown in Fig. 5.1. First, we detail the particle identification (PID) of the scattered K^- using the combined information of momentum, specific energy loss (dE/dx), and time-of-flight from the HypTPC. The robustness of the PID criteria is validated through a detailed comparison between experimental data and Monte Carlo simulations.

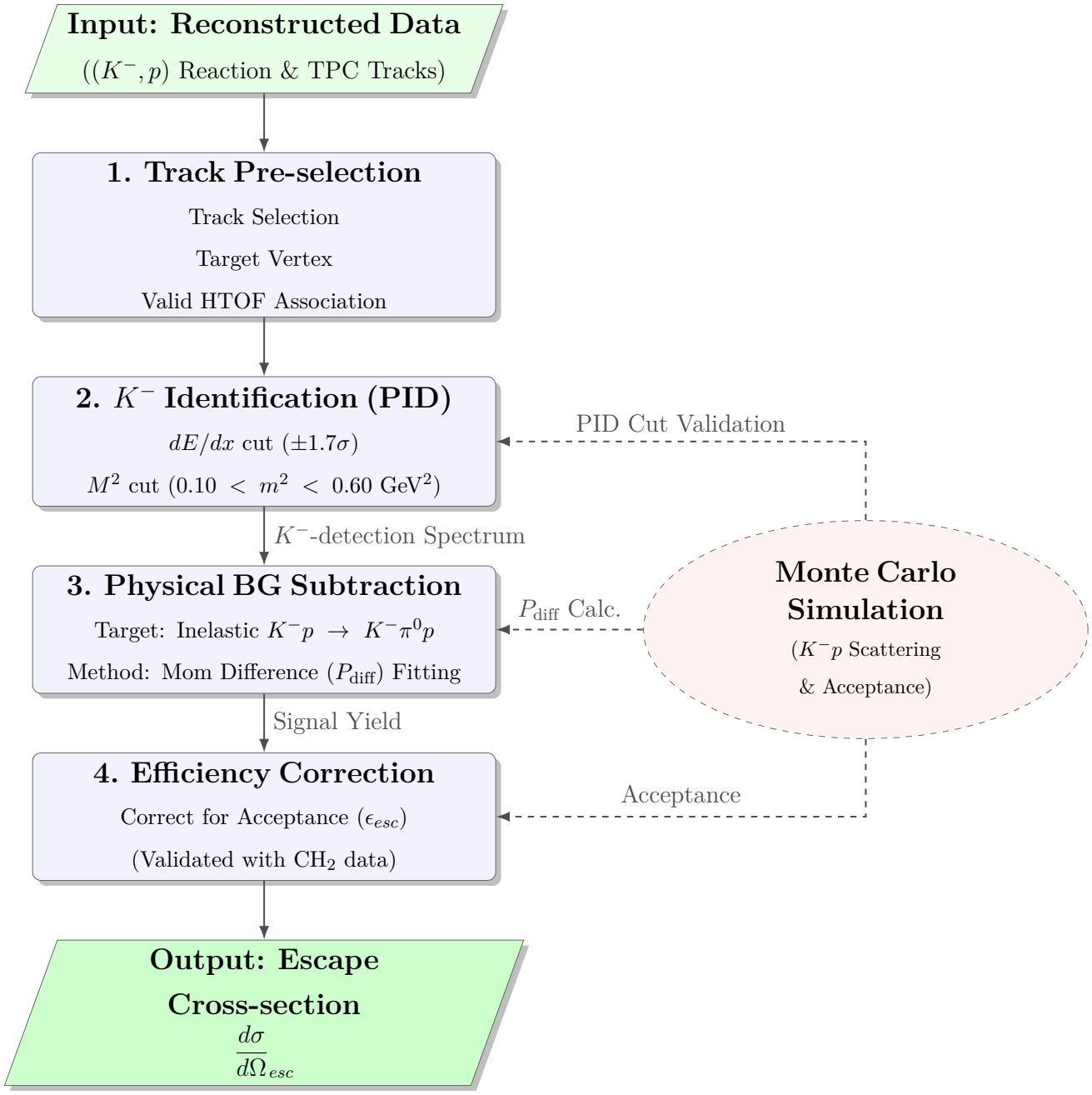

Figure 5.1: Overview of the analysis flow for the escape K^-. The procedure begins with reconstructed data and proceeds through event selection, including particle identification (PID) based on dE/dx and time-of-flight information. Following the subtraction of physical background from inelastic scattering, the yield is corrected for detection efficiency and acceptance to derive the final differential cross section. Monte Carlo simulations are utilized for PID validation, background momentum distribution generation, and acceptance estimation.

Next, we address the subtraction of background contributions. This involves two steps: the removal of non-physical backgrounds estimated from the PID analysis, and

the subtraction of the dominant physical background from the inelastic reaction $K^- p \to K^- \pi^0 p$, which is achieved by utilizing the momentum difference variable (P_{diff}) based on kinematic distinctions.

A crucial part of this chapter is the evaluation of the TPC acceptance for the escape K^-. We describe the comprehensive Monte Carlo simulation used to estimate the detection efficiency, and validate its reliability by comparing the simulation results for a proton target with experimental data from a polyethylene (CH_2) target.

Finally, after discussing the systematic uncertainties, we present the background-subtracted and efficiency-corrected differential cross-section for the escape K^- process. This result will be used in Chapter 6 to derive the quantitative constraints on the imaginary part of the $\bar{K}$-nucleus optical potential.

5.2 Escape K^- Spectrum

This section details the construction of the "escape K^- spectrum" by isolating events where the scattered K^- is explicitly detected in the HypTPC. This specific channel corresponds to K^- that have undergone quasi-free elastic scattering ($K^- N \to K^- N$) inside the nucleus and escaped the nucleus without absorption. The following subsections describe the particle identification criteria and the validation of the signal selection.

5.2.1 Selection of Scattered K^-

The selection of scattered K^- candidates is a critical step to isolate the signal from a large background of other charged particles, primarily π^-. This is achieved through a multi-step particle identification (PID) procedure that combines information from the HypTPC and the surrounding hodoscope counters (HTOF). The procedure involves sequential cuts to ensure tracks originate from the target, have a valid time-of-flight (TOF) measurement, and are consistent with the mass and energy loss of a kaon. The tracks considered for this selection are those not identified as the incident beam (`K18Track`) or the scattered proton (`KuramaTrack`), as described in Sec. 4.6 of Chap. 4.

Track Pre-selection: Target and HTOF Association

First, to ensure that reconstructed tracks originate from the (K^-, p) reaction vertex, a geometric association with the target is performed. Each HypTPC track is extrapolated backwards to the z-position of the target center. A track is accepted as a signal candidate only if its extrapolated position lies within a fiducial volume defined by a radial cut of $r < 50\,\text{mm}$ from the target center.

Next, a precise TOF measurement requires a correct association between the HypTPC track and a hit in the HTOF wall. Each TPC track is extrapolated outwards to the HTOF geometry. A track is considered successfully associated if its extrapolated position matches an active HTOF segment within a window of $|y_{ext} - y_{meas}| < 100\,\text{mm}$. Only tracks with a valid HTOF association are used for the subsequent PID steps.

Kaon Identification with dE/dx and TOF

The core of the PID relies on two key observables: the specific energy loss ($\langle dE/dx \rangle$) and the squared mass (m^2) derived from TOF.

The $\langle dE/dx \rangle$ in the TPC gas is a function of the particle's velocity, allowing for mass separation at a given momentum, as described by the Bethe formula. Figure 5.2 shows this correlation for negatively charged particles. To minimize fluctuations from the Landau distribution, $\langle dE/dx \rangle$ is calculated as the truncated mean of the lowest 80% of charge clusters on a track. A clear separation between the kaon and pion bands is observed. To select K^- candidates, we define a selection window based on the resolution of the $\langle dE/dx \rangle$ measurement (σ_K). Tracks falling within a band of $\pm 1.7\sigma_K$ around the theoretical K^- expectation are selected, as indicated by the dashed lines in the figure.

Particle identification is further enhanced using TOF information. Figure 5.3 shows the correlation between the inverse velocity $1/\beta$ (calculated from TOF and track length) and momentum. The separation between pions, kaons, and protons is clearly visible.

To apply a quantitative cut, the squared mass (M^2) is calculated from momentum and β. Figure 5.4 displays the M^2 distributions for negative tracks selected with different $\langle dE/dx \rangle$ cut widths: 1.0σ (blue), 1.7σ (red), and 3.0σ (green). The distributions show a K^- peak around 0.24 $(\text{GeV}/c^2)^2$. A selection window of $0.10 < M^2 < 0.60$ $(\text{GeV}/c^2)^2$ is applied to identify the scattered K^-.

The combination of these geometric and PID cuts ensures a high-purity sample of

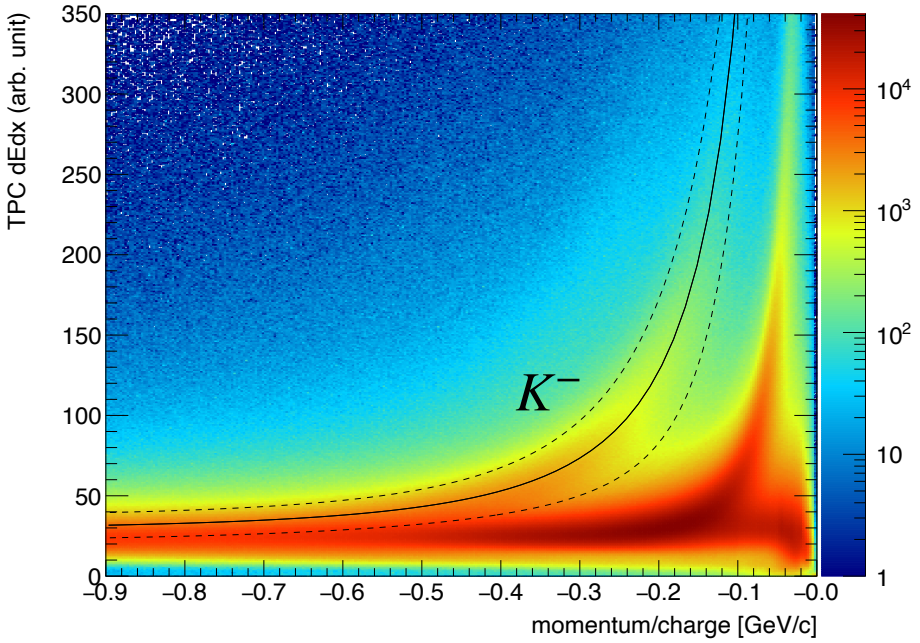

Figure 5.2: Correlation between momentum/charge and specific energy loss ($\langle dE/dx \rangle$) in the HypTPC for negatively charged tracks. The solid curves indicate the theoretical Bethe predictions for π^- and K^-. The dashed lines represent the $\pm 1.7\sigma$ selection boundaries for K^- identification.

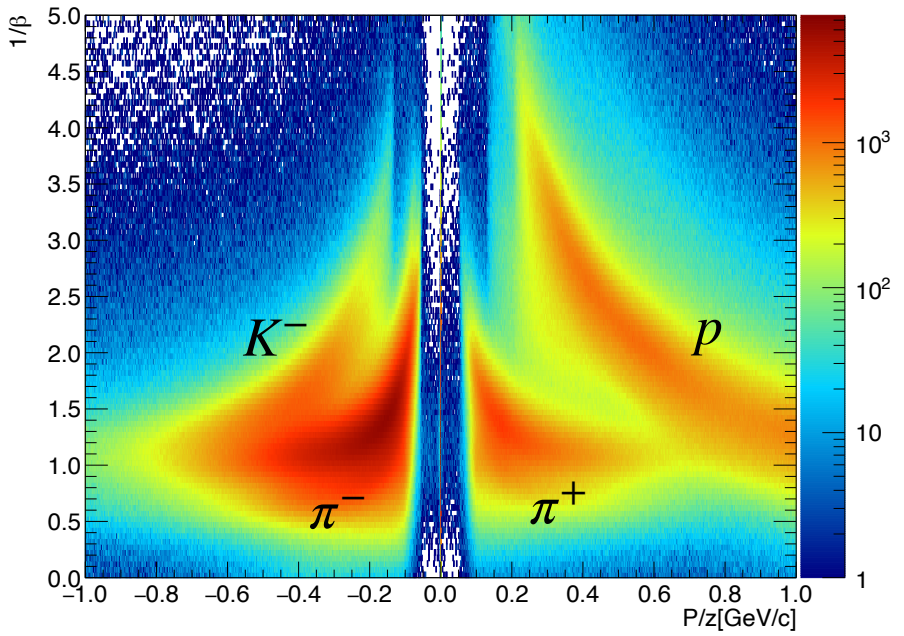

Figure 5.3: Correlation between inverse velocity $1/\beta$ and momentum/charge (p/q) reconstructed by the HypTPC. Theoretical curves for $\pi^{\pm}$ (black), $K^{\pm}$ (red), protons (blue), and deuterons (magenta) are overlaid, showing clear particle separation.

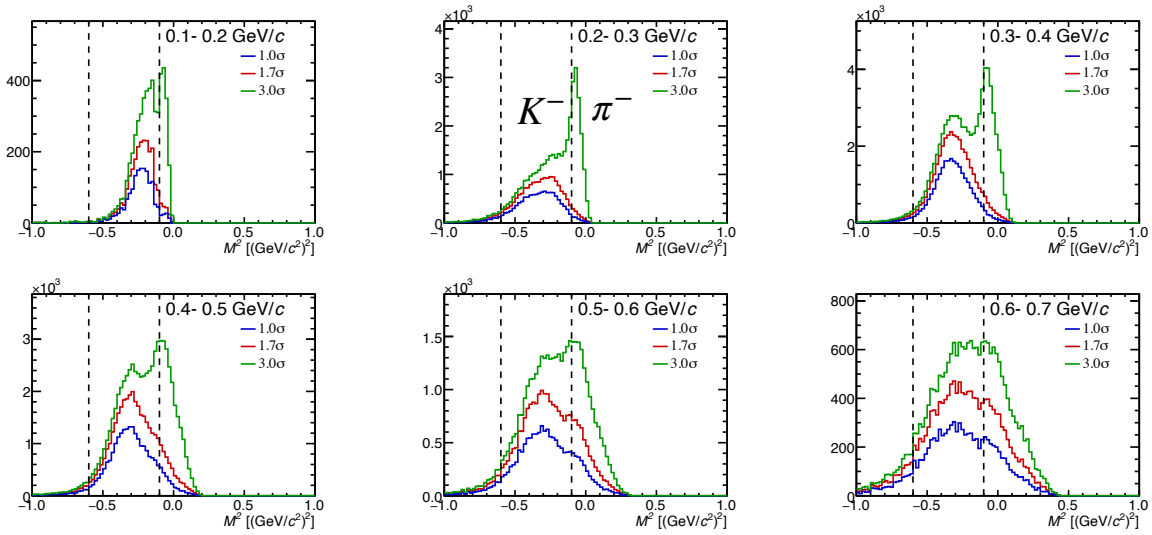

Figure 5.4: Squared mass (M^2) distribution for tracks selected by the dE/dx cut. The blue, red, and green histograms correspond to cut widths of 1.0σ, 1.7σ, and 3.0σ, respectively. The vertical dashed lines indicate the selection window for K^- candidates.

scattered K^- for the subsequent analysis. The optimization and validation of these cut conditions are discussed in detail in Section 5.2.2.

5.2.2 Optimization and Validation of PID Cuts

This section details the optimization and validation of the PID cut conditions defined in Sec. 5.2.1. The goal is to maximize the signal purity while maintaining high detection efficiency. This is achieved by quantitatively estimating the signal yield and background contributions using a fitting method, and comparing the results between experimental data and Monte Carlo simulations.

Yield/BG Estimation Method via M^2 Fitting In the analysis, a $\pm n\sigma$ region (the `dEdx` cut) centered on the expected K^- Bethe value is first selected from the `momentum` vs. `dEdx` distribution. The squared mass (M^2) distribution for negative-charge particles passing this cut is then fitted to separate the signal yield and background.

The fitting function used is either a sum of two Gaussian functions assuming K^- and π^- plus an unknown constant background (`gaus(`K^-`) + gaus(`π^-`) + const(BG)`) or a sum of a K^- Gaussian and a constant background (`gaus(`K^-`) + const(BG)`).

Figure 5.5 shows the M^2 distribution from real data (CH_2 target) for different `dEdx` cut widths. From left to right, the plots correspond to 1.0σ (tight cut), 2.0σ, and 3.0σ (wide cut) conditions. It is evident that for a tight cut (1.0σ), the K^- component (blue dotted line) is dominant and the π^- component (red dotted line) is suppressed. As the cut is widened, the π^- component becomes more significant, indicating a larger pion contamination.

For the following discussion, the signal and background counts are defined from the area within a specific Region of Interest (ROI) based on this fit:

- $N_{\mathbf{signal}}$ = Area of the K^- Gaussian function within the ROI.
- $N_{\mathbf{BG}}$ = Area of the π^- Gaussian function + Area of the constant BG within the ROI.

Optimization of the dEdx Cut Condition The changes in signal yield, background, and purity were investigated while varying the `dEdx` cut width ($n\sigma$), comparing data and simulation for the CH_2 target (Figure 5.6).

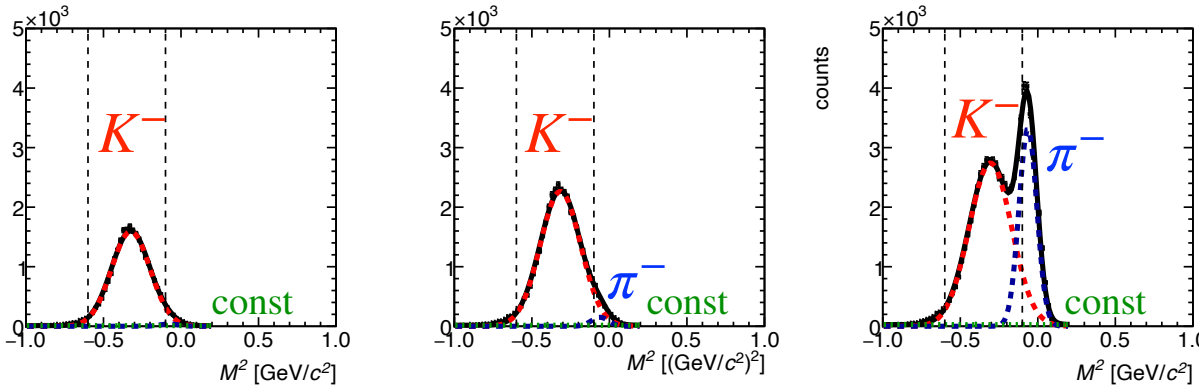

Figure 5.5: M^2 distributions for different dEdx cut conditions (1.0σ (left), 2.0σ (center), 3.0σ (right)) on CH_2 data. The plots show the fit components for K^- (blue), π^- (red), and background (green). Pion contamination is visibly reduced as the cut is tightened.

- **Signal Yield (Fig. 5.6 Left):** N_{signal} is plotted against the `dEdx` cut width. The data (red circles) and simulation (green squares) are normalized at the leftmost point for comparison. Around 2.0σ, the data begins to deviate from and exceed the simulation. This is interpreted as the inclusion of an unknown background (other than π^-) into the K^- signal region (M^2 cut region), which is not accounted for in the simulation.

- **Background Yields (Fig. 5.6 Center):** This plot shows the background counts (N_{BG}) versus the `dEdx` cut width. The total background (blue squares) is decomposed into contributions from pions (N_π, green triangles) and an unknown component (N_{unkn}, red circles). Both components show an increasing trend, particularly above 2.0σ.

- **Purity (Fig. 5.6 Right):** This shows the purity ($N_{\text{signal}}/(N_{\text{signal}} + N_{\text{BG}})$) versus the `dEdx` cut width. Considering the signal yield (left) and purity (right) plots together, a cut condition tighter than 2.0σ is necessary to maintain high purity. Based on this study, a cut of $\pm 1.7\sigma$ was chosen as the final selection criterion. This value offers a high purity of over 95% while retaining a significant portion of the signal yield, representing a good compromise between statistical precision and background rejection.

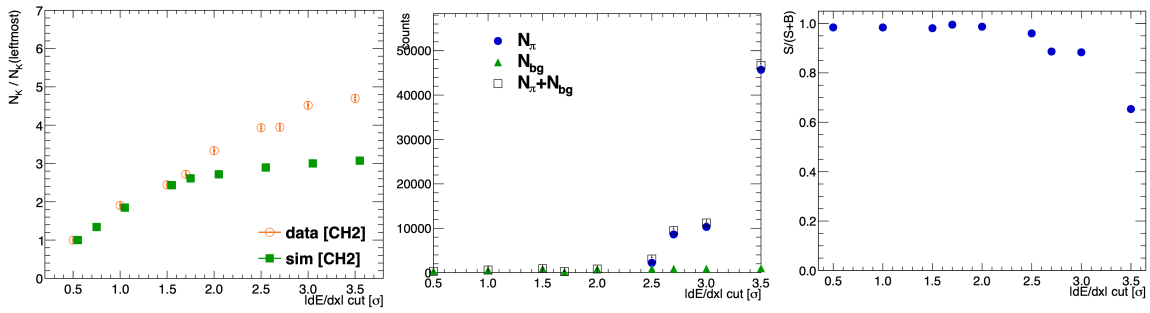

Figure 5.6: PID cut optimization study using CH_2 data. (Left) Normalized signal yield (N_K) vs. dE/dx cut width, comparing data (red circles) and simulation (green squares). (Center) Background yields (N_{BG}) vs. dE/dx cut width. The total background (blue squares) is decomposed into contributions from pions (N_π, green triangles) and an unknown component (N_{unkn}, red circles). (Right) Purity as a function of the dE/dx cut width. The deviation between data and simulation in the signal yield above 2.0σ suggests increasing background contamination.

Validation of Final Cut Conditions The reliability of the simulation is further validated by comparing the PID efficiency between real data (CH_2) and simulation (CH_2) as a function of the cut tightness (Figure 5.7).

The figure shows the efficiency versus the cut width for the `dEdx` cut (left) and M^2 cut (right). For both cuts, the efficiency trends as a function of cut width are in good agreement between data (orange triangles) and simulation (green triangles). A systematic deviation of about 5% (relative difference) is observed. This difference is attributed to the limitations of the simulation's reproducibility (e.g., modeling of detector response) and will be included as a systematic error in the final cross-section derivation. The red vertical lines indicate the final cut values used in this analysis, where an absolute efficiency difference of approximately 3% is observed.

Based on these studies, the final PID cut conditions for `dEdx` ($\pm 1.7\sigma$) and M^2 ($0.10 < m^2 < 0.60$ $(\text{GeV}/c^2)^2$) are confirmed to be robust.

Application to the Escape Spectrum As a final step in this section, we apply the validated PID procedure to construct the background-subtracted escape K^- spectrum. Figure 5.9 shows the raw escape spectrum (black) as a function of missing mass. The

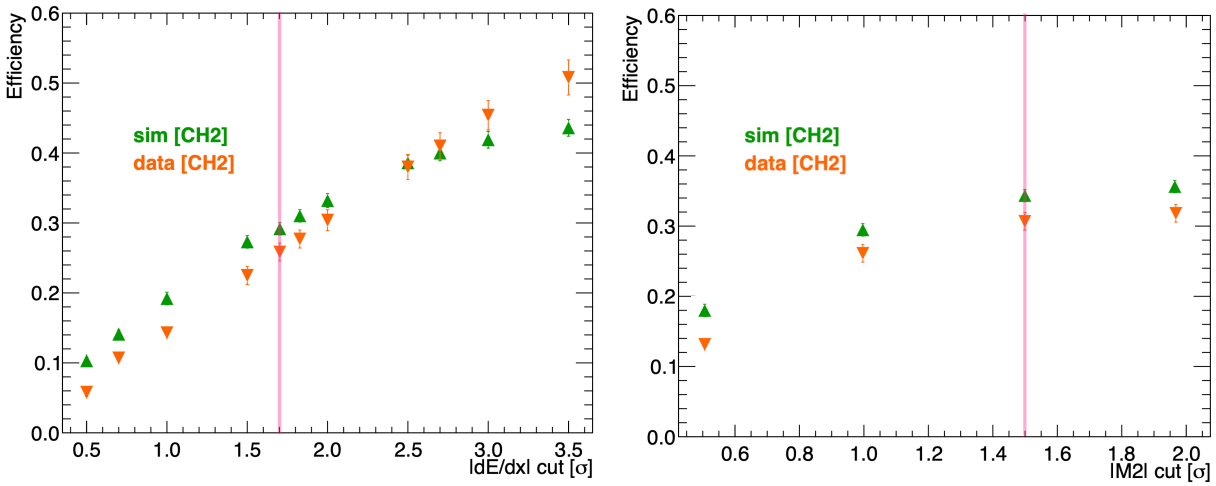

Figure 5.7: Comparison of PID cut efficiency between data (orange) and simulation (green) for the CH_2 target. (Left) Efficiency vs. dE/dx cut width. (Right) Efficiency vs. M^2 cut window. The red vertical lines indicate the final cut values used in the analysis, where an absolute efficiency difference of ~3% is observed between data and simulation.

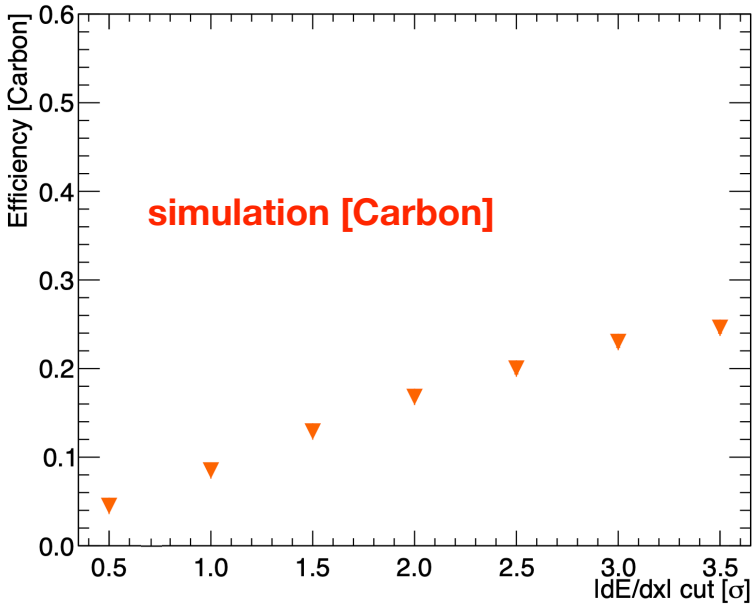

Figure 5.8

background component (blue), estimated from the M^2 fitting procedure described in Sec. 5.2.2, is overlaid. The red distribution represents the escape spectrum after subtracting this background. This demonstrates that the non-kaonic background, which

is relatively small, can be reliably estimated and removed from the raw spectrum. Figure 5.10 compares the resulting count-based exclusive spectrum with the inclusive spectrum obtained in Chap. 4, illustrating the fraction of events corresponding to the escape channel.

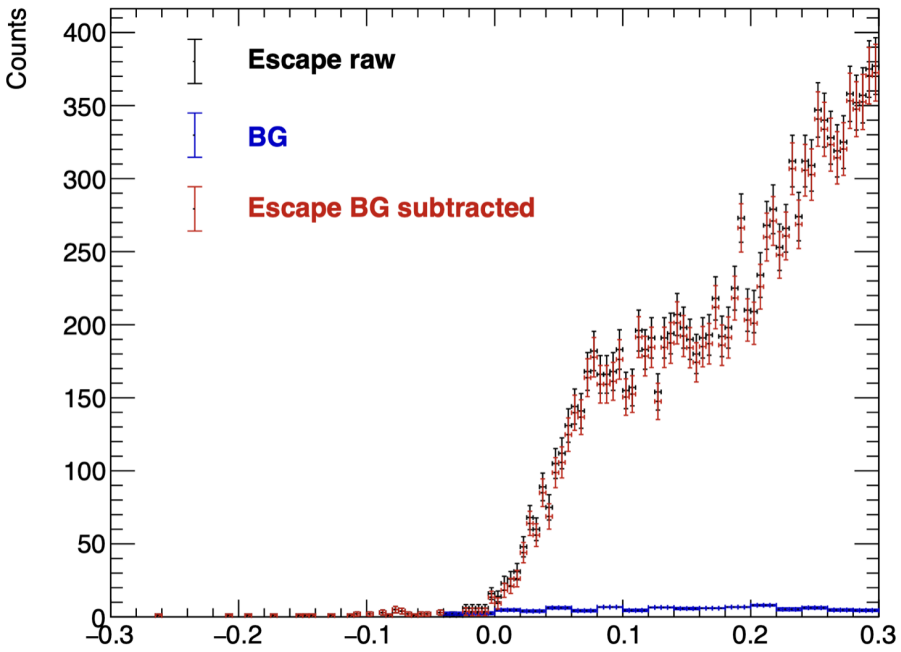

Figure 5.9: Estimation of background in the K^- escape spectrum. The black data points show the raw escape spectrum. The blue data points represent the background estimated from M^2 fitting. The red data points show the escape spectrum after background subtraction.

5.3 Physical Background Subtraction

With the non-kaonic background removed as described in Section 5.2.2, the next step is to address the physical background from competing reaction channels. Although the PID selection ensures a pure sample of kaons, the escape spectrum still contains contributions from inelastic K^- scattering processes that mimic the signal kinematics.

The reaction of interest is the quasi-free elastic scattering $^{12}\mathrm{C}(K^-, p)K^-$. However, the TPC also detects kaons from inelastic reactions occurring within the nucleus. To derive an accurate cross-section for the quasi-free elastic channel, these background events must be identified and subtracted using kinematic information.

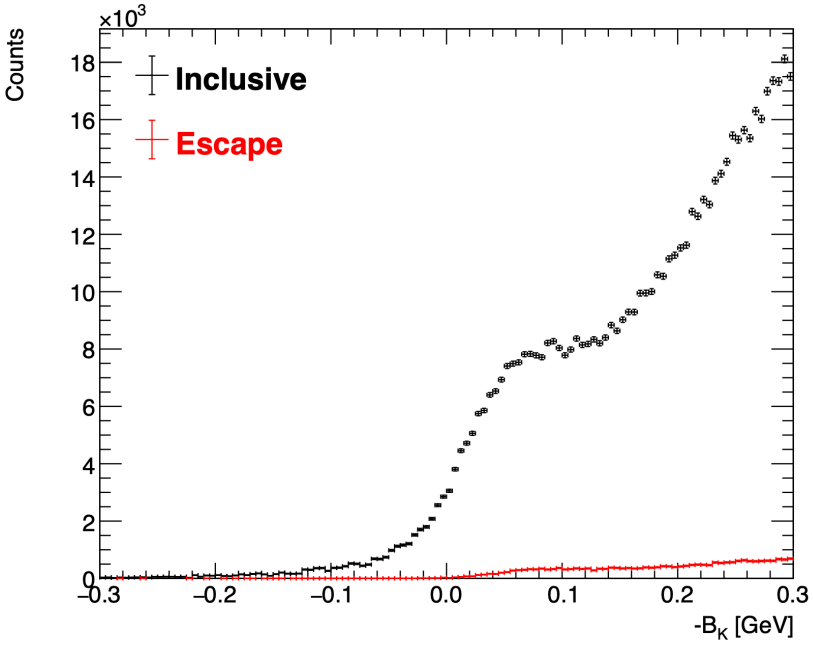

Figure 5.10: Count-based inclusive and escape spectra of the $^{12}\mathrm{C}(K^-, p)$.

5.3.1 Possible Background Process

The primary physical background competing with the quasi-free elastic scattering is the inelastic scattering process:

$$K^- + p \to K^- + \pi^0 + p. \tag{5.1}$$

Since a neutral pion is produced, this reaction contributes to the missing energy spectrum, creating a broad distribution that begins at the π^0 production threshold ($-B_K \approx m_{\pi^0} \approx 135\,\mathrm{MeV}$). In the larger energy region ($-B_K \geq\sim 135\,\mathrm{MeV}$), this inelastic process overlaps significantly with the tail of the quasi-free elastic signal, becoming a dominant source of contamination. Therefore, distinguishing and subtracting the $K^-\pi^0 p$ component is essential for extracting the pure quasi-free signal.

5.3.2 Background Rejection using Missing Momentum Analysis

To discriminate between the signal ($K^- p \to K^- p$) and the background ($K^- p \to K^- \pi^0 p$), we utilize the difference between the missing momentum calculated from the spectrometers and the K^- momentum measured by the TPC. This quantity, P_{diff}, is defined as:

$$P_{\text{diff}} = |\vec{P}_{\text{miss}} - \vec{P}_{K^-(\text{TPC})}|, \tag{5.2}$$

where $\vec{P}_{\text{miss}} = \vec{P}_{\text{beam}} - \vec{P}_{\text{proton}}$ is the missing momentum reconstructed by the K1.8 beamline and KURAMA spectrometers, and $\vec{P}_{K^-(\text{TPC})}$ is the momentum of the scattered K^- reconstructed by the HypTPC.

The behavior of P_{diff} differs distinctly between the two processes:

- **Quasi-free Elastic Scattering ($K^- p \to K^- p$):** For this two-body final state, momentum conservation implies $\vec{P}_{\text{miss}} \approx \vec{P}_{K^-(\text{TPC})} + \vec{P}_N$, where $\vec{P}_N$ is the initial momentum of the target nucleon. Therefore, $P_{\text{diff}} = |\vec{P}_{\text{miss}} - \vec{P}_{K^-(\text{TPC})}| \approx |\vec{P}_N|$. The distribution of P_{diff} thus directly reflects the Fermi momentum distribution of nucleons in the carbon nucleus, peaking at a low value.

- **Inelastic Scattering ($K^- p \to K^- \pi^0 p$):** In this three-body reaction, the missing momentum is shared between the unobserved π^0 and the scattered K^-, i.e., $\vec{P}_{\text{miss}} \approx \vec{P}_{K^-(\text{TPC})} + \vec{P}_{\pi^0} + \vec{P}_N$. The momentum of the detected K^- is therefore generally smaller than the missing momentum. This results in a broad P_{diff} distribution that extends to much higher values.

Simulation and Template Generation: To separate these components quantitatively, templates for the P_{diff} distribution were generated using Monte Carlo simulations. The kinematic models used for each process are as follows:

1. **Signal ($K^- p \to K^- p$):** To realistically reproduce the scattering within the ^{12}C nucleus, the initial state proton was modeled accounting for both its Fermi momentum and off-shellness.

2. **Background ($K^- p \to K^- \pi^0 p$):** Due to the limited experimental data on the differential cross-section for this specific reaction channel, the decay was assumed

to follow a uniform phase-space distribution.

Figure 5.11 shows the simulated P_{diff} distributions for the signal (left) and background (right). The clear separation in their shapes validates the use of this variable for discriminating between the two processes.

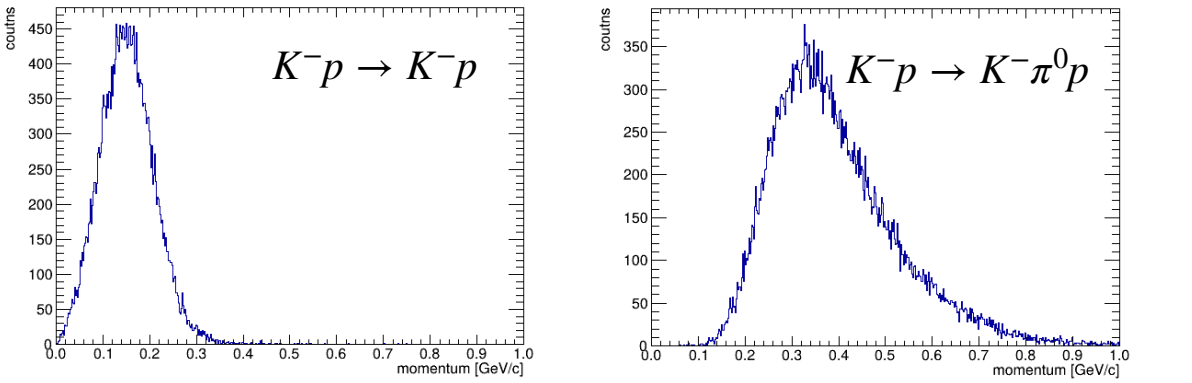

Figure 5.11: Simulated distributions of the momentum difference $P_{\text{diff}} = |\vec{P}_{\text{miss}} - \vec{P}_{K^-(\text{TPC})}|$. (Left) Quasi-free elastic scattering $K^-p \to K^-p$. (Right) Inelastic background $K^-p \to K^-\pi^0p$. The signal peaks at low values reflecting Fermi motion, while the background is broadly distributed due to the three-body kinematics.

Fitting and Subtraction: In the analysis of real data, the P_{diff} distribution was constructed for each bin of $-B_K$. The relative contributions of signal and background were determined by fitting the data with the simulated templates described above.

Figure 5.12 shows the fitting results for representative $-B_K$ bins. The data (black points) are well described by the sum (red line) of the signal (blue line) and background (green dotted line) templates. Using the scaling factors determined from the fit, the background contribution was subtracted from the raw escape spectrum.

Figure 5.13 presents the final result of this subtraction procedure. The raw escape spectrum (black points) is decomposed into the estimated physical background from the $K^-\pi^0p$ channel (green histogram) and the final, purified quasi-free elastic signal (red histogram).

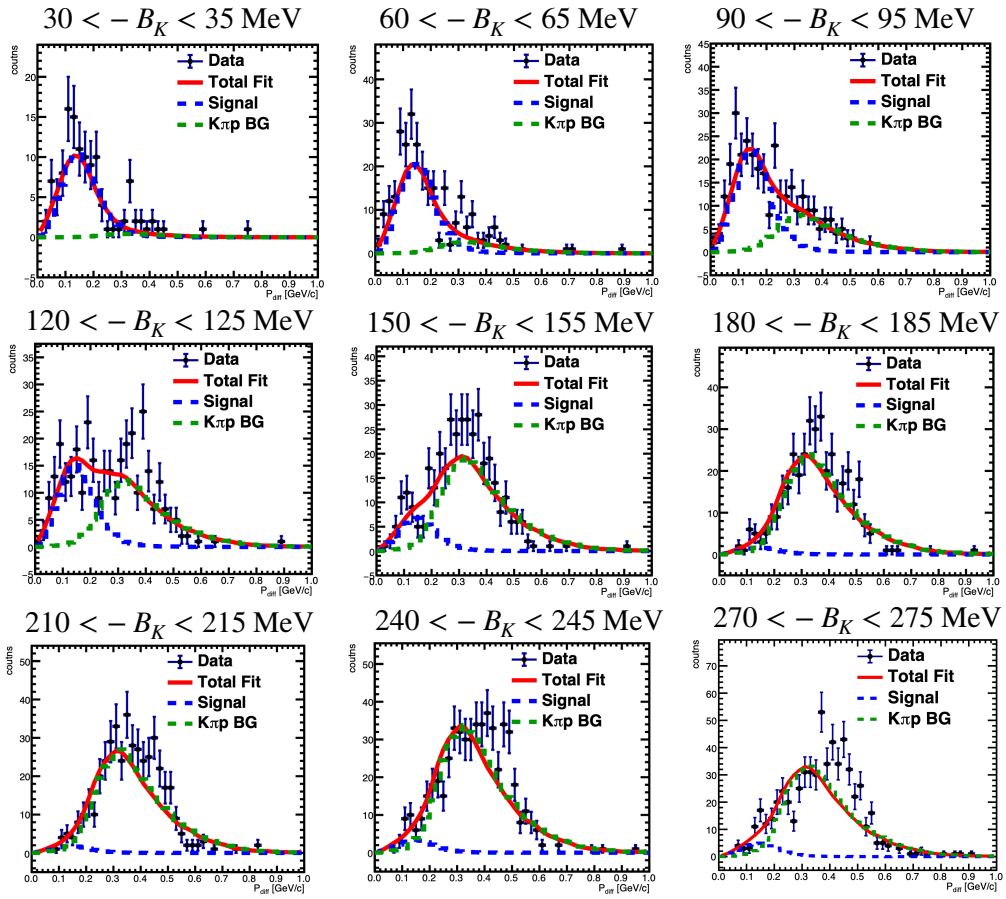

Figure 5.12: Fitting of the P_{diff} distributions in slices of $-B_K$. The data (black) are fitted with a combination of the signal template (blue) and the physical background template (green). The red line indicates the total fit.

Systematic Uncertainty in Physical Background Estimation In the template fitting used to evaluate the physical background contribution, the effect of the fitting range selection on the result was evaluated as a systematic uncertainty. Changing the fitting range causes variations in the template shape and the χ^2 value, which introduces uncertainty into the evaluation of the physical background.

To estimate this systematic uncertainty, the fit was performed repeatedly while varying the fitting range in steps corresponding to 0.02 GeV/c (a fit range scan), and the variation in the resulting signal yield was evaluated. The sum of χ^2 in the binding energy region of interest ($-0.04 < B_{Ek} < 0.20$ GeV) was used as a metric, and the condition that minimized this sum was adopted as the nominal fitting range.

The systematic uncertainty was calculated using the maximum (I_{max}) and mini-

mum (I_{min}) signal yields obtained when the fitting range was varied within ±2 steps (corresponding to ±0.04 GeV/c) around this optimal range:

$$\sigma_{\mathrm{syst}} = \frac{I_{\mathrm{max}} - I_{\mathrm{min}}}{2} \tag{5.3}$$

As a result of this evaluation, the relative systematic uncertainty on the signal yield from the physical background estimation was found to be 2.1%. This contribution is included in the total systematic uncertainty discussed in Sec. 5.5.

The cross-section is derived from this background-subtracted signal, as presented in Sec. 5.6.

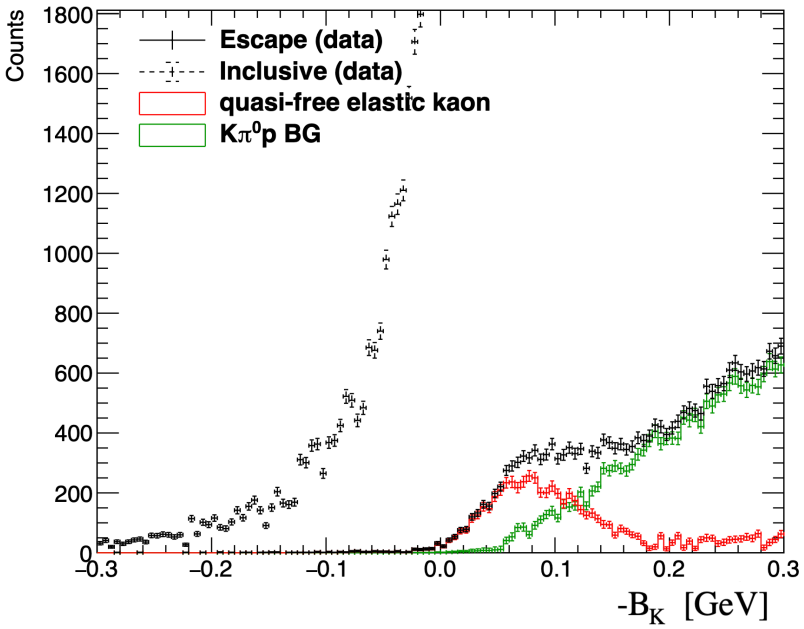

Figure 5.13: The measured escape spectrum (black points) decomposed into the signal component (red histogram) and the physical background component (green histogram) estimated via the template fitting method.

5.4 TPC Acceptance Estimation

To derive the absolute cross-section for the escape K^- channel, the background-subtracted yield must be corrected for the detection efficiency of the HypTPC. This efficiency, often referred to as acceptance, is a comprehensive factor that accounts for the detector's geometrical coverage, the survival probability of the K^- (against decay and hadronic

interactions), and the efficiencies of the track reconstruction and particle identification (PID) cuts.

This acceptance correction factor is calculated using a detailed Monte Carlo (MC) simulation. Given the critical role of this correction, it is essential to validate the reliability of the simulation. This section details the methodology for both the acceptance estimation and its validation.

5.4.1 Methodology for Acceptance Estimation and Validation

The core of our strategy is to validate the MC simulation using the elementary reaction on a proton target, $K^- p \to K^- p$, before applying it to the quasi-free reaction on the carbon target. The validation procedure is structured as follows:

1. **Simulation of Proton Target Reaction:** We first use the MC simulation to calculate the detection efficiency for K^- from the $K^- p \to K^- p$ reaction in CH_2 target. The simulation models the detector geometry, material effects (energy loss, multiple scattering), particle physics processes (K^- decay, hadronic interactions), and the full analysis chain, including PID cuts.

2. **Experimental Measurement on Proton Target:** We then measure the same efficiency using experimental data. This is achieved by statistically isolating the proton target contribution through a subtraction of the normalized Carbon target data from the CH_2 target data.

3. **Validation via Comparison:** The simulation is considered validated if the calculated efficiency from step 1 agrees with the experimentally measured efficiency from step 2 within uncertainties.

4. **Application to Carbon Target:** Finally, with the validated simulation framework, we calculate the acceptance for the quasi-free scattering process on the ^{12}C target. It should be noted that the density difference between the ^{12}C (diamond) and CH_2 targets leads to distinct energy loss (dE/dx) characteristics. This difference has a significant impact on the detection efficiency and acceptance. A crucial cross-check is performed by demonstrating that applying the respective acceptance corrections to the raw Carbon data and the statistically-extracted

Carbon data (from $CH_2 - H_2$ subtraction) yields consistent final spectra. This confirms that the simulation correctly models the significant target-dependent effects.

The following subsections will detail each of these steps.

5.4.2 Evaluation by Simulation: Proton Target

The detection efficiency for K^- from a proton target was evaluated using a detailed MC simulation.

Simulation Inputs and Methodology: The simulation utilized the experimentally measured distributions of the incoming beam K^- and the scattered proton momenta as kinematic inputs. The reaction process was assumed to be a scattering event between the beam K^- and a proton at rest within the CH_2 target.

1. A scattered K^- was generated based on the kinematics of the $K^-p \to K^-p$ reaction, using the measured beam K^- and scattered proton information. The momentum and angular resolutions of the spectrometers, as determined from data, were incorporated.

2. The generated K^- was passed through the simulator, which incorporates the experimental geometry (target, detectors). The same analysis procedure (tracking, PID cuts, etc.) as applied to the real data was then enforced.

3. The K^- detection efficiency was defined as the ratio of the number of K^- that passed all analysis cuts to the total number of generated K^-.

Incorporated Physical Processes and Conditions: The simulation included the following realistic effects that influence the detection efficiency:

- **Electromagnetic Interaction (`EM`):** Energy loss and multiple scattering in materials.

- **Hadronic Interaction (`Hadron`):** Loss of K^- due to nuclear interactions with the target and detector materials.

- **Kaon Decay (`Decay`):** In-flight decay of the K^- (lifetime ≈ 12.4 ns).
- **Analysis Cuts (`PIDcut`):** The specific PID cuts used in the analysis.
- **Nuclear Effects (`Fermi`):** For the Carbon target simulation, the initial state proton was modeled using a spectral function that accounts for both Fermi momentum (mean: 0.145 GeV/c, $\sigma = 0.050$ GeV/c) and nucleon off-shellness.

Separation of Contributions: To quantify the impact of each physics process on the detection efficiency, a factor analysis was performed using the simulation. The baseline efficiency was first established by enabling only electromagnetic interactions (`EM only`), which primarily reflects the geometrical acceptance. Then, other key physics processes—hadronic interactions (`Hadron`), kaon decay (`Decay`), and analysis cuts (`PID Cuts`)—were added individually to this baseline to assess their independent impact. Finally, a full simulation including all effects simultaneously was performed to obtain the final, realistic detection efficiency. The results for the CH_2 and Carbon targets are summarized in Table 5.1.

Table 5.1: Factor analysis of the simulated K^- detection efficiency. The impact of each physics process is evaluated by adding it individually to the baseline `EM only` simulation.

Target	Baseline (`EM only`)	Efficiency with one additional process				Full Simulation
		`+ Hadron`	`+ Decay`	`+ PID Cuts`	`+ Fermi`	
Empty	55.9%	55.2%	48.4%	28.5%	49.4%	—
CH2	54.2%	52.5%	45.8%	29.1%	—	**24.2%**[a]
Carbon	29.1%	27.7%	25.7%	15.8%	30.8%	**12.5%**[b]

[a] Full Sim. (CH2) = +Hadron +Decay +PIDcut
[b] Full Sim. (Carbon) = +Hadron +Decay +Fermi +PIDcut

This factor analysis highlights the following key points:

1. **Geometrical Acceptance and Target Effects:** The baseline efficiency for an empty target (shown in Table 5.1) was 55.9%, representing the pure geometrical acceptance of the HypTPC. For the CH_2 and Carbon targets, this baseline is reduced to 54.2% and 29.1% respectively. The dramatic drop for Carbon is due to increased energy loss and multiple scattering in the denser target material,

causing more particles to fall outside the kinematic acceptance or fail analysis cuts. Further discussion on the validity for this simulation is presented at Sec. 5.4.5

2. **Impact of Individual Processes:** By comparing the columns in Table 5.1 for the CH_2 target, we can quantify the individual sources of inefficiency. Relative to the baseline of 54.2%, kaon decay is the largest single source of loss, reducing the efficiency to 45.8%. The PID analysis cuts also have a very significant impact, reducing the efficiency to 29.1%. Hadronic interactions have a smaller, but non-negligible, effect (52.5%).

3. **Final Simulated Efficiencies:** The full simulation, which combines all effects, yields a final detection efficiency of **24.2%** for the proton reaction (in CH_2) and **12.5%** for the quasi-free reaction on Carbon. These are the values used for the acceptance correction and validated against experimental data.

5.4.3 Evaluation by Experimental CH_2 Data

To validate the simulation, the K^- detection efficiency for the elementary K^-p reaction was derived directly from experimental data. The method relies on statistically isolating the events from the hydrogen component in the CH_2 target.Data sets from the polyethylene (CH_2) and carbon (C) targets were analyzed, with the carbon data scaled according to the beam intensity and the number of target nuclei. The pure hydrogen contribution was then extracted by performing a normalized $CH_2 - C$ subtraction. Figure 5.14 shows the resulting missing mass spectra for the $p(K^-, p)X$ reaction. The peak centered around 0.5 GeV/c^2 corresponds to the scattered K^- in the elastic scattering channel.The inclusive yield ($N_{\text{inclusive}}$), shown as the black spectrum in Fig. 5.14, represents events where the recoil proton was identified, regardless of the scattered kaon detection. The exclusive yield ($N_{\text{exclusive}}$), shown in red, corresponds to the subset of events where the scattered K^- was also successfully reconstructed by the spectrometer.To determine the signal yields, both spectra were fitted with a combined function of a Gaussian for the signal peak and a first-order polynomial for the background. The experimental detection efficiency was then defined as the ratio of the signal yields extracted from these fits:

$$\text{Efficiency}_{\text{exp}} = \frac{N_{\text{exclusive}}(K^- p \to K^- p)}{N_{\text{inclusive}}(K^- p \to X)}. \tag{5.4}$$

where N represents the integral of the Gaussian component obtained from the fitting procedure.

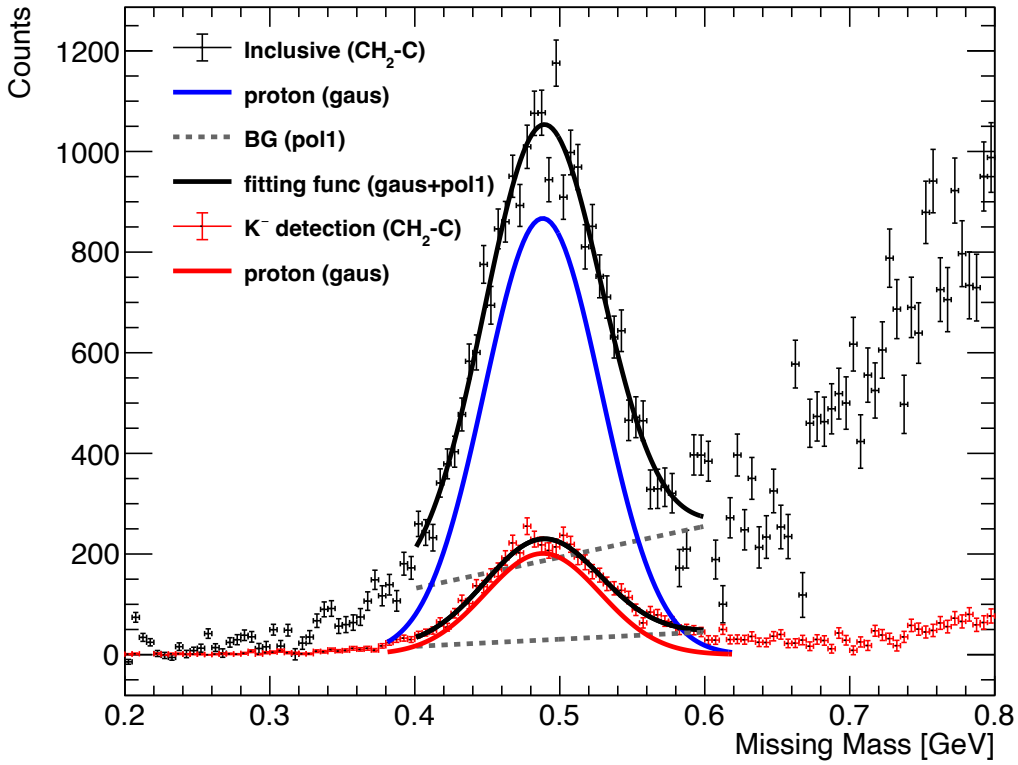

Figure 5.14: Missing mass spectra of the $p(K^-, p)X$ reaction used for the efficiency evaluation. The black points represent the inclusive yield derived from the CH_2 data after carbon subtraction. The red points show the exclusive yield requiring the detection of the scattered K^-. The solid curves indicate the best-fit functions (Gaussian signal + first-order polynomial background) for the inclusive (black curve) and exclusive (red curve) distributions, respectively. The blue curve highlights the signal component (Gaussian) of the inclusive spectrum.

5.4.4 Comparison and Discussion

The K^- detection efficiencies for the proton target, as derived from simulation and experimental data, are compared below.

- **Simulation:** Detection efficiency $= 24 \pm 3\%$ (syst.)

- **Experimental Data:** Detection efficiency = $22 \pm 2\%$ (stat.)

The systematic uncertainty on the simulation result was estimated to be 3% relative (i.e., $24 \pm 3\%$), obtained by varying simulation parameters such as material budgets and detector response. The experimental value has a statistical uncertainty of $\sim$9% relative ($22 \pm 2\%$).

The values from the simulation ($24 \pm 3\%$) and the experimental data ($22 \pm 2\%$) are in reasonable agreement within their respective uncertainties. This agreement provides strong confidence that our simulation framework realistically models the absolute K^- detection efficiency, including the effects of detector geometry, material interactions, particle decay, and analysis cuts. Further discussion on the validity for this simulation is presented at Sec. 5.4.5.

5.4.5 Validation of Target Material Effects on Efficiency

Finally, we verify the validity of the entire analysis chain—including acceptance correction and background subtraction—by comparing results from different target materials. Specifically, we confirm that the large efficiency reduction predicted for the Carbon target (due to energy loss and absorption) is correctly modeled by the simulation.

As established in the previous subsection (Table 5.1), the simulation under the "`EM only`" condition predicted a significant drop in detection efficiency for the Carbon target (29.1%) compared to the Empty (55.9%) or CH_2 (54.2%) targets. This reduction is substantially larger than what can be attributed to geometrical size or density alone, suggesting that increased K^- energy loss and multiple scattering within the carbon target severely impact the TPC acceptance and subsequent analysis cuts.

This subsection aims to verify, using experimental data, that this large efficiency reduction predicted by the simulation is a genuine physical effect and not an artifact. The validation is performed by comparing two "Carbon K^- Escape Spectra" derived via physically equivalent but experimentally distinct methods:

1. **Escape (C) (Blue):** The escape spectrum measured directly from the Carbon target.

2. **Escape (C in CH2) (Red):** The escape spectrum statistically extracted from the CH_2 target data by subtracting the contribution from the H $\boxtimes$ (proton) target.

Figure 5.15 displays these two spectra. The crucial point is that both spectra have been corrected for detection efficiency using their respective, distinct, simulation-derived values from the previous section (i.e., the "Full Sim." efficiencies for `Carbon` and `CH2`).

As observed in the figure, the two spectra agree with each other within a relative difference of 5.3% in the region of interest ($-B_K$: 0–0.2 GeV). This level of agreement confirms the reliability of the simulation in modeling the target-dependent efficiency. The residual 5.3% difference is taken as the systematic uncertainty associated with the efficiency correction, as discussed in Section 5.5.

Discussion: The simulation-derived efficiencies for `Carbon` (12.5%) and `CH2` (24.2%) are markedly different. The fact that the two raw data spectra, Escape (C) and Escape (C in CH2), become consistent after applying these different correction factors provides strong evidence for the simulation's validity. It demonstrates that the simulation correctly models the complex, target-dependent effects—including geometric acceptance, energy loss, multiple scattering, decay, and hadronic interactions—and thus validates the large, calculated efficiency correction for the carbon target.

5.5 Systematic Uncertainty Evaluation

The systematic uncertainties associated with the derivation of the escape K^- cross-section were evaluated. The contributions are summarized below.

5.5.1 Uncertainty in Efficiency Correction

The dominant source of systematic uncertainty arises from the acceptance correction for the Carbon target. As demonstrated in Sec. 5.4.5, the validity of the simulation-based efficiency correction was verified by comparing the escape spectrum measured directly from the Carbon target with that statistically extracted from the CH_2 target. A residual relative difference of 5.3% was observed between the two efficiency-corrected spectra. This difference is taken as the systematic uncertainty on the acceptance correction, reflecting the limitations in modeling target-dependent effects like energy loss and hadronic interactions. Consequently, a systematic uncertainty of 5.3% is assigned to the final cross-section.

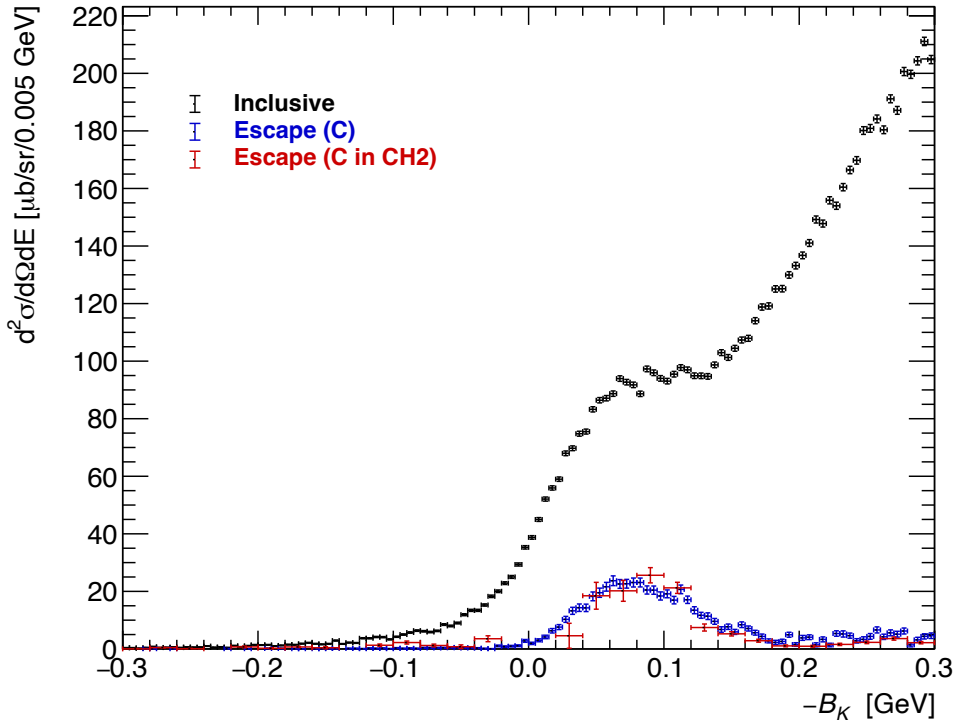

Figure 5.15: Comparison of the efficiency-corrected K^- escape spectra. The spectrum measured from the Carbon target (Blue: **Escape (C)**) is compared with the spectrum statistically extracted from the CH_2 target (Red: **Escape (C in CH2)** = CH2(K^-, p) - H2(K^-, p)). The red spectrum is rebinned to reduce statistical fluctuations while maintaining the spectral shape. The inclusive spectrum (Black) is shown for reference. The red and blue spectra agree with each other within a relative difference of 5.3%, and this agreement confirms the reliability of the simulation in modeling the target-dependent efficiency.

5.5.2 Stability of PID Conditions

The systematic uncertainty associated with the particle identification (PID) criteria was evaluated by varying the selection cut conditions. The thresholds for the specific energy loss (dE/dx) and the squared mass (M^2) were varied within reasonable ranges around their nominal values. The resulting variation in the K^- yield was found to be approximately 1.9%. This contribution is relatively small compared to the acceptance uncertainty.

5.5.3 Uncertainty in Physical Background Subtraction

As described in Sec. 5.3.2, the systematic uncertainty associated with the physical background subtraction procedure was evaluated by studying the stability of the result with respect to the template fitting range. The variation in the signal yield was found to be 2.1%.

5.5.4 Detector Efficiency and Acceptance

The consistency of the detector efficiency between the simulation and experimental data was evaluated using the proton target. The simulation yielded an efficiency of $24 \pm 3\%$, while the experimental data showed $22 \pm 2\%$. Although they are in reasonable agreement within their uncertainties, the relative difference of 8.3% was assigned as a systematic uncertainty on the absolute normalization of the cross-sections. Since the detection of the escaping K^- meson relies on the HypTPC acceptance, this uncertainty directly propagates to the determined escape probability P_{esc}.

5.5.5 Total Systematic Uncertainty

The individual contributions from the efficiency correction (5.3%), PID stability (1.9%), and physical background subtraction (2.1%) are combined in quadrature (= 10.2%). The total systematic uncertainty is conservatively assigned as 10.2%.

5.6 Cross-section for Inclusive and Escape Process

Having validated the inclusive spectrum, we proceed to isolate the "escape" process. The escape events are defined as those where the quasi-free K^- is exclusively detected by the HypTPC, identifying it as a surviving particle that did not undergo absorption in the nucleus.

5.6.1 Definition

The differential cross-section for the escape K^- was derived by correcting the raw yield with the HypTPC acceptance ϵ_{esc}:

$$\left\langle \frac{d^2\sigma}{d\Omega dE} \right\rangle_{\rm esc} = (K^-\text{-escape}) \times \frac{1}{\varepsilon_{\rm esc}} \left\langle \frac{d^2\sigma}{d\Omega dE} \right\rangle_{\rm inc} \tag{5.5}$$

where the "K^--escape" is defined as requirement of K^- detection and the physical background subtraction as already explained in Sec 5.2.1 and Sec 5.3, respectively.

5.6.2 Result

Figure 5.16 displays the resulting escape K^- spectrum (red histogram), compared to the inclusive data (blue dots). The escape spectrum shows a significantly reduced magnitude. This reduction is a direct physical consequence of the K^- absorption in the nuclear medium; the difference between the generated QFES flux and the escaping flux corresponds to the absorbed component.

To quantify the escape process, we integrated the differential cross-section over the QFES region, defined as $-B_K \in [-0.040, 0.200]$ GeV (red hatched area in Fig. 5.16). The lower bound of the integration range is chosen to account for the spill-out effect due to the experimental resolution. The upper bound is determined from theoretical calculations, which will be introduced in Chap. 6, as the region where its contribution to the total escape cross section is less than 1%, irrespective of the value of the imaginary part of the optical potential. This range covers the entire QFES peak structure. The resulting integrated cross section for the escape process is:

$$\left(\frac{d\sigma}{d\Omega}\right)_{\rm esc} = 436 \pm 6\ (\text{stat.}) \pm 26\ (\text{syst.})\ \mu\text{b/sr}, \tag{5.6}$$

where the first term represents the statistical error, and the second term represents the systematic error.

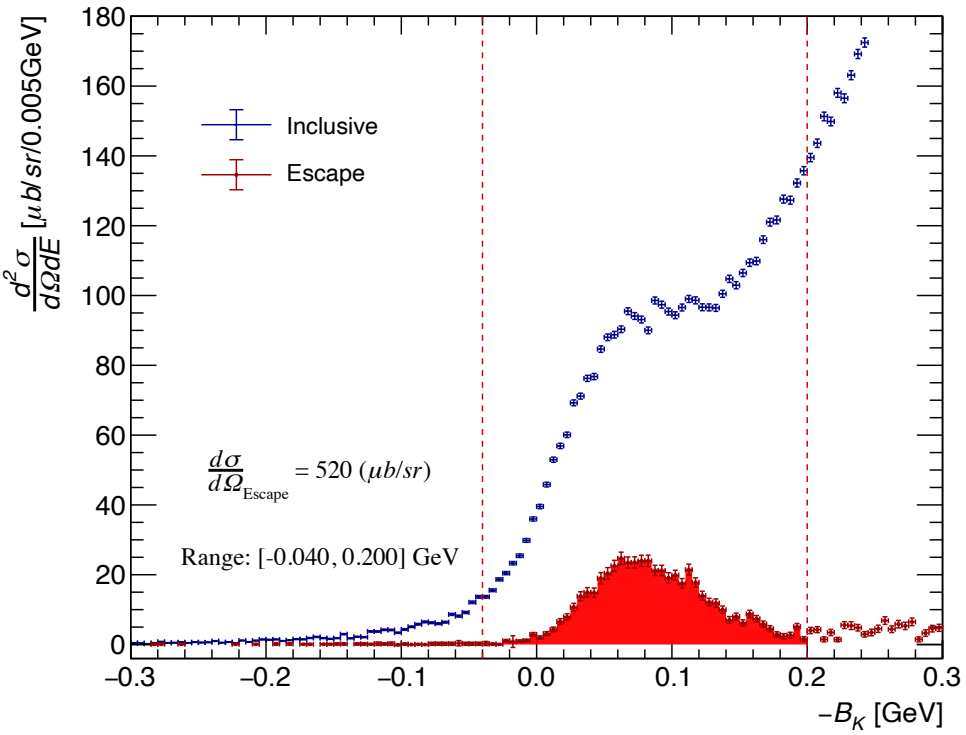

Figure 5.16: Differential cross section spectrum of escape K^- in the ^{12}C(K^-, p) reaction (red histogram), corrected for HypTPC acceptance, and the inclusive data (blue dots) is also shown. The red hatched area indicates the integration range ($-0.040 \leq -B_K \leq 0.200$ GeV) used to derive the escape K^- cross section.

Chapter 6

Discussion

6.1 Objectives

In the preceding chapters, we derived the inclusive cross-section and the escape cross-section for the $^{12}\mathrm{C}(K^-, p)$ reaction. This chapter builds upon these experimental results to discuss their physical implications for the $\bar{K}$-nucleus interaction.

The primary objective of this chapter is to place quantitative constraints on both the real (V_0) and imaginary (W_0) parts of the K^--nucleus optical potential. Unlike previous studies, this work employs a simultaneous χ^2 minimization analysis of the inclusive and escape spectra. This approach provides a unique and high-precision sensitivity to the absorption mechanism within the nuclear medium.

The discussion in this chapter is organized as follows:

- **Theoretical Framework**: We first introduce the Green's function method, which allows for a unified treatment of the bound state and quasi-free continuum regions while incorporating a complex optical potential.
- **Analysis Methodology**: We describe the simultaneous fitting model, which combines theoretical templates with quasi-free scattering components. This model utilizes branching ratios and constraints from the J-PARC E05 experiment to ensure a robust decomposition of complex reaction processes.
- **Determination of Potential Depths**: By comparing the experimental data with theoretical predictions through a grid search in the (V_0, W_0) parameter space, we determine the optimal potential parameters.

- **Physical Implications**: Finally, we discuss the nature of the determined potential, characterized by a moderately attractive real part ($V_0 \approx -72$ MeV) and a remarkably deep imaginary part ($W_0 \approx -100$ MeV). This significant absorptive strength provides quantitative evidence for the dominance of multi-nucleon absorption processes, such as $K^- NN \to YN$, within the dense nuclear interior.

6.2 Theoretical Framework: Green's Function Method

6.2.1 Physical Motivation for the Green's Function Approach

The Green's function method is a powerful theoretical framework used to calculate the inclusive energy spectra of nuclear reactions, such as the (K^-, p) reaction, particularly in the context of mesonic atoms and nuclei. A significant advantage of this method is its ability to treat both the bound state region and the quasi-free continuum region in a unified manner [66, 74]. In systems involving strong interactions, such as kaonic nuclei, the bound states often acquire large widths due to strong absorptive potentials. In such cases, the distinction between bound states and the continuum becomes ambiguous, making approaches that assume discrete eigenstates less effective. The Green's function method overcomes this by summing over all possible final states, thereby allowing for the evaluation of the nuclear response function covering the entire energy range of interest without assuming discrete bound states.

6.2.2 Formalism

In the Green's function method, the double differential cross-section for the (K^-, p) reaction on a nuclear target is typically formulated within the impulse approximation. The cross-section is factorized into the elementary cross-section of the $K^- p \to K^- p$ reaction and the nuclear response function $S(E)$:

$$\left(\frac{d^2\sigma}{d\Omega dE}\right)_A^{lab} = \left(\frac{d\sigma}{d\Omega}\right)_{ele}^{lab} \times S(E), \tag{6.1}$$

where E is the energy transfer. The nuclear response function $S(E)$ describes the probability of producing a kaon-nuclear system and is expressed in terms of the Green's function $G(E; \boldsymbol{r}, \boldsymbol{r}')$:

$$S(E) = -\frac{1}{\pi}\mathrm{Im}\sum_f \int d\boldsymbol{r}d\boldsymbol{r}'\tau_f^\dagger(\boldsymbol{r})G(E;\boldsymbol{r},\boldsymbol{r}')\tau_f(\boldsymbol{r}'), \tag{6.2}$$

where τ_f represents the transition amplitude. The Green's function $G(E)$ contains the information of the strong interaction between the meson and the nucleus, encapsulated in the Hamiltonian H_K:

$$G(E,\boldsymbol{r},\boldsymbol{r}') = \langle p^{-1}|\phi_K(\boldsymbol{r})\frac{1}{E-H_K+i\epsilon}\phi^\dagger(\boldsymbol{r}')|p^{-1}\rangle, \tag{6.3}$$

where ϕ_K is the kaon field operator and $|p^{-1}\rangle$ denotes the proton-hole state. The Hamiltonian H_K includes the complex optical potential $U(r)$, which is often parameterized phenomenologically as being proportional to the nuclear density distribution $\rho(r)$:

$$U(r) = (V_0 + if_{\mathrm{phase}}(E)W_0)\frac{\rho(r)}{\rho(0)}. \tag{6.4}$$

Here, V_0 and W_0 represent the real and imaginary depths of the optical potential at the nuclear center, respectively. Notably, the imaginary part of the optical potential has an energy dependence via $f_{\mathrm{phase}}(E)$ in this calculation. By solving the Klein-Gordon equation with this optical potential, the Green's function accounts for the distortion of the kaon wave function and the absorption effects inside the nucleus.

In this section, we derive the escape process of K^- in the nuclear medium. This quantity serves as a fundamental experimental result for discussing the K^--nucleus interaction in the subsequent sections.

6.2.3 Definition of Escape Probability

The escape probability, P_{esc}, is defined as the ratio of the integrated cross-section of the escape process to that of the total quasi-free elastic scattering (QFES) process. It represents the fraction of K^- mesons that survive the absorption process inside the nucleus and are detected. The definition is given by:

$$P_{esc} = \frac{\int_{R_{esc}}\left(\frac{d^2\sigma}{d\Omega dE}\right)_{esc}dE}{\int_{R_{total}}\left(\frac{d^2\sigma}{d\Omega dE}\right)_{total}dE} \tag{6.5}$$

Here, distinct integration ranges are applied to the numerator and the denominator

to correctly evaluate the probability. The numerator is integrated over the full range of the measured escape spectrum (R_{esc}), while the denominator employs a sufficiently wide range (R_{total}) to cover the entire theoretical strength of the quasi-free process.

6.2.4 Theoretical Sensitivity to the Optical Potential Depth

Based on the theoretical framework of the Green's function method, the calculated energy spectra and the resulting escape probabilities exhibit significant sensitivity to the optical potential parameters. In particular, the imaginary depth W_0, which governs the absorption of the K^- meson within the nuclear medium, plays a crucial role in determining the spectral shape. For the case of the shallow imaginary potential, since the absorption effect is relatively weak, the conversion process is limited. This allows a large fraction of the produced K^- mesons to survive and be emitted from the nucleus. For the deeper case, as the imaginary potential becomes deeper, the conversion process —primarily via $K^-N \to \Sigma\pi$ and $\Lambda\pi$ reactions—becomes dominant due to the increased absorption strength.

6.3 Analysis Methodology and Fitting Model

To determine the optimal optical potential parameters (V_0, W_0), a simultaneous χ^2 minimization fit was performed on both the inclusive and escape spectra using a grid search method in the (V_0, W_0) parameter space.

6.3.1 Formulation of Fitting Functions

The fitting functions were constructed by combining theoretical templates calculated via the Green's function method with quasi-free (QF) scattering components. Each component was convoluted with a Gaussian function to account for the detector's energy resolution. The model for the inclusive spectrum, $Model_{\mathrm{Inc}}$, is formulated as follows:

$$Model_{\mathrm{Inc}} = A \cdot f \cdot T_{\mathrm{Inc}} + A \cdot (1-f) \cdot Kp^{\mathrm{Inelastic}} + \sum_{i=0}^{5} S_{n_i} \cdot Kn_i^{\mathrm{Inelastic}} \tag{6.6}$$

The parameters and components are defined as:

- A: Global normalization factor.

- f: Fraction of the elastic scattering component, defined as $f = I_0/(I_0+I_1)$, where I_0 and I_1 represent the cross sections for K^-p elastic and inelastic scattering, respectively.
- T_{Inc}: Theoretical inclusive spectrum template generated via interpolation of the grid points.
- $Kp^{\mathrm{Inelastic}}$: Summation of various K^-p inelastic scattering channels.
- $Kn_i^{\mathrm{Inelastic}}$: Inelastic process for each of the six K^-n reaction channels.
- S_{n_i}: Independent scale factors for each K^-n reaction channel.

Crucially, both T_{Inc} and $Kp^{\mathrm{Inelastic}}$ are normalized to unity over the fitting range. This normalization ensures that the parameter f rigorously represents the relative weight of the theoretical template compared to the K^-p reaction components.

6.3.2 Constraints and Justification based on J-PARC E05

In this analysis, the branching ratios among the K^-p inelastic channels, as well as the ratio between the elastic and total inelastic cross sections (f), were fixed based on the $p(K^-, p)$ scattering data from the J-PARC E05 experiment.

This constraint is justified by the difference in experimental conditions; the energy resolution of the current E42 experiment is approximately seven times poorer than that of the E05 experiment. Given this significant resolution difference, it is more reliable to adopt the precise reaction ratios determined by E05 as fixed constraints rather than attempting an independent parameter determination. This approach provides a robust basis for the decomposition of complex reaction processes and enhances the overall reliability of the fit.

6.3.3 Minimization Procedure

The model for the escape spectrum, $Model_{\mathrm{Esc}}$, is defined using the same normalization factor and fraction:

$$Model_{\mathrm{Esc}} = A \cdot f \cdot T_{\mathrm{Esc}} \tag{6.7}$$

A total of seven parameters (A and S_{n_0} to S_{n_5}) were optimized using the `TMinuit` package. The fit was performed simultaneously over the binding energy ranges of -0.04 to 0.30 GeV for the inclusive spectrum and -0.04 to 0.20 GeV for the escape spectrum. The six K^-n reaction channels considered are: $K^- + n \to \Lambda + \pi^-$, $\Sigma^0 + \pi^-$, $K^- + \pi^- + p$, $\Lambda + \pi^0 + \pi^-$, $\Sigma^+ + \pi^- + \pi^-$, and $\Lambda + \pi + \pi + \pi$.

In this simultaneous fitting framework, the resulting optical potential parameters are significantly constrained by both the consistency of the spectral shapes and the relative yield ratio between the inclusive and escape components.

6.4 Fit Results and Parameter Determination

6.4.1 Fit Results and Spectral Reproduction

The binding energy spectra for the $^{12}\mathrm{C}(K^-, p)$ reaction, overlaid with the best-fit curves, are shown in Figure 6.1. The figure displays both the inclusive and escape spectra. In both cases, the experimental data points are reproduced by the optimized model (solid lines) across a wide energy range.

For the inclusive spectrum, the total fit strength is successfully decomposed into the theoretical template, the quasi-free (QF) K^-p inelastic scattering component, and the six K^-n reaction channels. Notably, the spectral tail in the region where the binding energy is positive ($-B_K > 0$ GeV) is accurately described by the contribution of the QF components. This confirms that the background shape is appropriately modeled within this analysis framework.

Furthermore, the escape spectrum is also reproduced by the scaled theoretical template. The consistency between the inclusive and escape fits demonstrates that the proposed model effectively accounts for the underlying physical processes in both channels without contradiction.

6.4.2 2D Likelihood Map and Parameter Determination via HPD Method

To determine the optimal depths of the real (V_0) and imaginary (W_0) parts of the optical potential, a simultaneous fit was performed on both the inclusive and escape spectra.

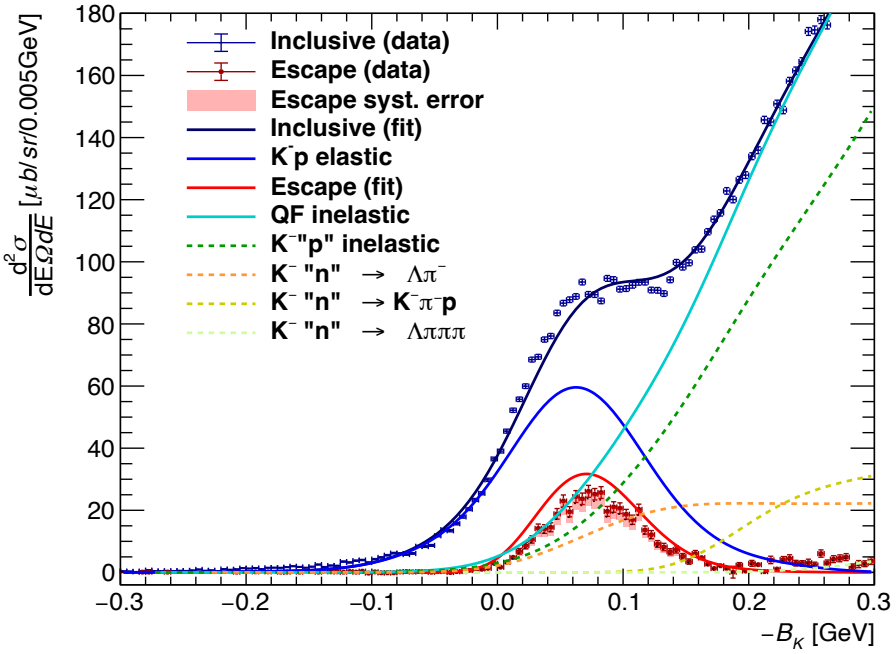

Figure 6.1: Experimental binding energy spectra and the best-fit results for the ^{12}C(K^-, p) reaction. The blue points represent the inclusive data, while the red points represent the escape data with their statistical errors. The filled area indicates the systematic errors for the escape spectrum. The inclusive spectrum is shown with the total fit (black line), which is decomposed into the theoretical template (blue), QF K^-p inelastic (green), and various K^-n reaction channels (other colors). The escape spectrum is fitted with the scaled theoretical template. The fit was performed in the range of -0.04 to 0.30 GeV for the inclusive spectrum and -0.04 to 0.20 GeV for the escape spectrum.

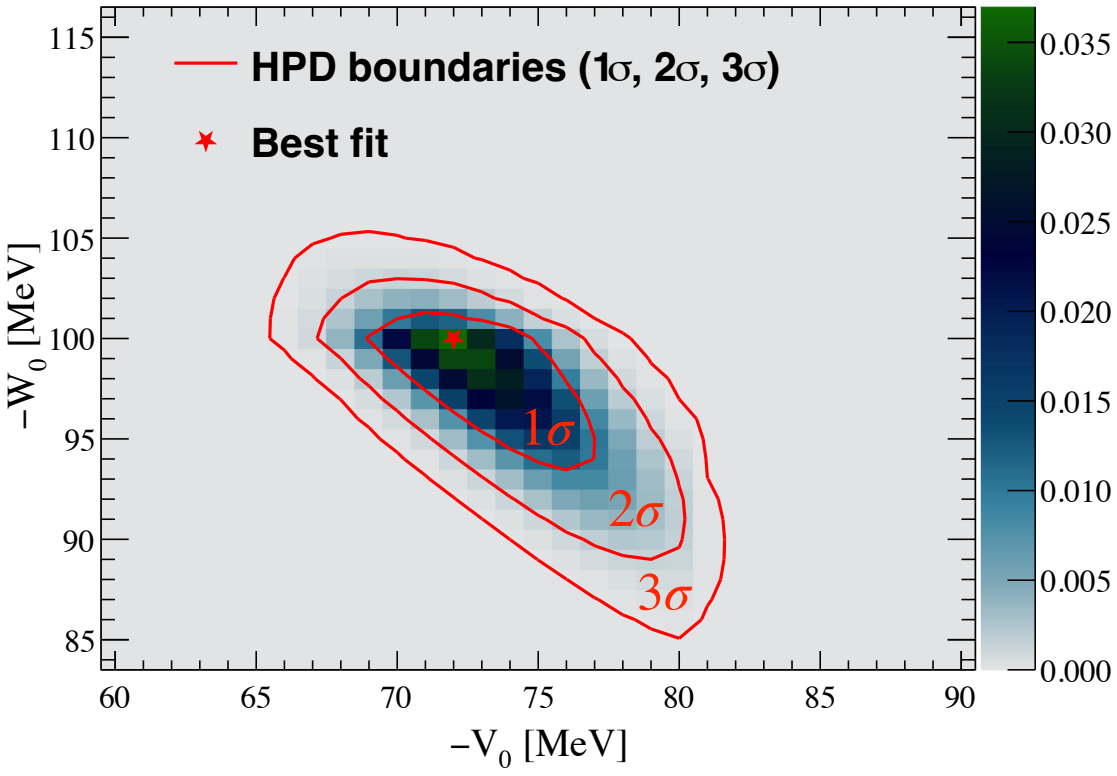

Figure 6.2: Two-dimensional posterior probability distribution as a function of the real (V_0) and imaginary (W_0) optical potential depths. The color scale represents the normalized posterior weights $w_{i,j}$ calculated from the simultaneous fit of the inclusive and escape spectra. The red star indicates the best-fit point where the posterior probability is maximized. The solid red contours represent the boundaries of the 68.27%(1σ), 95.45%(2σ), and 99.73%(3σ) Highest Posterior Density (HPD) regions. The distribution is well-contained within the search region of the grid, with the relative likelihood at the boundaries $R_{\text{boundary}} \leq 0.01$, ensuring a reliable estimation of the statistical uncertainties.

The high sensitivity of this analysis originates from two primary constraints: (1) the theoretical fixed ratio between the inclusive and escape spectra, which is determined by the escape probability within the model, and (2) the strong dependence of the inclusive spectral shape on the imaginary potential depth, where a deeper imaginary part leads to a broadening of the spectral width. These factors provide a robust constraint on the parameter search, allowing for a robust determination of the potential depths.

In this study, the confidence intervals for the parameters are determined using the Highest Posterior Density (HPD) method based on Bayesian statistics. This approach provides a more fundamental and robust estimation of uncertainties compared to a simple χ^2 grid search.

The likelihood ratio (relative likelihood) $R_{i,j}$ at each grid point (i, j) in the (V_0, W_0) parameter space is defined as:

$$R_{i,j} = \exp\left(-\frac{\chi^2_{i,j} - \chi^2_{\min}}{2}\right) \tag{6.8}$$

where $\chi^2_{\min}$ represents the minimum χ^2 value obtained across the grid. Assuming a flat prior distribution $P(V_0, W_0) = \text{const.}$, the posterior probability density is proportional to the likelihood. The normalized posterior weight $w_{i,j}$ for each grid point is then given by:

$$w_{i,j} = \frac{R_{i,j}}{\sum_{k,l} R_{k,l}} \tag{6.9}$$

The HPD region is defined by including grid points in descending order of their posterior weights $w_{i,j}$ until the cumulative probability reaches a specified confidence level P_σ. Figure 6.2 shows the resulting two-dimensional posterior probability distribution. The color scale indicates the normalized posterior weights $w_{i,j}$, and the red contours represent the boundaries of the 1σ, 2σ, and 3σ HPD regions, corresponding to cumulative probabilities of 68.27%, 95.45%, and 99.73%, respectively.

6.4.3 Statistical Significance and Results

As shown in Fig. 6.2, the best-fit point (marked by the red star) is located at the center of the high-probability density region. The minimum χ^2 value obtained at this point is $\chi^2_{\min} = 1566$, which corresponds to $\chi^2/\text{ndf} = 14.5$ with $\text{ndf} = 108$. Although the χ^2/ndf value is relatively large, this is primarily attributed to the inherent limitations of the

theoretical model in perfectly reproducing the entire spectral shape, despite the high statistical precision of the experimental data.

To ensure the validity of this approach given by the finite calculation grid, we confirmed that the maximum likelihood ratio at the boundaries of the search region satisfies $R_{\text{boundary}} \leq 0.001$. This negligible value at the edges indicates that the calculation range is sufficiently wide and that the posterior distribution is well-contained within the search region.

Based on the 1σ HPD region, the optimal potential parameters and their associated statistical uncertainties are determined to be:

$$V_0 = -72^{+3}_{-5}\ \text{MeV}, \quad W_0 = -100^{+7}_{-1}\ \text{MeV} \tag{6.10}$$

These values reflect the high sensitivity of the simultaneous fitting of inclusive and escape spectra to the absorptive strength within the nuclear medium.

6.4.4 Systematic Uncertainties

The systematic uncertainties associated with the determined optical potential parameters, V_0 and W_0, are evaluated by examining the impact of uncertainties in the analysis assumptions on the final fit results. The primary source of systematic error in this study is the uncertainty in the normalization of the escape spectrum.

The evaluation was performed by adopting a 10% fluctuation as the systematic error, as described in Sec. 5.5, to examine its impact on the determined potential parameters.

Evaluation of Parameter Sensitivity

To quantify the systematic errors on V_0 and W_0, the escape spectrum was scaled by its uncertainty ($\pm 10.2\%$), and the simultaneous χ^2 fitting was re-performed for each case. Among the results obtained under these scaling conditions, the parameter set (V_0, W_0) that yielded the minimum χ^2 was adopted as the central value for evaluating the systematic shifts. The optimal parameters were thus fixed at $V_0 = -72$ MeV and $W_0 = -100$ MeV, which also corresponded to the most reliable efficiency estimation.

The systematic uncertainty for each parameter was assigned based on the maximum observed shift in the best-fit central value:

- **Real Part (V_0):** The variation in the escape spectrum normalization resulted in a maximum shift of +8 MeV in the real potential depth, leading to a systematic uncertainty of $^{+8}_{-0}$ MeV.

- **Imaginary Part (W_0):** The imaginary part exhibited a higher sensitivity to the escape yield, with a maximum shift of +16 MeV observed across the various scaling conditions, resulting in a systematic uncertainty of $^{+16}_{-0}$ MeV.

The stability of the analysis framework was further confirmed through several consistency checks:

1. **Stability of Background Modeling**: The sensitivity to the fitting range was tested by comparing the baseline range (-0.040 to 0.300 GeV) with a restricted range (-0.040 to 0.200 GeV). Even with the narrower range, the background (BG) composition remained consistent. Furthermore, the model's extrapolation to the 0.200–0.300 GeV region showed excellent agreement with the data, confirming the validity of the BG assumptions.

2. **Robustness of Reaction Constraints**: The impact of the J-PARC E05 data constraints was evaluated by varying both the branching ratios of the K^-p inelastic channels and the elastic-to-inelastic ratio (f) by $\pm 10\%$. In both cases, the final optical potential parameters remained stable, demonstrating that the results are robust against these input ratios.

Consequently, the total systematic uncertainties are determined to be $^{+8}_{-0}$ MeV for V_0 and $^{+16}_{-0}$ MeV for W_0.

6.4.5 Discussion: Physical Implications

The optical potential parameters obtained from the spectral analysis in this study are as follows:

$$V_0 = -72^{+3}_{-5}\ (\text{stat.})^{+0}_{-8}\ (\text{syst.})\ \text{MeV} \tag{6.11}$$

$$W_0 = -100^{+7}_{-1}\ (\text{stat.})^{+0}_{-16}\ (\text{syst.})\ \text{MeV} \tag{6.12}$$

Particularly the result for the imaginary part $W_0 = -100^{+7}_{-1}\ (\text{stat.})^{+0}_{-16}\ (\text{syst.})$ MeV,

provides significant physical implications regarding the interaction of K^- mesons within the nuclear medium.

Depth of the Imaginary Potential and Absorption Strength

The determined depth of the imaginary potential, $W_0 \approx -100$ MeV, is remarkably deep compared to previous studies, quantitatively demonstrating that K^- mesons undergo extremely strong absorption, also referred to as the conversion process,inside the nucleus. In the context of the optical potential model, the imaginary part is the component of the Hamiltonian that governs particle attenuation and transitions to other reaction channels within the nucleus. This deep W_0 signifies that K^- mesons produced through quasi-free scattering processes have a very high probability of undergoing reactions such as $K^-N \to \Sigma\pi$ and $\Lambda\pi$ with nucleons or via multi-nucleon absorption processes before they can escape the nucleus.

Escape Probability and Discussion of Physical Implications

The experimental escape probability P_{esc}(Data) is determined to be 29 ± 2 (stat.)$^{+0}_{-4}$ (syst.)%. This value is calculated as the ratio of the experimental escape cross-section to the total inclusive cross-section obtained from the fitting results. In contrast, the escape probability calculated from the cross-section ratios of the fitting model, P_{esc}(Fit), is 39%. This value is systematically higher than the experimental value, even when considering the magnitude of experimental uncertainties, as shown in Fig. 6.1.

This systematic discrepancy may indicate the limitations of the current theoretical model. The fact that the experimental escape probability is lower than the model prediction suggests that the effects of multi-nucleon absorption within the nuclear medium may be more significant than what is accounted for in the present framework.

Based on these results, the physical behavior of K^- mesons in the nuclear medium can be concluded as follows. Near the center of the nucleus, the K^- feels a strong attractive real potential ($V_0 = -72$ MeV) while simultaneously undergoing extremely strong absorption due to a deep imaginary potential ($W_0 = -100$ MeV). This picture of a “deep optical potential with strong absorption” has been quantitatively revealed with high precision for the first time through the novel approach of this study: the simultaneous analysis of the inclusive and escape spectra.

Comparison with the Traditional Potential Framework

The optical potential parameters determined in this study, $V_0 = -72^{+3}_{-5}$ (stat.)$^{+0}_{-8}$ (syst.) MeV and $W_0 = -100^{+7}_{-1}$ (stat.)$^{+0}_{-16}$ (syst.) MeV, present a unique case that does not strictly conform to the traditional classification of the "shallow" versus "deep" potentials as discussed in Chapter 2.

As summarized in Table 2.3, theoretical models based on chiral SU(3) dynamics typically predict a shallow potential with $V_0 \sim -40$ to -80 MeV and $W_0 \sim -40$ to -60 MeV. Our result for the real part, $V_0 = -72$ MeV, is in good agreement with these theoretical predictions, supporting the view of a moderately attractive $\bar{K}$-nucleus interaction in the nuclear medium.

However, the imaginary part, $W_0 = -100$ MeV, is significantly deeper than the values predicted by the standard $t\rho$ approximation or chiral microscopic models. Instead, it reaches the magnitude required by phenomenological density-dependent (DD) fits to kaonic atom data, which favor an absorptive strength of approximately -100 MeV. Furthermore, the fact that the real part remains within the shallow regime even in the nuclear interior suggests that it possesses a weaker density dependence than ever expected, in contrast to the imaginary part which appears to be strongly enhanced by non-linear effects such as multi-nucleon absorption.

This nature—characterized by a shallow real depth and a deep imaginary depth—indicates that the K^--nucleus interaction cannot be fully described solely by one-nucleon scattering processes. As motivated in Sec. 2.1, such a large absorptive strength strongly suggests the dominance of multi-nucleon absorption processes, such as $K^-NN \to YN$, within the dense nuclear interior. Furthermore, the discrepancy between our results and the simple $t\rho$ predictions points toward a density dependence of the absorption mechanism, which becomes manifest as the antikaon penetrates the nuclear interior. The simultaneous constraint on both potential depths achieved in this work provides a new experimental foundation for understanding these complex many-body medium effects.

Chapter 7

Conclusion and Prospects

7.1 Conclusion

In this dissertation, we have investigated the $\overline{K}$-nucleus interaction, specifically focusing on the imaginary part of the optical potential, through the exclusive measurement of the $^{12}C(K^-, p)$ reaction. The experiment, J-PARC E42, was performed at the K1.8 beamline of the J-PARC Hadron Experimental Facility using a high-intensity K^- beam of 1.8 GeV/c.

The primary motivation of this study was to resolve the long-standing ambiguity regarding the strength of the anti-kaon absorption in the nuclear medium. While previous kaonic atom data and inclusive measurements (J-PARC E05) constrained the real part of the potential to be relatively shallow ($V_0 \sim -80$ MeV), the imaginary part (W_0) remained poorly determined. Theoretical models range from shallow to deep absorption, and precise determination of W_0 is crucial for understanding the properties of kaonic nuclei and the equation of state for dense nuclear matter.

To address this issue, we measured the escape process of the scattered K^- meson. This quantity represents the process where a K^- produced via the quasi-free elastic scattering (QFES) process survives its passage through the nucleus without being absorbed. Since absorption is directly governed by the imaginary potential, the escape probability serves as a sensitive probe for W_0.

We successfully measured the $^{12}C(K^-, p)$ reaction using the KURAMA spectrometer for the scattered proton and the newly installed Hyperon Time Projection Chamber (HypTPC) for detecting the escaping K^-. The large acceptance of the HypTPC allowed

for the efficient detection of recoil K^- mesons and other decay products.

The analysis proceeded in two main steps. First, the inclusive $^{12}C(K^-, p)$ spectrum was obtained, which showed good agreement with previous high-precision data from J-PARC E05, validating our experimental setup. Second, the exclusive "escape K^- spectrum" was derived by tagging events with a surviving K^- detected in the HypTPC. A rigorous analysis was performed to subtract physical backgrounds, primarily from inelastic processes ($K^-p \to K^-\pi^0 p$), using kinematic correlations and template fitting methods. Efficiency corrections were carefully applied, validated by comparing results from Carbon and Polyethylene targets.

We successfully derived the escape cross-section to be $\left(\frac{d\sigma}{d\Omega}\right)_{\rm esc} = 436 \pm 6$ (stat.) $\pm$ 26 (syst.) μb/sr. The escape probability was derived by taking the ratio of the integrated escape cross-section to the total QFES cross-section.

To further investigate the $\bar{K}$-nucleus interaction, we performed a simultaneous χ^2 minimization fit to both the inclusive and escape spectra. This analysis yielded the optimal potential depths at the nuclear center as: $V_0 = -72^{+3}_{-5}$ (stat.)$^{+0}_{-8}$ (syst.) MeV and $W_0 = -100^{+7}_{-1}$ (stat.)$^{+0}_{-16}$ (syst.) MeV. This determination represents a significant advancement over previous studies using kaonic atoms. While global fits to atomic data are often limited by a "continuous ambiguity" where the real and imaginary parts cannot be uniquely disentangled, our study achieved a high-precision and independent determination of both potential depths. By utilizing an in-flight reaction that penetrates deep into the nuclear interior, this work has successfully extracted essential information regarding the strong interaction in the dense nuclear environment, which was previously inaccessible.

The obtained parameters reveal a unique nature of the potential: a moderately attractive real part consistent with chiral unitary models, combined with a deeply absorptive imaginary part matching the magnitude of phenomenological fits. This result suggests the dominance of multi-nucleon absorption processes, such as $\bar{K}NN \to YN$, and highlights their significant role in the in-medium nature of antikaons.

In conclusion, this research has established a definitive experimental foundation for the $\bar{K}$-nucleus optical potential. By overcoming the limitations of surface-sensitive atomic probes and uniquely constraining the interaction deep inside the nucleus, we have provided a unified and quantitative description of antikaon propagation in dense

hadronic matter.

7.2 Prospects

The results presented in this thesis mark a significant step forward in understanding the $\overline{K}$-nucleus interaction. However, the rich data set collected in the J-PARC E42 experiment offers further opportunities for investigation.

Detailed Study of Absorption Mechanisms The large imaginary potential derived in this work implies the dominance of multi-nucleon absorption. A direct measurement of the charge exchange channel ($K^- p \to \bar{K}^0 n$) or the non-mesonic decay channels (e.g., $K^- NN \to \Lambda N, \Sigma N$) using the HypTPC would provide microscopic verification of this phenomenological finding. The capability of the HypTPC to track multiple charged particles is ideally suited for such multi-particle correlation studies.

Investigation of the Deeply Bound Region One of the remaining puzzles from the J-PARC E05 experiment was the observation of an event excess in the deeply bound region ($B_K \sim 100$ MeV) that could not be explained by simple quasi-free processes. While the present study focused on the quasi-free elastic region to determine the optical potential, the HypTPC data allows for an exclusive analysis of this deeply bound region. By reconstructing specific final states, such as Λp or $\Sigma\pi$ pairs, we can decompose the inclusive spectrum and identify the origin of this excess. This analysis will clarify whether the structure corresponds to a bound state of Y^* and nucleus or arises from any other exotic processes.

In conclusion, this study has successfully constrained the imaginary part of the $\overline{K}$-nucleus optical potential through the novel measurement of the K^- escape probability. The established potential parameters and the experimental methods developed herein provide a solid foundation for future studies of strange nuclear physics.

Appendix A

TPC acceptance

Using the optimized PID conditions determined in the previous section, the overall detection efficiency for scattered K^- is evaluated. This efficiency, referred to as TPC acceptance, includes geometrical acceptance, track reconstruction efficiency, and PID efficiency.

To derive the differential cross-section of the escape K^- spectrum, the measured yield must be corrected for the detection efficiency of scattered K^- in the HypTPC (the product of geometrical acceptance, track reconstruction efficiency, and PID efficiency). This overall detection efficiency, hereinafter referred to as TPC acceptance, was evaluated.

Due to the kinematics of the quasi-free scattering process, the emission angle of the scattered K^- is strongly correlated with the angle of the scattered proton detected by the spectrometer. Therefore, it is important to check whether the TPC acceptance depends on the kinematic variables of the scattered proton, particularly the azimuthal angle (ϕ). Figure 1 shows the TPC detection efficiency of scattered K^- as a function of the laboratory azimuthal angle ϕ_p of the scattered proton. As can be seen in the figure, while the efficiency is generally constant with respect to ϕ_p, slight variations exist, likely attributable to the sector structure of the TPC and its alignment with respect to the beam.

To estimate the impact of this ϕ dependence on the final cross-section evaluation, a comparative study using different correction methods was performed. Figure 2 compares the escape spectrum corrected event-by-event using the efficiency corresponding to its ϕ_p (red histogram) with the spectrum corrected using a constant efficiency averaged over the entire ϕ region (blue histogram). As indicated by the ratio shown in the

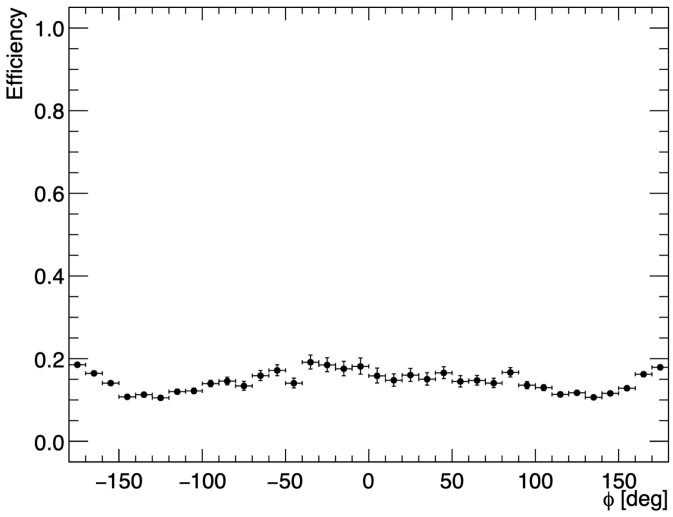

Figure 1: TPC detection efficiency of scattered K^- as a function of the laboratory azimuthal angle (ϕ_p) of the scattered proton, evaluated via simulation.

bottom panel of the figure, the difference between the two is relatively less than 2% across the entire spectral range. This confirms that the impact of the ϕ dependence of the TPC acceptance on the escape K^- cross-section is very small and negligible.

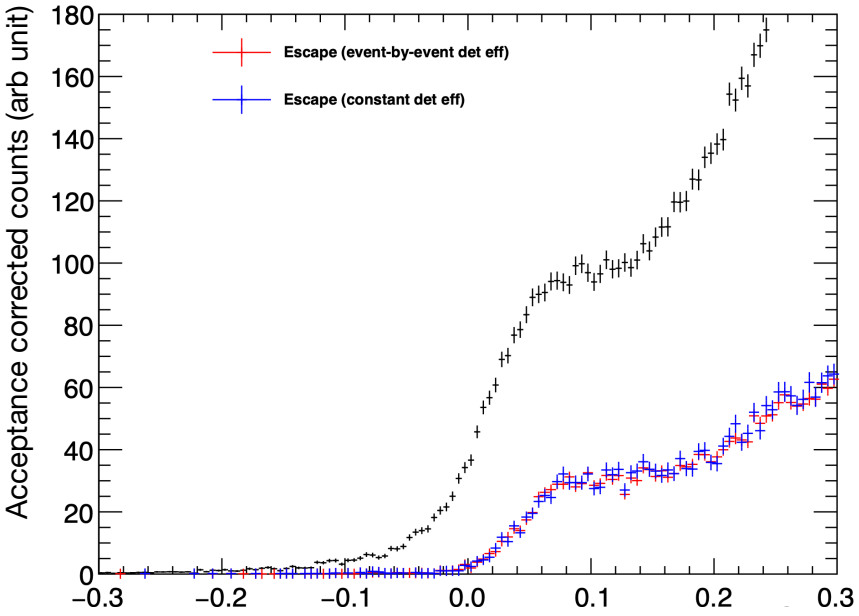

Figure 2: Comparison of escape K^- differential cross-section spectra corrected considering the ϕ dependence of TPC acceptance (red histogram) and using a constant efficiency (blue histogram). The bottom panel shows the ratio between them. The difference is relatively less than 2%.

References

[1] A. D. Martin. "Kaon-nucleon parameters". In: *Nuclear Physics B* 179 (1981), pp. 33–48. DOI: 10.1016/0550-3213(81)90247-9.

[2] M. Alston-Garnjost et al. "Differential cross section of the reaction $K^- p \to \bar{K}^0 n$ from 515 to 956 MeV/c". In: *Phys. Rev. D* 17 (1978), p. 2226. DOI: 10.1103/PhysRevD.17.2226.

[3] N. H. Bedford. "K-p Interactions below 250 MeV/c". Cited as preliminary TST data in Martin (1981). PhD thesis. Durham University, 1979.

[4] Nowak et al. "Charged Σ hyperon production by K^- meson interactions at rest". In: *Nucl. Phys. B* 139 (1978), pp. 61–71. DOI: 10.1016/0550-3213(78)90179-6.

[5] S. Deser et al. "Energy Level Displacements in π-Mesonic Atoms". In: *Physical Review* 96 (1954), pp. 774–776. DOI: 10.1103/PhysRev.96.774.

[6] T.L. Trueman. "Energy level shifts in atomic states of strongly-interacting particles". In: *Nuclear Physics* 26 (1961), pp. 57–67. DOI: 10.1016/0029-5582(61)90115-8.

[7] M. Iwasaki et al. "Observation of K-series X rays of kaonic hydrogen". In: *Physical Review Letters* 78 (1997), pp. 3067–3069. DOI: 10.1103/PhysRevLett.78.3067.

[8] G. Beer et al. "Measurement of the Kaonic Hydrogen X-Ray Spectrum". In: *Physical Review Letters* 94 (2005), p. 212302. DOI: 10.1103/PhysRevLett.94.212302.

[9] M. Bazzi et al. "A new measurement of kaonic hydrogen X-rays". In: *Physics Letters B* 704 (2011), pp. 113–117. DOI: 10.1016/j.physletb.2011.09.011.

[10] Y. Ikeda, T. Hyodo, and W. Weise. "Improved constraints on chiral SU(3) dynamics from kaonic hydrogen". In: *Physics Letters B* 706 (2011), pp. 63–67. DOI: 10.1016/j.physletb.2011.10.053.

[11] Y. Ikeda, T. Hyodo, and W. Weise. "Chiral SU(3) theory of antikaon - nucleon interactions with improved threshold constraints". In: *Nuclear Physics A* 881 (2012), pp. 98–114. DOI: 10.1016/j.nuclphysa.2012.01.012.

[12] M. Mai and U.-G. Meissner. "New insights into antikaon - nucleon scattering and the structure of the Λ (1405)". In: *Nuclear Physics A* 900 (2013), pp. 51–64. DOI: 10.1016/j.nuclphysa.2013.01.032.

[13] A. Cieplý and J. Smejkal. "Chiral SU(3) dynamics constrained by the SIDDHARTA kaonic hydrogen data: $\bar{K}N$ scattering lengths and kaonic hydrogen". In: *Nuclear Physics A* 881 (2012), pp. 115–122. DOI: 10.1016/j.nuclphysa.2012.01.013.

[14] Z.-H. Guo and J. A. Oller. "Meson - baryon reactions with strangeness -1 within a chiral framework". In: *Physical Review C* 87 (2013), p. 035202. DOI: 10.1103/PhysRevC.87.035202.

[15] T. Hyodo. "Antikaon - nucleon dynamics and its application to few-body systems". In: *Nuclear Physics A* 914 (2013), pp. 260–274. DOI: 10.1016/j.nuclphysa.2013.01.015.

[16] Shreyasi Acharya et al. "Scattering Studies with Low-Energy Kaon-Proton Femtoscopy in Proton-Proton Collisions at the LHC". In: *Phys. Rev. Lett.* 124.9 (2020), p. 092301. DOI: 10.1103/PhysRevLett.124.092301. arXiv: 1905.13470 [nucl-ex].

[17] S. Navas and others (Particle Data Group). "Review of Particle Physics". In: *Phys. Rev. D* 110 (3 2024). (Particle Data Group), p. 030001. DOI: 10.1103/PhysRevD.110.030001. URL: https://pdg.lbl.gov/.

[18] D. Jido et al. "Chiral dynamics of the two $\Lambda(1405)$ states". In: *Nucl. Phys. A* 725 (2003), pp. 181–200. DOI: 10.1016/S0375-9474(03)01598-7.

[19] H. Kamano et al. "$\Lambda(1405)$ pole in a dynamical coupled-channels model". In: *Phys. Rev. C* 92.2 (2015), p. 025205. DOI: 10.1103/PhysRevC.92.025205. arXiv: 1506.01725 [nucl-th].

[20] Y. Ikeda, T. Hyodo, and W. Weise. "Coupled-channels approach to $\bar{K}N$ scattering and $\Lambda(1405)$ in chiral SU(3) dynamics". In: *Nucl. Phys. A* 881 (2012), pp. 98–114. DOI: 10.1016/j.nuclphysa.2012.01.012.

[21] S. Aikawa et al. "Pole position of $\Lambda(1405)$ measured in $d(K^-, n)\pi\Sigma$ reactions". In: *Phys. Lett. B* 837 (2023), p. 137637. DOI: 10.1016/j.physletb.2022.137637.

[22] M. Niiyama et al. "Photoproduction of $\Lambda(1405)$ and $\Sigma^0(1385)$ on the proton at $E_\gamma = 1.5 - 2.4$ GeV". In: *Phys. Rev. C* 78 (2008), p. 035202. DOI: 10.1103/PhysRevC.78.035202. arXiv: 0805.4051 [hep-ex].

[23] K. Moriya et al. "Measurement of the $\Sigma\pi$ photoproduction line shapes near the $\Lambda(1405)$". In: *Phys. Rev. C* 87 (2013), p. 035206. DOI: 10.1103/PhysRevC.87.035206.

[24] H. Y. Lu et al. "First Observation of the $\Lambda(1405)$ Line Shape in Electroproduction". In: *Phys. Rev. C* 88 (2013), p. 045202. DOI: 10.1103/PhysRevC.88.045202.

[25] M. Agnello et al. "Evidence for a $\bar{K}$-Nuclear Bound State". In: *Phys. Rev. Lett.* 94 (2005), p. 212303. DOI: 10.1103/PhysRevLett.94.212303.

[26] T. Yamazaki et al. "Indication of a Deeply Bound Compact K^-pp State Formed in the $pp \to p\Lambda K^+$ Reaction at 2.85 GeV". In: *Phys. Rev. Lett.* 104 (2010), p. 132502. DOI: 10.1103/PhysRevLett.104.132502.

[27] G. Agakishiev et al. "Proton-proton collisions at 3.5 GeV: A comprehensive analysis". In: *Eur. Phys. J. A* 50 (2014), p. 82. DOI: 10.1140/epja/i2014-14082-1. arXiv: 1403.4288 [nucl-ex].

[28] J. Adamczewski-Musch et al. "Search for the K^-pp bound state in $p+p$ collisions at 3.5 GeV". In: *Phys. Rev. C* 103 (2021), p. 025204. DOI: 10.1103/PhysRevC.103.025204.

[29] G. Bendiscioli et al. "Review of Low-Energy $\bar{K}$ Nucleon and $\bar{K}$ Nuclear Physics by the OBELIX Collaboration". In: *Nuclear Physics A* 789 (2007), pp. 222–242. DOI: 10.1016/j.nuclphysa.2007.03.012.

[30] G. Bendiscioli et al. "Low-energy $\bar{K}$-nuclei interaction studies by the OBELIX Collaboration". In: *European Physical Journal A* 40 (2009), pp. 11–20. DOI: 10.1140/epja/i2009-10787-6.

[31] A. Tokiyasu et al. "Search for the K^-pp bound state via the $\gamma d \to K^+\pi^- X$ reaction". In: *Phys. Lett. B* 728 (2014), pp. 616–620. DOI: 10.1016/j.physletb.2013.12.039.

[32] Y. Ichikawa et al. "Observation of the 201cK^-pp"-like structure in the $d(\pi^+, K^+)$ reaction at 1.69 GeV/c". In: *Prog. Theor. Exp. Phys.* 2015 (2015), p. 021D01. DOI: 10.1093/ptep/ptv002.

[33] S. Ajimura et al. "The K^-pp bound state observed in the ^{3}He$(K^-, \Lambda p)n$ reaction". In: *Phys. Lett. B* 743 (2015), pp. 305–309. DOI: 10.1016/j.physletb.2015.02.033. arXiv: 1408.5768 [nucl-ex].

[34] T. Hashimoto et al. "Search for the 201cK^-pp"-like structure in the ^{3}He(K^-, n) reaction at 1.0 GeV/c". In: *Prog. Theor. Exp. Phys.* 2015.6 (2015), p. 061D01. DOI: 10.1093/ptep/ptv076.

[35] T. Yamaga et al. "Observation of a $\bar{K}NN$ bound state in the ^{3}He(K^-, n) reaction". In: *Phys. Rev. C* 102.4 (2020), p. 044002. DOI: 10.1103/PhysRevC.102.044002.

[36] S. Acharya et al. "Study of the p - p - K^+ and p - p - K^- dynamics using the femtoscopy technique". In: *Eur. Phys. J. A* 59.12 (2023), p. 298. DOI: 10.1140/epja/s10050-023-01139-9. arXiv: 2303.13448 [nucl-ex].

[37] Y. Akaishi and T. Yamazaki. "Nuclear $\bar{K}$ bound states in light nuclei". In: *Physical Review C* 65.4 (2002), p. 044005. DOI: 10.1103/PhysRevC.65.044005.

[38] N. Barnea, A. Gal, and E. Z. Liverts. "Realistic calculations of single- and double-$\bar{K}$ nuclear bound states". In: *Physics Letters B* 712 (2012), pp. 132–136. DOI: 10.1016/j.physletb.2012.04.021.

[39] A. Dote, T. Hyodo, and W. Weise. "Variational calculation of the K^-pp system based on chiral SU(3) dynamics". In: *Physical Review C* 79 (2009). ppK^- system with energy-dependent effective $\bar{K}N$ interaction, p. 014003. DOI: 10.1103/PhysRevC.79.014003.

[40] A. Doté, T. Hyodo, and W. Weise. "Variational calculation of the K^-pp system based on chiral SU(3) dynamics". In: *Physical Review C* 79 (2009), p. 014003. DOI: 10.1103/PhysRevC.79.014003.

[41] Y. Ikeda, H. Kamano, and T. Sato. "Target and energy dependence of K^-pp quasi-bound state in a coupled-channel Faddeev calculation". In: *Progress of Theoretical Physics* 124 (2010), pp. 533–557. DOI: 10.1143/PTP.124.533.

[42] N. V. Shevchenko, A. Gal, and J. Mareš. "Faddeev calculation of a $\bar{K}NN$ quasi-bound state". In: *Physical Review Letters* 98 (2007), p. 082301. DOI: 10.1103/PhysRevLett.98.082301.

[43] N. V. Shevchenko et al. "Faddeev calculation of the $\bar{K}NN$ system with coupled channels". In: *Physical Review C* 76 (2007), p. 044004. DOI: 10.1103/PhysRevC.76.044004.

[44] Y. Ikeda and T. Sato. "Energy-dependent $\bar{K}N$ interaction and the three-body $\bar{K}NN$ bound state". In: *Physical Review C* 79 (2009), p. 035201. DOI: 10.1103/PhysRevC.79.035201.

[45] S. Wycech and A. M. Green. "Variational calculations for $\bar{K}NN$ bound states". In: *Physical Review C* 79 (2009), p. 014001. DOI: 10.1103/PhysRevC.79.014001.

[46] T. Hyodo and W. Weise. "Effective $\bar{K}N$ interaction based on chiral SU(3) dynamics". In: *Physical Review C* 77 (2008), p. 035204. DOI: 10.1103/PhysRevC.77.035204.

[47] Shuji Maeda, Yoshinori Akaishi, and Toshimitsu Yamazaki. "Strong binding and shrinkage of single and double $\bar{K}$ nuclear systems (K^-pp, K^-ppn, K^-K^-p and K^-K^-pp) predicted by Faddeev-Yakubovsky calculations". In: *Proceedings of the Japan Academy, Series B* 89.9 (2013), pp. 418–437. DOI: 10.2183/pjab.89.418.

[48] A. Dote, T. Hyodo, and W. Weise. "K^-pp system with chiral SU(3) effective interaction". In: *Nuclear Physics A* 804 (2008), pp. 197–206. DOI: 10.1016/j.nuclphysa.2008.02.001.

[49] Yudai Ichikawa. "Strange dibaryon system produced in the $d(\pi^+, K^+)$ reaction at J-PARC". Doctoral dissertation. PhD thesis. Kyoto University, Feb. 2015.

[50] C. Curceanu et al. "Kaonic Deuterium Measurement with SIDDHARTA-2 on DAΦNE". In: *Acta Physica Polonica B* 51.1 (2020), pp. 251–257. DOI: 10.5506/APhysPolB.51.251. URL: https://repozitorij.pmf.unizg.hr/object/pmf:8619.

[51] J. Zmeskal et al. "Measurement of the Strong Interaction Induced Shift and Width of the Kaonic Deuterium Atom 1s State". In: *Acta Physica Polonica B* 46.1 (2015), pp. 101–112. DOI: 10.5506/APhysPolB.46.101.

[52] M. Sato et al. "X-ray spectroscopy of kaonic ^{3}He 3d→2p transition". In: *Phys. Lett. B* 654 (2007), pp. 80–84. DOI: 10.1016/j.physletb.2007.08.038.

[53] C. J. Batty, E. Friedman, and A. Gal. "Strong interaction effects in kaonic atoms". In: *Phys. Rep.* 287 (1997), pp. 385–445. DOI: 10.1016/S0370-1573(97)00011-2.

[54] T. Waas and W. Weise. "S-wave interactions of K̄ and η mesons in nuclear matter". In: *Nuclear Physics A* 625.1 (1997), pp. 287–306. ISSN: 0375-9474. DOI: https://doi.org/10.1016/S0375-9474(97)00487-9. URL: https://www.sciencedirect.com/science/article/pii/S0375947497004879.

[55] A. Cieplý et al. "Study of chirally motivated low-energy K^- optical potentials". In: *Nucl. Phys. A* 696.1-2 (2001), pp. 173–193. DOI: 10.1016/S0375-9474(01)01140-5.

[56] A. Ramos and E. Oset. "The properties of the $\bar{K}$ in the nuclear medium". In: *Nucl. Phys. A* 671 (2000), pp. 481–513. DOI: 10.1016/S0375-9474(99)00627-9.

[57] J. Mareš, E. Friedman, and A. Gal. "$\bar{K}$-nuclear bound states in a dynamical model". In: *Nucl. Phys. A* 770.1-2 (2006), pp. 84–105. DOI: https://doi.org/10.1016/j.nuclphysa.2006.02.010.

[58] N. Barnea and E. Friedman. "Radial sensitivity of kaonic atoms and strongly bound $\bar{K}$ states". In: *Phys. Rev. C* 75 (2007), 022202(R). DOI: 10.1103/PhysRevC.75.022202.

[59] E. Friedman and A. Gal. "In-medium nuclear interactions of low-energy hadrons". In: *Physics Reports* 452 (2007), pp. 89–153.

[60] T. Hashimoto et al. "Measurements of Strong-Interaction Effects in Kaonic-Helium Isotopes at Sub-eV Precision with X-Ray Microcalorimeters". In: *Phys. Rev. Lett.* 128 (11 2022), p. 112503. DOI: 10.1103/PhysRevLett.128.112503.

[61] J Yamagata-Sekihara et al. "Investigation of Kaonic Atom Optical Potential by the High-Precision Data of Kaonic 3He and 4He Atoms". In: *Progress of Theoretical and Experimental Physics* 2025.1 (Jan. 2025), p. 013D02. ISSN: 2050-3911. DOI: 10.1093/ptep/ptae189. eprint: https://academic.oup.com/ptep/article-pdf/2025/1/013D02/61218706/ptae189.pdf. URL: https://doi.org/10.1093/ptep/ptae189.

[62] Yutaro Iizawa et al. "Origin of energy shift in kaonic atom and kaon-nucleus interaction". In: (2019). arXiv: 1907.05626 [nucl-th]. URL: https://arxiv.org/abs/1907.05626.

[63] P. A. Katz et al. "Reactions of Stopped K^- in Helium". In: *Phys. Rev. D* 1 (5 1970), pp. 1267–1276. DOI: 10.1103/PhysRevD.1.1267.

[64] C. Vander Velde-Wilquet et al. "Determination of the branching fractions for K^--meson absorption at rest in carbon nuclei". In: *Nuovo Cimento A* 39.4 (1977), pp. 538–547. DOI: 10.1007/BF02771028.

[65] T. Kishimoto et al. "Search for deeply bound kaonic nuclear states by in-flight K^- reactions". In: *Prog. Theor. Phys.* 118 (2007), pp. 181–202. DOI: 10.1143/PTP.118.181.

[66] Y. Ichikawa et al. "An event excess observed in the deeply bound region of the ^{12}C(K^-, p) missing-mass spectrum". In: *Progress of Theoretical and Experimental Physics* 2020.12 (Dec. 2020), p. 123D01. ISSN: 2050-3911. DOI: 10.1093/ptep/ptaa139. eprint: https://academic.oup.com/ptep/article-pdf/2020/12/123D01/36875482/ptaa139.pdf. URL: https://doi.org/10.1093/ptep/ptaa139.

[67] T. Waas, N. Kaiser, and W. Weise. "In-medium effects on K^- mesons in dense nuclear matter". In: *Nuclear Physics A* 617 (1997), pp. 449–460.

[68] A. Ramos and E. Oset. "The properties of antikaons in the nuclear medium". In: *Nuclear Physics A* 671 (2000), pp. 481–502. DOI: 10.1016/S0375-9474(99)00846-X.

[69] E. Oset and A. Ramos. "Non-perturbative chiral approach to s-wave $\bar{K}N$ interactions". In: *Nuclear Physics A* 635 (1998), pp. 99–120. DOI: 10.1016/S0375-9474(98)00170-5.

[70] A. Cieplý and J. Smejkal. "Self-consistent calculations of antikaon-nuclear quasi-bound states". In: *Nucl. Phys. A* 881 (2012), pp. 115–126. DOI: 10.1016/j.nuclphysa.2012.02.015.

[71] S. H. Kim et al. "Cosmic-ray test of a time-of-flight detector for double-strangeness experiments at J-PARC". In: *Nucl. Instrum. Methods Phys. Res. A* 795 (2015), pp. 39–44. DOI: 10.1016/j.nima.2015.05.046.

[72] Wooseung Jung. “Study of Double-Strangeness Production in the $^{12}C(K^-, K^+)$ Reaction at 1.8 GeV/c”. Doctoral dissertation. PhD thesis. Korea University, 2025.

[73] T. Matsuo et al. “Computer Program ”TRIO” for Third Order Calculation of Ion Trajectory”. In: *J. Mass Spectrom. Soc. Jpn.* 24.1 (1976). Also cited as Mass Spectroscopy (Japan), pp. 19–61.

[74] J. Yamagata-Sekihara et al. “Formation of Kaonic Atoms and Kaonic Nuclei in In-Flight (K^-, p) Reactions”. In: *Prog. Theor. Phys.* 114 (2005). [Erratum: Prog. Theor. Phys. 114, 905 (2005)], pp. 301–316. DOI: 10.1143/PTP.114.301.